Techniques and Applications of Compton Imaging for Position-Sensitive Gamma-Ray Detectors

by

Weiyi Wang

A dissertation submitted in partial fulfillment
of the requirements for the degree of
Doctor of Philosophy
(Nuclear Engineering and Radiological Sciences)
in The University of Michigan
2011

Doctoral Committee:

Professor Zhong He, Chair
Professor Jeffrey A. Fessler
Emeritus Professor Glenn F. Knoll
Assistant Professor Clayton D. Scott

To my family

TABLE OF CONTENTS

LIST OF FIGURES

ix

xi

LIST OF TABLES

ABSTRACT

Techniques and Applications of Compton Imaging for Position-Sensitive
Gamma-Ray Detectors

by

Weiyi Wang

Chair: Zhong He

Three-dimensional position-sensitive CdZnTe gamma ray detectors are capable of achieving excellent energy resolution at room temperature. With this versatile detector technology, many types of imaging techniques and applications become possible. The maximum-likelihood expectation-maximization (MLEM) method estimates the source distribution for which the set of measured events is most probable. This method is capable of estimating the source image from each energy range as well as the incident spectrum from each direction. The resulting deconvolved incident spectrum, which has the correct branching ratio in the source direction, is useful for identifying the source isotope and estimating the source activity from each direction, as well as estimating the presence, composition and thickness of any shielding material.

To use a greater fraction of events, the system-response function is analytically extended to three-interaction events, and then it is extrapolated to events with any number of interactions from an array system. Also, by combining charge-sharing

events, and including events with any number of interactions in the system model, imaging makes use of all recorded events, and the angular resolution is improved.

Some interesting applications for which our detector and imaging algorithms are shown to be capable include: reconstructing the distribution of the natural radiation background, finding anomalies in a smoothly varying background, and compensating for the known motion of a source. Two methods are proposed for motion compensation. The first method rotates the imaging reference frame to track the movement of the source. Alternatively, the second method extends the imaging space with additional time dependent target bins. Both methods can be applied to simple backprojection as well as the MLEM deconvolution. Also, when imaging directions are desired to be associated with physical objects, an overlaid optical-radiation image can be generated.

With the sub-pixel interaction position sensing capability of the new digital ASIC, the image blur associated with the difference between the true Compton scattering location and the measured centroid of the recoil electron cloud can be reduced by altering the back-projection cone angle. Appreciable improvement of the image angular resolution is achieved using this method with both simulated and experimental data.

CHAPTER I

Introduction

1.1 Gamma-Ray Imaging Techniques

Gamma rays are electromagnetic radiation of high frequency. They are difficult to detect because of their high penetrating power. However, for the same reason, detecting gamma rays is very attractive to homeland security applications because these high energy photons require heavy material to be shielded. Reconstructing the distribution of gamma ray emitters has been studied for decades in many fields such as astrophysics, nuclear medicine, and industrial scanning.

Gamma rays mainly interact with the detector materials by three different mechanisms: photoelectric absorption, pair production, and Compton scattering. In the photoelectric effect, electrons are emitted from the detector material as a consequence of full-energy absorption from the incident gamma ray. By measuring the electrons created from this interaction, one can estimate the energy of the gamma ray. In CdZnTe detectors, the photoelectric effect is most prominent when the incident photon carries an energy less than 200 keV. Based solely on this photoelectric effect, various imaging techniques have been developed, including X-ray imaging [1], Computed Tomography (CT) [2], Single Photon Emission Computed Tomography (SPECT) [3; 4], Positron Emission Tomography (PET) [5; 6], coded aperture [7; 8; 9], centroid method [10], and attenuation imaging which will be briefly discussed in sec-

tion 5.3.

Pair production can only occur when the incident photon has an energy exceeding twice of the rest energy of an electron (1.022 MeV). An electron-positron pair is created in this process, and when the short-lived positron annihilates with an electron, two annihilation photons each with an energy of 511 keV are created. Since the directions of the annihilation photons are independent of the incident gamma ray, this effect cannot be used in estimating the direction of the gamma-ray emitter unless the track of the initial positron and electron can be measured.

When a gamma ray Compton scatters with the detector material, part of the energy of the gamma ray is transferred to the scattering electron which recoils and is ejected from its atom. This recoil electron travels a short distance in the detector before losing all of its energy and creating a cloud of electron-hole pairs along its path. In CdZnTe detectors, Compton scattering effect is the dominant interaction type from 300 keV to several MeV [11], which defines the energy range of a Compton camera. The basic concept of obtaining the direction of the incident gamma ray using Compton scattering is proposed by Schönfelder et al [12]. A variety of materials and designs have been used in the development of Compton cameras [13; 14; 15]. Du, from the University of Michigan, built a Compton camera using CdZnTe for the first time [16]. Prior to the introduction of three-dimensional position sensitivity, all Compton camera designs involved two layers: a scatter layer and an absorption layer. Lehner et al demonstrated Compton imaging and achieved 4π field of view (FOV) using a single three-dimensional position-sensitive CdZnTe detector [17]. Efforts have been made to combine a Compton camera with an active coded aperture to form a hybrid imager with an extended energy range below 300 keV [18; 19]. If the track of the recoil electron is measured, the angular resolution can be significantly improved [20; 21]. The details of how to utilize Compton scattering to create an image of the source distribution is discussed throughout this thesis.

1.2 Objective and Overview of This Work

The main objective of this work is to continue developing fast, and real-time or semi-real-time Compton imaging algorithms for three-dimensional position-sensitive gamma ray detectors, improve imaging efficiency, explore new imaging capabilities with an updated detector array and readout system, and study how to apply these imaging techniques to real world applications.

Chapter II introduces the three-dimensional position-sensitive room-temperature gamma-ray CdZnTe detector-array system that is used throughout this thesis work. Chapter III gives an overview of the simple back-projection algorithm and explains a method of overlaying an optical image of the environment with the gamma-ray image. Previously in our research laboratory, the MLEM deconvolution, for the spatial as well as the combined spatial-energy domain, was developed for two-interaction events from a single 1.5-cm $\times$ 1.5-cm $\times$ 1-cm position-sensitive room-temperature CdZnTe detector. Because of the increased volume of individual CdZnTe detector modules and the new array configuration, the fraction of events with three or more interactions has increased. In order to make use of these events and improve the imaging efficiency at higher energies, chapter V analytically extends the system response to three-interaction events and further extrapolates to events with any number of interactions. Chapter IV further increases the imaging efficiency by including charge-sharing events in the Compton image reconstruction. Chapter VI explores using the deconvolved spectrum to estimate the presence of an isotope, source intensity, presence of shielding, and shielding material in each direction. Chapter VII demonstrates the capability of visualizing natural radiation background as well as imaging localized sources in the distributed natural radiation background which contains the same isotope. Chapter VIII describes two methods of compensating for the motion of sources. Given the lateral sub-pixel position-sensing capability of the new digital ASIC, chapter IX proposes an algorithm to correct the error in the reconstructed back-projection

cone produced by the difference between the measured centroid of the recoil electron cloud and the true Compton scattering location. Finally, chapter X summarizes the contribution of this thesis work and suggests future work.

CHAPTER II

Three-Dimensional Position-Sensitive Room-Temperature CdZnTe Detector Array

The radiation detection community has long desired a replacement for high purity germanium detectors, which provide very accurate measurements of gamma-ray energy but require liquid nitrogen cooling. Wide-band-gap semiconductor gamma-ray detectors can operate at room temperature but the electrons and holes created by gamma-ray interactions have significantly different mobilities. For this reason, the signals from these detectors are dominated by electron movement and require special single-polarity charge-sensing techniques.

For more than a decade, researchers in our laboratory at the University of Michigan have been using this effect to our advantage by developing a single-polarity charge-sensing technique, which also provides 3-D position sensitivity[22]. This capability is unique to 3-D position-sensitive room-temperature semiconductors and enables the 4π Compton imaging capability in a single crystal.

This chapter describes how to obtain both energy and three-dimensional interaction position information from a pixelated CdZnTe detector. The limitations and non-ideal characteristics of our detector are then discussed. An array of three-dimensional position-sensitive room-temperature CdZnTe detectors is used throughout this entire thesis work.

2.1 Single Polarity Charge Sensing and 3D Position Sensing

Electron-hole pairs are created in a semiconductor detector during the ionizing process when a gamma-ray interacts with the material. An electric field is applied to the detector so the ionized electrons and holes move toward the oppositely charged electrodes. Since the number of electron-hole pairs is proportional to the energy deposited from the gamma ray, the energy of the interaction can be measured.

As the electrons and holes created by a gamma-ray interaction move towards anode and cathode of the detector, signal is induced on the electrodes. The Shockley-Ramo theorem provides a simple way to calculate the magnitude of the induced signal due to the motion of charge carriers [23]. Based on this theorem, one can calculate that the change of the induced signal on a electrode i from a charge q that moves from location x_0 to x_1 is

$$\Delta Q = -q[\phi_i(x_1) - \phi_i(x_0)] \tag{2.1}$$

where $\phi_i(x)$ is the weighting potential at location x. The weighting potential is defined as the potential, after removing all space charges, under the condition that the electrode i is set to unit potential and all other electrodes are set to zero potential.

In a room-temperature semiconductor material, the mobility of holes is much smaller than the mobility of electrons. Several electrode configurations[24; 25; 26; 27; 28] have been developed to overcome this hole-trapping problem. These electrode configurations are designed to be sensitive only to the movement of electrons, hence the name single polarity charge sensing.

Figure 2.1 shows the typical weighting potential for the collecting anode as a function of depth in a pixelated detector [11]. Because of their relative low mobility, holes can be considered stationary during the charge collecting time. As electrons drift towards the collecting anode, the change of the weighting potential on anode is slightly depth dependent while the cathode signal is proportional to the depth of

interaction due to its planar configuration. Therefore, the ratio of the cathode signal amplitude to the anode amplitude can determine the depth of interaction, shown in equation (2.2). He et al. [29] proposed this cathode to anode signal ratio (C/A Ratio, or CAR) method in 1996.

$$\frac{S_C}{S_A} \propto \frac{neZ}{ne} = Z \tag{2.2}$$

in which, S_C and S_A is the induced signal due to the moving of electrons on cathode and anode respectively, n is the number of electrons ionized by the interaction, and Z is the depth of interaction.
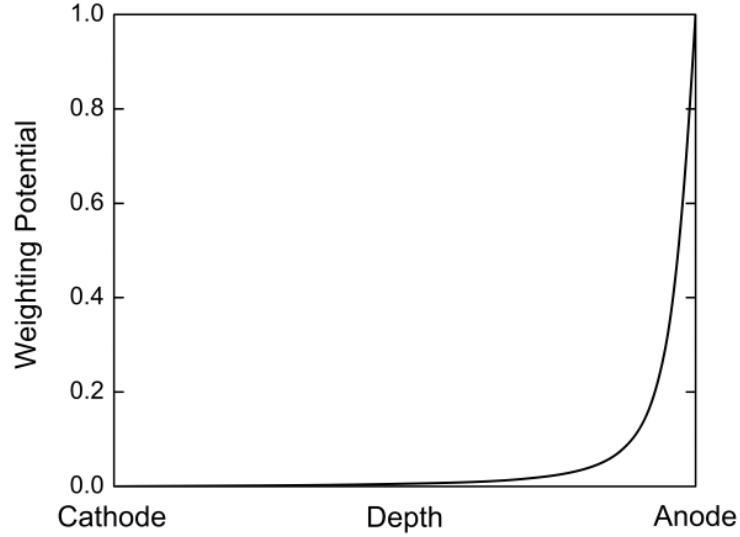
Figure 2.1: The weighting potential as a function of depth for a collecting anode in a pixelated detector.

If there is more than one interaction in the detector, more than one electron cloud is created. The ratio of cathode signal to the summation of all anode signals is an energy-weighted centroid of the depths of the interactions.

$$\frac{S_C}{\sum_{i=1}^{N} S_{Ai}} \propto \frac{\sum_{i=1}^{N} n_i e Z_i}{\sum_{i=1}^{N} n_i e} = \frac{\sum_{i=1}^{N} n_i Z_i}{\sum_{i=1}^{N} n_i} \tag{2.3}$$

where N is the number of pixels that are triggered from the interaction, S_{Ai} denotes the signal from the ith collecting anode, n_i is the number of electrons in the ith

triggered pixel, and Z_i is the depth of interaction in the ith triggered pixel.

Luckily, the individual depth of interaction for multiple-pixel events can be obtained from the drift time of electrons. Because of the weighting potential, as soon as the electrons start moving, a signal is induced on the cathode and the cathode is triggered immediately. The anode will not be triggered until the electrons arrive within one pixel pitch away [11]. Since the electrons drift at a constant velocity under a fixed uniform electric field, the time difference between the cathode trigger and each anode trigger is a measurement of the individual depth of interaction. Combining depth Z with X and Y information from the collecting pixel, three-dimensional position sensitivity is achieved.

2.2   CdZnTe Detector Array System

Unlike HPGe detectors, CdZnTe has a large band gap of 1.6 eV [30], so it can be operated in room temperature. CdZnTe also has high atomic numbers (48, 30, 52) and high density (6 g/cm^3) so it has high stopping power for radiation. In addition, the low average ionization energy (5 eV) per electron-hole pair enables better counting statistics. All of these properties make CdZnTe a very attractive material for radiation detectors.

The three-dimensional position-sensitive room-temperature CdZnTe detectors used in this work all have dimensions of 2 cm $\times$ 2 cm $\times$ 1.5 cm. One of the two square surfaces has a planar cathode and the other one has a pixelated anode. There are 11×11 pixels on the anode surface. Each pixel has a pitch of 1.72 mm. A steering grid is attached to the anode surface between pixels. The cathode is normally biased at -2000 V to -3000 V. The steering grid is biased at a much less negative bias compared to the cathode, typically between -30 V and -200 V, in order to steer the electrons from the gap between pixels to a collecting pixel. The signals from all electrodes are read out from a 128-channel analog application-specific integrated

circuit (ASIC) manufactured by Gamma-Medica Ideas. This ASIC has a dynamic range of 0 to 3 MeV. The design and performance of this ASIC is discussed by Zhang et al. [31]. With this ASIC, the CdZnTe detector is capable of achieving less than 0.7% FWHM at 662 keV for single-pixel events from the entire crystal volume [32]. Another ASIC is developed at the Brookhaven National Laboratory which has lower electronic noise, so it is capable of achieving better energy resolution [33]. There are many considerations regarding how to calibrate the detector to achieve the best spectroscopic performance; the calibration processes are discussed in detail by Zhang [34] and Kaye [35].

In order to improve the spectroscopic and imaging efficiency for high-energy events, increase the average separation distance between interaction, hence improve the image angular resolution, an 18-detector array was recently built in our lab [36]. All detectors trigger together and operate like a single detector. As illustrated in figure 2.2, this detector array consists two layers of 3×3 detectors. The gap between neighbor detectors is 2 mm. The cathodes of both layers are facing outward. The distance between anodes of each layer is either 5.50 cm or 4.09 cm. A similar design with 18 smaller CdZnTe crystals was discussed by Zhang [37].

2.3   Limitations of the Detector system

There are several limitations of the detector system that may compromise the quality of the reconstructed image.

- The peripheral pixels have slightly larger effective volume than inner pixels.

- In order to eliminate noise triggers, a software trigger threshold was set to 30 keV. Interactions with energies less than 30 keV are ignored.

- Multiple interactions can occur under the same pixel. Due to the limitation of the analog ASIC, multiple events will be reconstructed as a single interaction
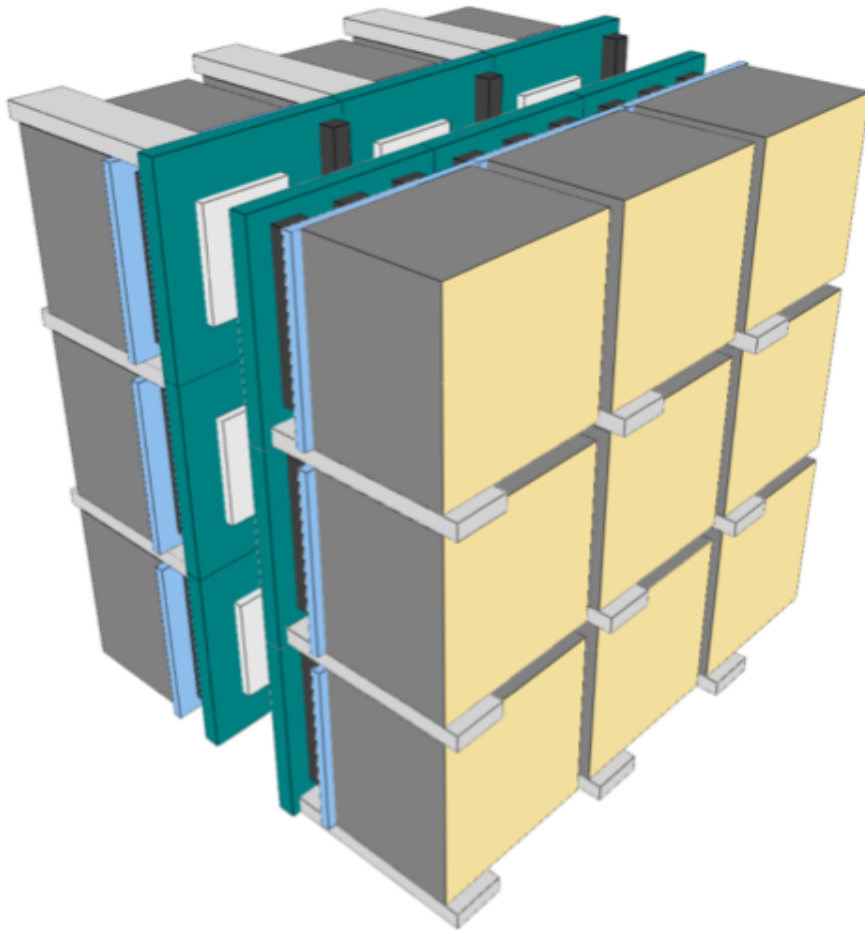
Figure 2.2: A illustration of the 18-detector array.

with the combined energy. For multiple-pixel events, the reconstructed depth from drift time is determined by the interaction that is closest to the collecting anode, so there is a systematic bias for the reconstructed depth towards the anode side.

- Studies have shown that the electron cloud may migrate to its neighbor pixels as it drifts toward the collecting anode pixel from its interaction location [38]. This "pixel-jumping" effect is more severe on the cathode side [35], and behaves differently in different crystals. Furthermore, this effect slightly changes the reconstructed axis of the back-projection cone. However, since the scatter angle is calculated only from the energy depositions, the reconstructed scatter angle is not affected by the pixel-jumping effect. Therefore, unlike some other imaging methods (such as coded aperture), Compton image reconstruction is less sensitive to the pixel-jumping effect for events with large interaction separation distance relative to the pixel pitch.

- The photon which interacts at the near-anode location produces a smaller signal that is sometimes below the trigger threshold. The thickness of this dead layer depends on the photon energy and the software trigger threshold level. An experiment shows that for 662 keV the thickness of the dead layer near the anode surface is approximately 1 mm [39]. This effect has a significant impact on the single-pixel events image reconstruction (attenuation imaging).

- By digitizing the cathode waveform, a new study [40] shows the electric field in some detectors is not uniform under the same pixel. Instead, it is a function of sub-pixel position. As a consequence, the reconstructed depth is also a function of sub-pixel interaction position. This effect will create a oval-shaped image for a point source, which will be discussed in section 3.3. This effect is impossible to correct with the current analog ASIC.

- The electron cloud diffuses as it drifts towards the anode. Due to the long drifting distance, the electron cloud created at the cathode side has a higher probability to be shared by multiple neighboring pixels.

CHAPTER III

Compton Camera

3.1 Simple Back-Projection

As illustrated in figure 3.1, when a gamma ray with initial energy E_0 Compton-scatters in the detector material with a scatter angle of θ, part of the gamma ray's energy E_1 is transferred to a scattering electron which recoils and is ejected from its atom. From the conservation of energy and momentum, the Compton equation can be derived as

$$E_2 = \frac{E_0}{1 + \frac{E_0}{m_e c^2}(1 - \cos\theta)} \tag{3.1}$$

in which, E_2 is the energy of the scattered photon, and $m_e c^2$ is the rest mass energy of an electron.

If the scattered photon with the remaining energy E_2 interacts with the detector again in a photoelectric interaction, the scatter angle θ can be uniquely determined by the Compton scattering equation.

$$\theta = \cos^{-1}\left(1 - \frac{E_1 m_e c^2}{E_0(E_0 - E_1)}\right) \tag{3.2}$$

A cone can then be reconstructed with the calculated scatter angle θ and the axis along the line between two interaction locations, as shown in figure 3.2. The incident photon may originate from any direction on the reconstructed cone unless the direction of

13
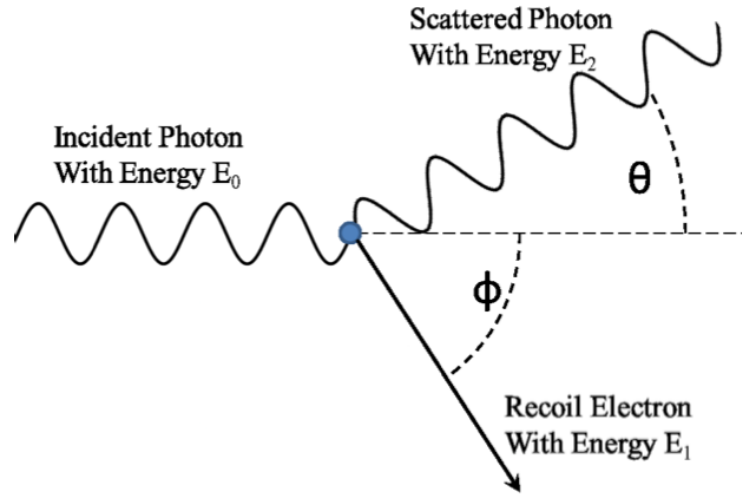
Figure 3.1: An incident photon with energy E_0 deposits energy E_1 in a Compton scattering interaction with a scatter angle θ.
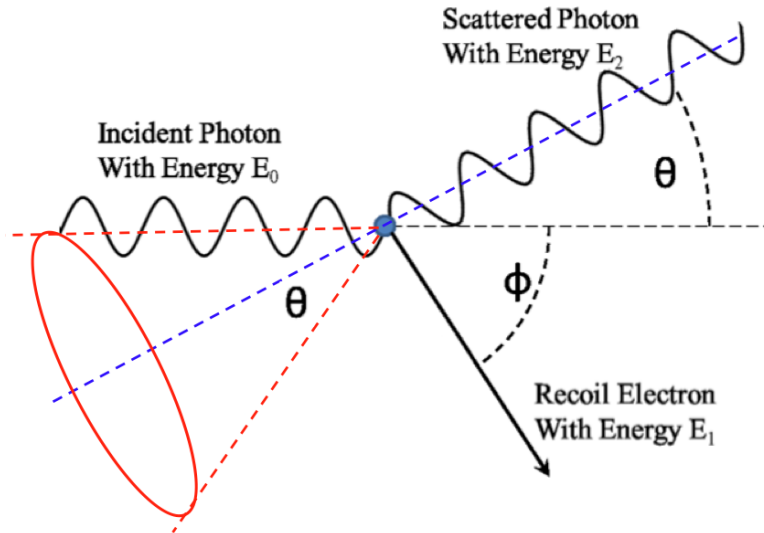
Figure 3.2: A cone can be back-projected with the calculated scatter angle θ and the axis along the line between two interaction locations.

the recoil electron can be measured [21]. Unfortunately, the size of the electron cloud is too small for the position resolution of our system to determine the recoil electron direction. However, the intersection of the cones from multiple incident photons points the source direction. This algorithm is known as simple back-projection (SBP). The angular resolution of SBP with a single CdZnTe detector with dimensions of 2 cm × 2 cm × 1.5 cm is about 40 degrees.

3.2   Sequence Reconstruction

Due to the limited timing resolution of our detector system, it is impossible to perform the time-of-flight measurement of the event sequence. So for an N-pixel event, $N!$ possible sequences need to be considered for the image reconstruction. The design objective of the SBP algorithm is to be simple and fast to calculate; so only the most likely sequence is used for each event.

For two-interaction events, we first confirm each sequence is energetically possible by checking if any interaction has an energy above the Compton edge (the maximum energy a photon can deposit in a Compton-scattering event). If both interactions have energies below the Compton edge, we usually favor back scattering (by choosing the sequence with the first interaction having a higher energy) due to the fact that a scattered photon with higher energy would be more likely to escape from our small detector. Another method is to select the sequence with higher probability. The two interactions and the penetration distance between interactions are considered in the probability calculation. These two methods demonstrate similar performance for identifying the correct sequence [11].

For three-or-more-interaction events, we also have two options. The first one is a similar probability-based method which accounts for all interactions and penetration distances between interactions. The second method calculates a figure of merit (FOM) for each sequence based on the agreement between the calculated scatter an-

gles from energy depositions using the Compton formula and the measured scatter angles from the interaction locations. The sequence having the highest FOM is used for reconstructing the back-projection cone for that event. A simulation study shows that for the 18-detector-array system, the second method has a better performance for 5-or-more pixel events [41].

3.3   The Uncertainty of the Back-Projection Cones

Due to measurement uncertainties in the reconstructed energy and position, only a few back-projection cones pass the source direction. In order to quickly locate the source direction using SBP with a limited number of events, a Gaussian-shaped cone width is added to each back-projection cone. The cone width is determined by its angular resolution measurement (ARM) which is the angle between the reconstructed back-projection cone and the actual source direction [11]. Energy and position reconstruction uncertainty, Doppler broadening, and coherent scattering contribute to the ARM.

Energy uncertainty changes the reconstructed scatter angle of the back-projection cone, so it contributes equally to all directions. Position uncertainty affects the cone axis. In an example of a two-interaction event with interactions at locations (x_1, y_1, z_1) and (x_2, y_2, z_2), the polar angle θ and the azimuthal angle ϕ of the cone axis can be calculated as

$$\theta = \tan^{-1} \frac{z_2 - z_1}{\sqrt{(x_2 - x_1)^2 + (y_2 - y_1)^2}} \tag{3.3}$$

and

$$\phi = \tan^{-1} \frac{y_2 - y_1}{x_2 - x_1} \tag{3.4}$$

It can be seen that only the polar angle is affected by the depth uncertainty. We have observed that some detectors tend to produce elongated hot spots from a point source while other detectors produce more circular hot spots. As demonstrated in

16

figure 9.7(a) the elongated hot spot usually has a larger polar FWHM than its azimuthal FWHM. This effect can be verified by simulating different detectors with different depth uncertainties. Figure 3.3 shows the SBP image from events that are generated by a simulated detector with perfect depth resolution measuring a Cs-137 point source. The SBP image from the same point source measured by a simulated detector with a depth uncertainty of 3 mm is shown in figure 3.4. The reconstructed hot spot from the detector with 3 mm depth uncertainty clearly has a bigger extend in polar direction than the detector with perfect depth resolution. Therefore, an elongated polar FWHM can be used as an indication for poor depth reconstruction.
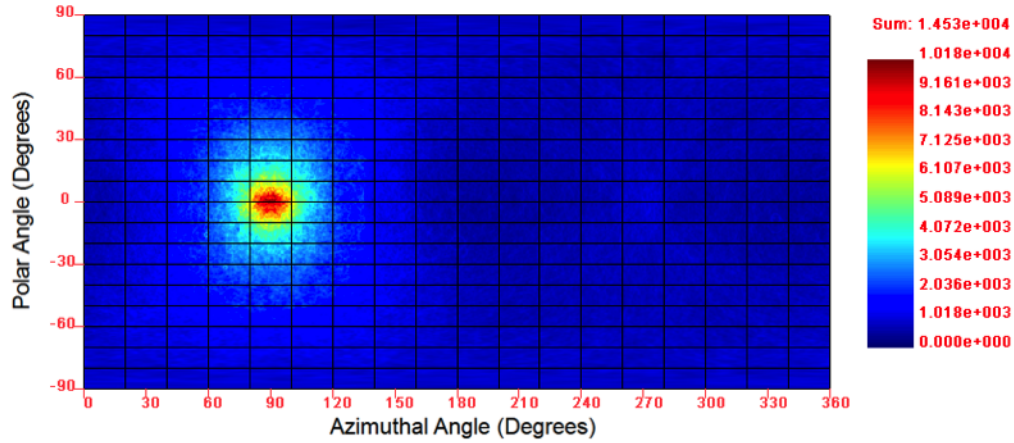
Figure 3.3: The reconstructed image with a simulated CdZnTe detector with perfect depth resolution.

3.4   Overlaying Radiation Images with Optical Images

The reconstructed source image is normally shown as an intensity map with axes corresponding to polar and azimuthal angles which represent the 4π field-of-view of the detector. In the application of searching and locating a source, it is inconvenient and tedious to locate a source by a set of polar and azimuthal angles in the detector's reference frame. Therefore, it is desired to mount a camera with the detector and
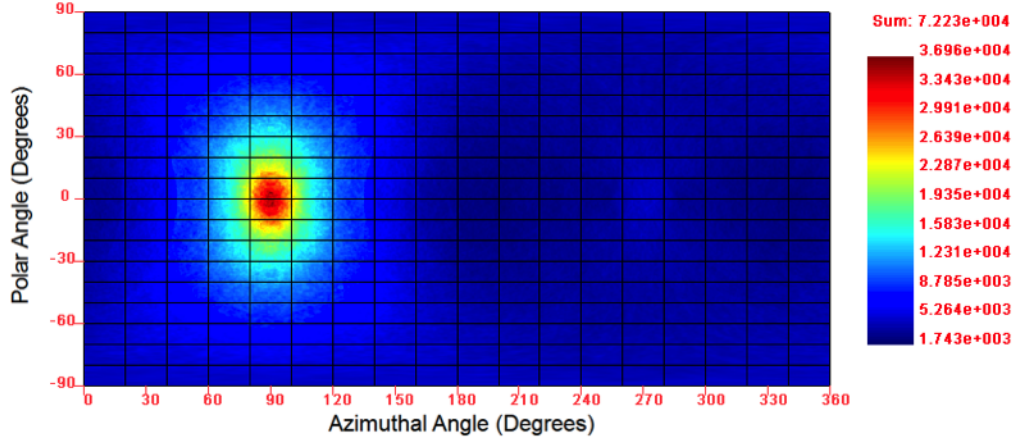
Figure 3.4: The reconstructed image with a simulated CdZnTe detector with a depth
uncertainty of 3 mm.

overlay the reconstructed radiation image with the optical image. The operator may simply look at the combined image and say: "Sir, there is a source in the left pocket of your pants."

In order to prove the concept, a 0-360 Panoramic Optic™ panoramic lens was mounted on a digital camera. The lens was placed at the same location as the center of detector head to minimize parallax effects. The set up is shown in figure 3.5. The field of view of this lens ranges from 0 to 360 degrees in the azimuthal direction and 37.5 to 152.5 degrees in the polar direction. Fig 3.6 shows a raw picture of our lab which was taken with the panoramic lens. After unwrapping the picture, a panoramic view is achieved as in figure 3.7.

In order to correctly overlay the radiation image with the optical image, a 30-μCi Cs-137 source was placed at several locations in the field of view of the lens. A calibration was performed to match the reconstructed hot spot with the source location in the optical image by flipping and rotating the radiation image. Two black bands were added to the combined images to match the 4π field of view of the Compton camera. The calibration process is shown in figures 3.8 and 3.9.

18

After performing this calibration, figure 3.10 can be achieved. The hot spot correctly overlaps with the left pocket of my pants which contains a 10-μCi Cs-137 source. Figure 3.11 shows the combined optical-radiation image from a three-source measurement with a 30-μCi Na-22, a 10-μCi Ba-133 and a 1-μCi Co-60 source. The radiation image from the photopeak energy windows of Ba-133, Na-22 and Co-60 are color-coded in red, green and blue, respectively.
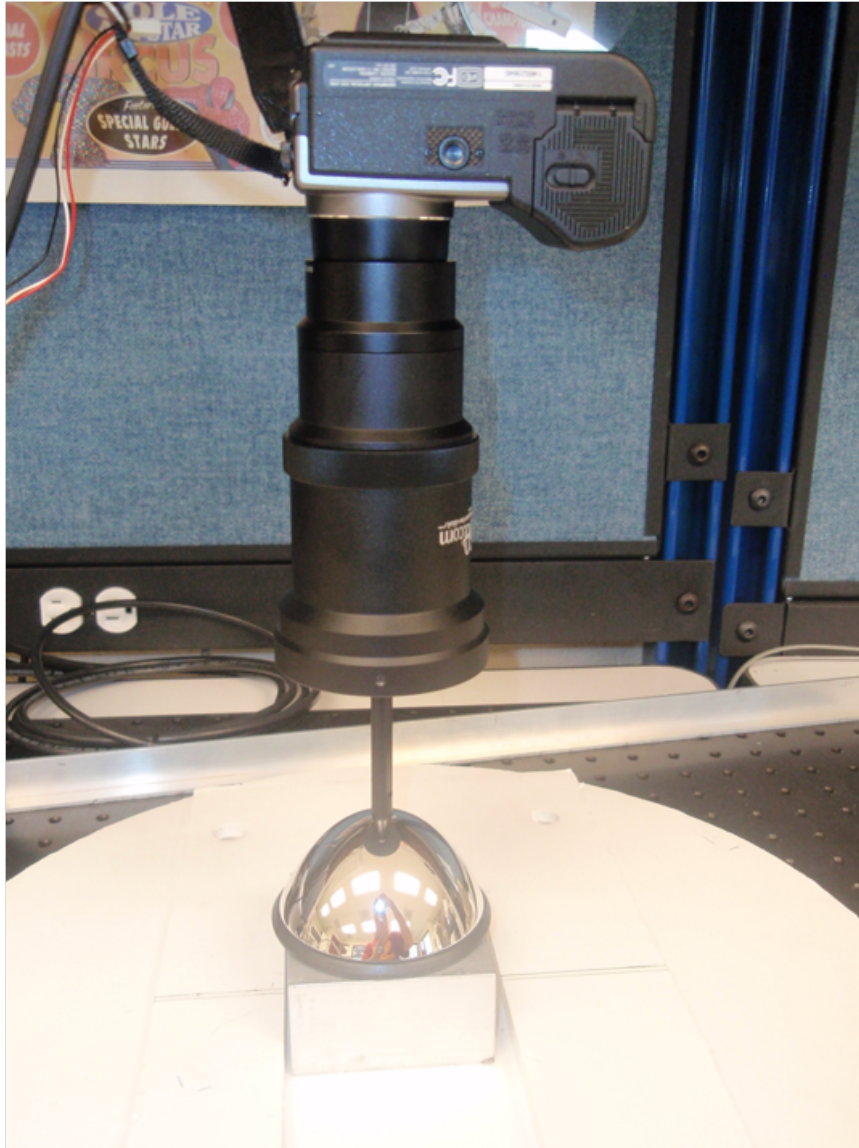
Figure 3.5: A panoramic lens was mounted on a digital camera via an adaptor so it is capable of focusing on the surface of the lens.

Figure 3.6: The panoramic picture before unwrapping.

Figure 3.7: The unwrapped panoramic picture.
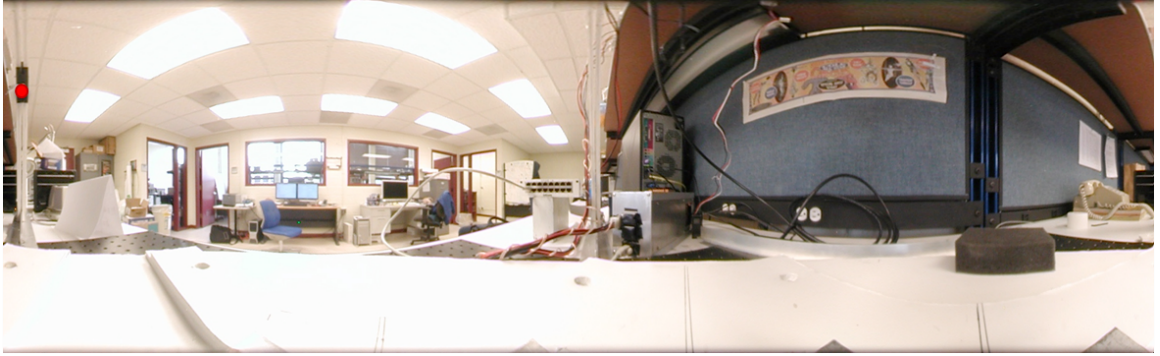
(a) A red disk Cs-137 source was placed at position 1.

(b) The radiation image was rotated to match the reconstructed hotspot with the location of the red disk in optical image.

Figure 3.8: A red disk Cs-137 source was placed at position 1 to calibrate the radiation image to match the optical image. The radiation image was created from about 2000 events in the Cs-137 photopeak using the MLEM deconvolution in the spatial domain.
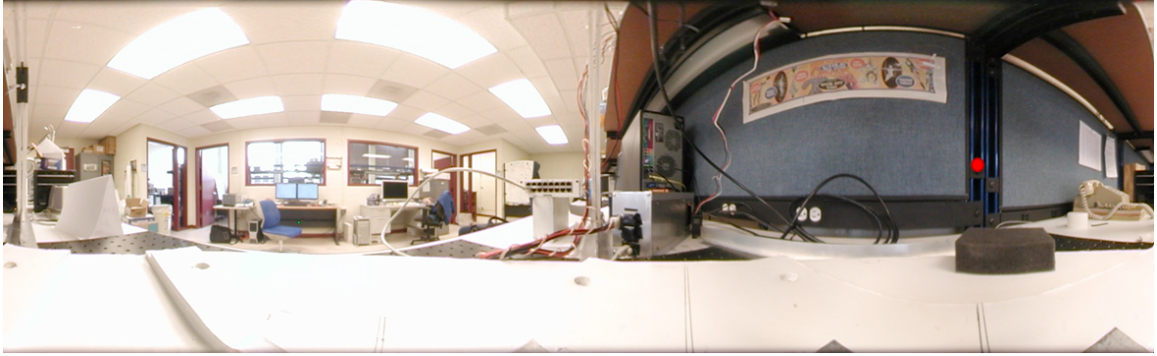
(a) A red disk Cs-137 source was placed at position 2.

(b) The radiation image was rotated/flipped to match the reconstructed hotspot with the location of the red disk in optical image.

Figure 3.9: The red disk Cs-137 source was moved at position 2 to calibrate the radiation image to match the optical image. The radiation image was created from about 2000 events in the Cs-137 photopeak using the MLEM deconvolution in the spatial domain.

Figure 3.10: The combined image from a source-in-my-pocket scenario. A 10-μCi Cs-137 source was used in this measurement. 622 events were used in the Compton image reconstruction.

Figure 3.11: The radiation image from the photopeak energy windows of Ba-133, Na-22 and Co-60 are color-coded in red, green and blue, respectively.

CHAPTER IV

Improvement of Compton Imaging Efficiency by Using Side-Neighbor Events

An electron cloud can be collected by and shared between several neighboring pixels. These charge-sharing events can be produced from several reasons: a large electron cloud has a size comparable to a pixel pitch; the electron cloud is located directly below the gap between pixels; the electron cloud defuses while drifting towards the anode; and the x-ray emission from a photoelectric interaction. The charge-sharing effect is not desired for the Compton image reconstruction since it does not contain any useful Compton scattering information but produces multiple-pixel events. The charge-sharing effect can be reduced by increasing the pixel pitch of the detector. However, increasing the pixel size will cause poorer energy resolution because it reduces the small pixel effect [28], and increases the leakage current collected by each pixel. With our current detector configuration, over half of the multiple-pixel events at 1333 keV are side-neighbor events. These events were excluded from the Compton image reconstruction prior to the work presented in this dissertation.

Theoretically, charge-sharing interactions should be combined into a single interaction because they are produced from a single electron cloud. However, it is almost impossible to differentiate charge-sharing events from side-neighbor Compton scattering events due to the limitation of the analog readout system. This chapter separates

the simulated side-neighbor events into different categories based on the type and the sequence of the interactions, and explores how to mine out the most side-neighbor events that can produce a correct source image using SBP. A method is then proposed and evaluated using experimental data.

4.1 Side-Neighbor Events from Simulated Sources

Our group has developed a program to simulate the entire response of our system, from the generation, movement, and induction of charge to the readout process of the current analog ASIC [42]. This simulation software can be validated for the purpose of this study by correctly reproducing the time-amplitude-walk effect for both non-neighbor and side-neighbor events [43].

4.1.1 662 keV

Using this software, we simulated the detector and the ASIC response from a point source that emits 662 keV photons. The three-pixel side-neighbor events that include a single pair of neighboring pixels from the simulation result were then divided into six categories based on the type of interaction that produces the side-neighbor events, as shown in table 4.1. We have three possible option for each event: use the side-neighbor interactions in the image reconstruction without modification (assume they are side-neighbor Compton events), combine side-neighbor interactions to one interaction (assume they are charge-sharing events), or exclude from the image reconstruction. Categories 1 and 4 are charge-sharing events, so the averaged depth and summed energy in the side-neighbor pixels should be input to the imaging algorithm as a single interaction. Categories 2 and 5 are three-interaction Compton events, so they can be used in the image reconstruction directly. Category 3 and 6 are the events that undergo both charge sharing and Compton scatter in the side-neighbor pixels.

In order to verify these theoretical predictions, we first combined all side-neighbor

25

Table 4.1: The Definitions and the Event Fractions of Categories for Three-Pixel Side-Neighbor Events at 662 keV

	Charge sharing	Compton scattering	Others
1st interaction is involved in the side-neighboring pixels	cat.1: 22.4%	cat.2: 18.5%	cat.3: 5.2%
1st interaction is not involved in the side-neighboring pixels	cat.4: 16.5%	cat.5: 25.7%	cat.6: 11.7%

interactions in each category and performed image reconstruction with these new two-interaction non-side-neighbor events. We then directly reconstructed images from each category without combining side-neighbor events.

Figure 4.1 and 4.2 shows the reconstructed image using the SBP algorithm after combining all side-neighbor interactions in each category. The averaged depth and summed energy in the side-neighbor pixels are input to the imaging algorithm as a single interaction. After combining side-neighbor interactions, categories 1 and 4 make a correct image as expected. In addition, categories 5 and 6 make a correct image as well. The first interaction in categories 5 and 6 is a Compton interaction without a signal from a side-neighbor pixel. By combining the second and the third interactions, the cone angle remains unchanged due to the fact that the cone angle is only dependent on the total energy and the energy deposition of the first Compton scatter. Since the separation distance between the side-neighboring second and third interaction is small compared to the separation distance between the first and the second interaction locations, the cone axis has a small change in both categories 5 and 6 after combining side-neighbor interactions. As a consequence, the hot spot in figures 4.2(b) and 4.2(c) is slightly larger than figure 4.2(a).

If all six categories are all treated as three-interaction Compton events, figures 4.3 and 4.4 can be achieved, which show that only categories 4, 5 and 6 reconstruct a correct source image. In these three categories, the first interaction is not one of the side-neighboring pixels, so the first interaction is a Compton scatter. For
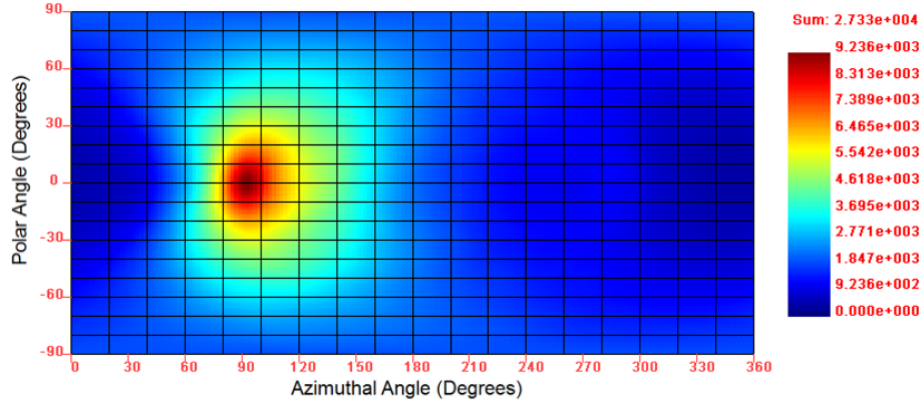
(a) Category 1
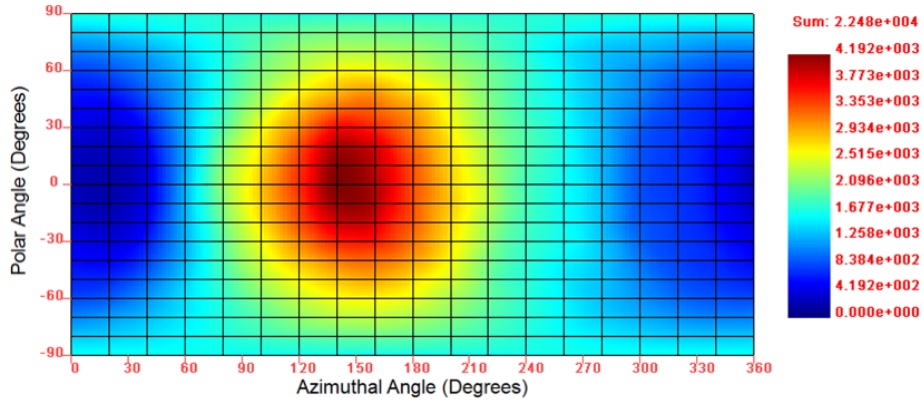
(b) Category 2
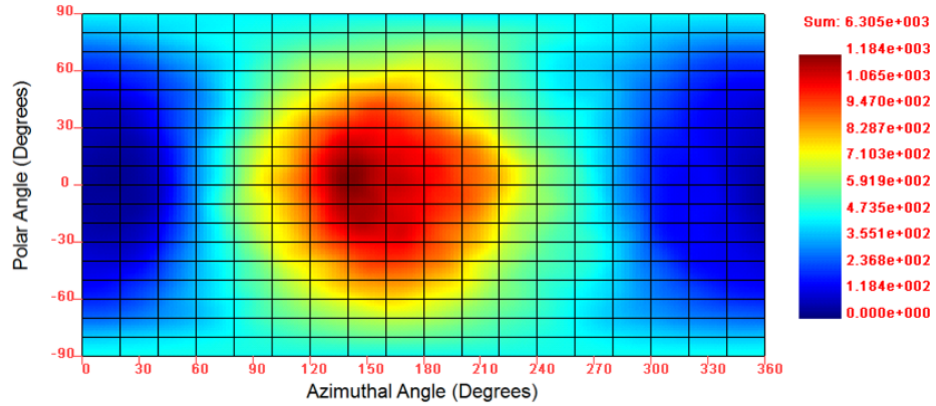
(c) Category 3

Figure 4.1: All side-neighbor interactions are combined into a single interaction. The SBP image reconstruction is performed with these combined 2-interaction events (originally 3-pixel events) from categories 1 to 3.
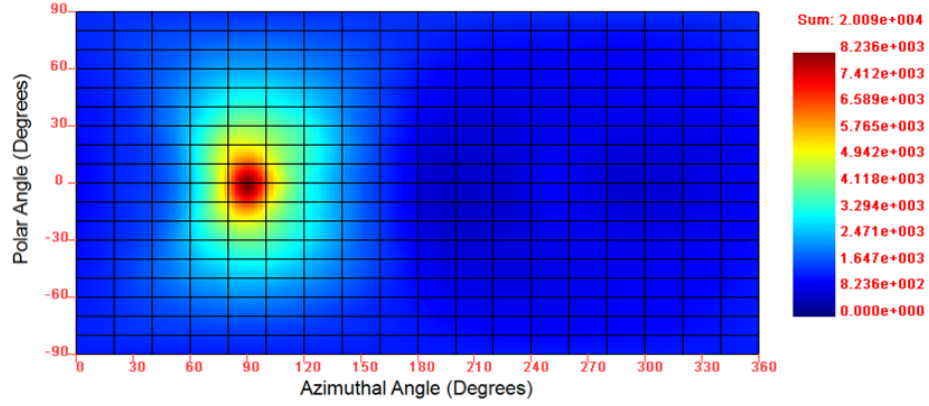
(a) Category 4
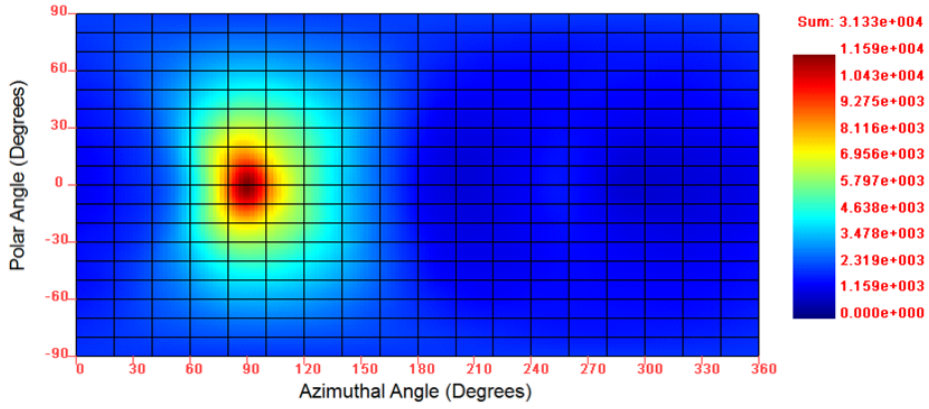
(b) Category 5
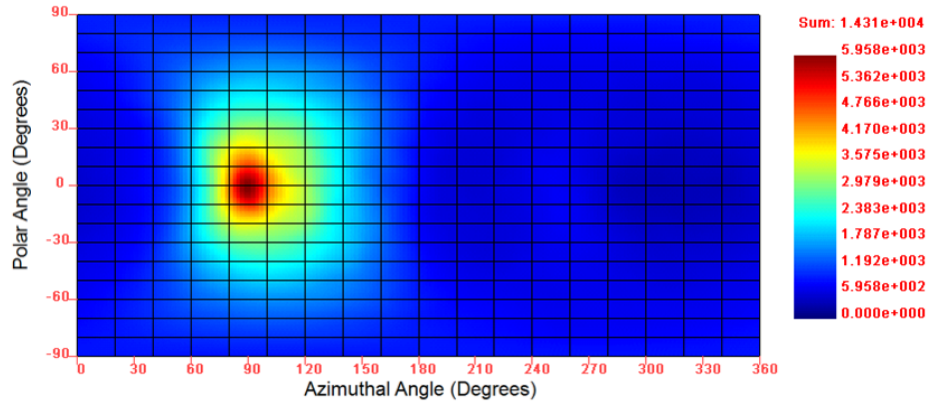
(c) Category 6

Figure 4.2: All side-neighbor interactions are combined into a single interaction. The SBP image reconstruction is performed with these combined 2-interaction events (originally 3-pixel events) from categories 4 to 6.

the same reason described in the last paragraph, the reconstructed cone angles are correct in categories 4, 5 and 6. In category 2, the side-neighbor interactions are from true Compton interactions so it can be directly used in the imaging reconstruction. However, category 2 produces a very poor image due to large cone-axis uncertainties which is introduced by the short separation distance between the first and the second interaction which are in side-neighboring pixels.

To summarize, category 1 can only produce a correct image after combining side-neighbor interactions. Categories 2 and 3 will never make a decent image and should be excluded from the SBP reconstruction. Finally, categories 4, 5 and 6 can make a correct image regardless if the side-neighbor interactions are combined. Figure 4.5, 4.6 and 4.7 show the distribution of the depth difference between side-neighbor interactions for each category. No region can be drawn to clearly separate categories 1 from category 4, category 2 from category 5, or category 3 from category 6. It is possible to differentiate category 2 and 3 from category 1 such that events with large separation distances would be discarded. However, this would result in the loss of an roughly equal number of good events from categories 5 and 6. Therefore, in order to improve the imaging efficiency, the best strategy with the analog ASIC is to combine all side-neighbor events since it has the highest event fraction that produces a correct image. From table 4.1, this correctly-combined fraction for three-pixel side-neighbor events at 662 keV is about 76.3%.

4.1.2   1333 keV

A similar analysis was performed with a simulated point source which emits 1333 keV photons. The same conclusion can be drawn that the most effective way to use the side-neighbor events is to combine all side-neighbor interactions. From table 4.2, about 76.5% of the combined three-pixel side-neighbor events are capable of producing a correct image.
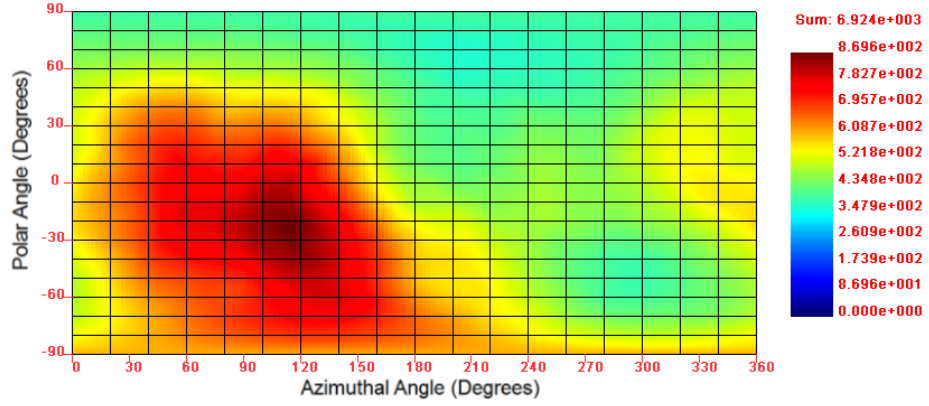
(a) Category 1
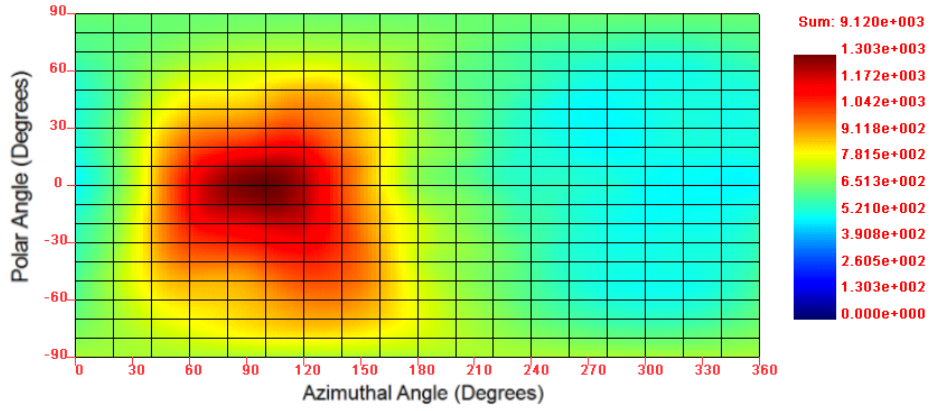
(b) Category 2
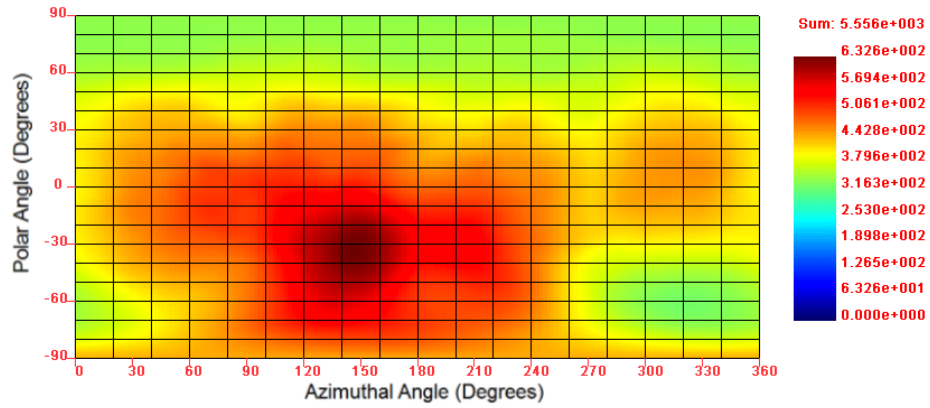
(c) Category 3

Figure 4.3: The SBP image reconstruction is directly performed with three-pixel side-neighbor from categories 1 to 3. The events are from a simulated point source that emits 662 keV photons.
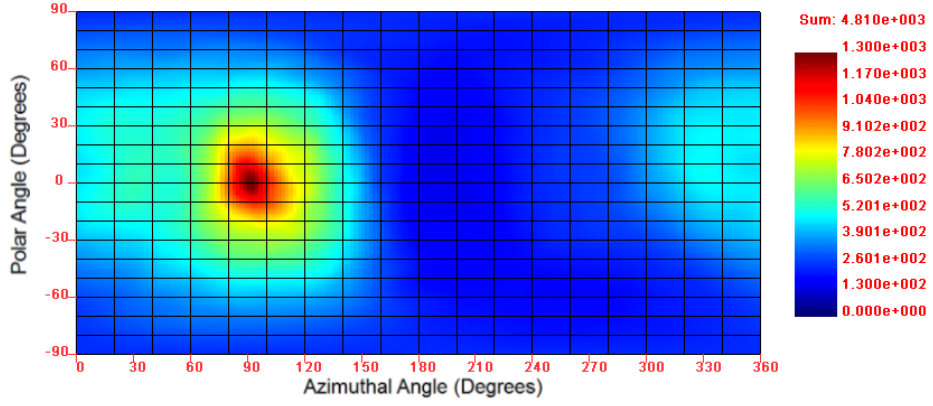
(a) Category 4
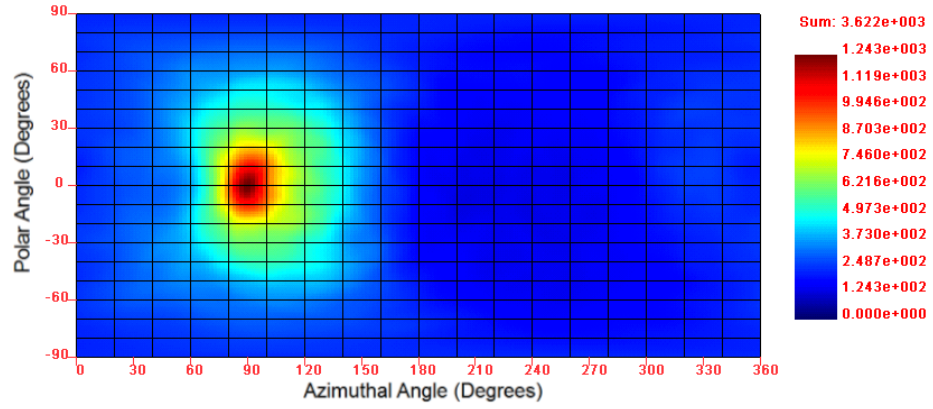
(b) Category 5
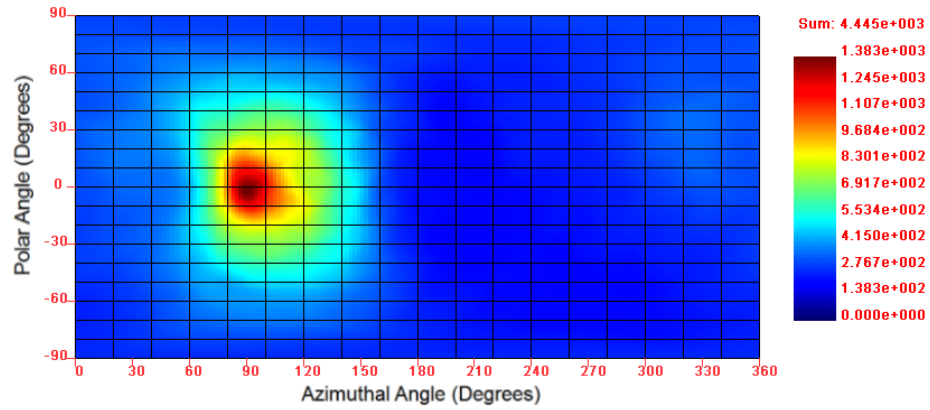
(c) Category 6

Figure 4.4: The SBP image reconstruction is directly performed with three-pixel side-neighbor from categories 4 to 6. The events are from a simulated point source that emits 662 keV photons.
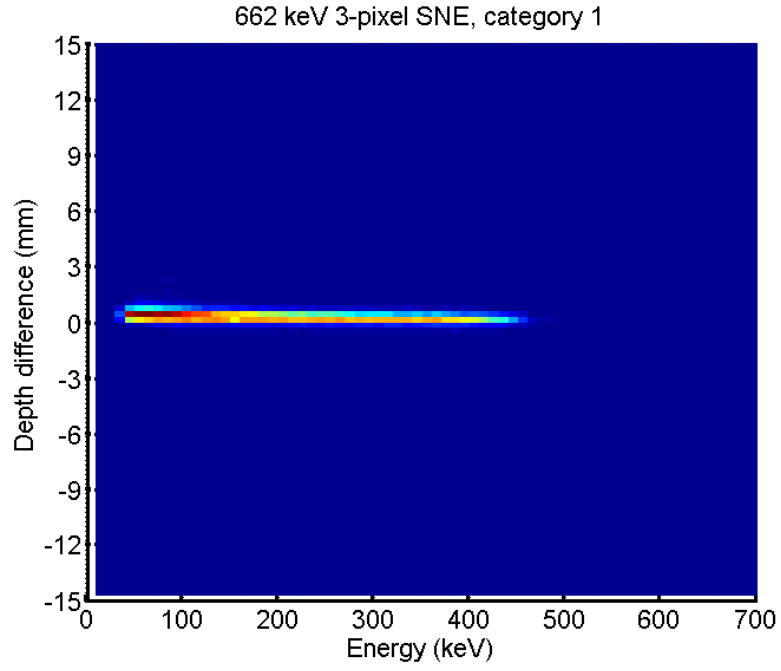
(a) Category 1
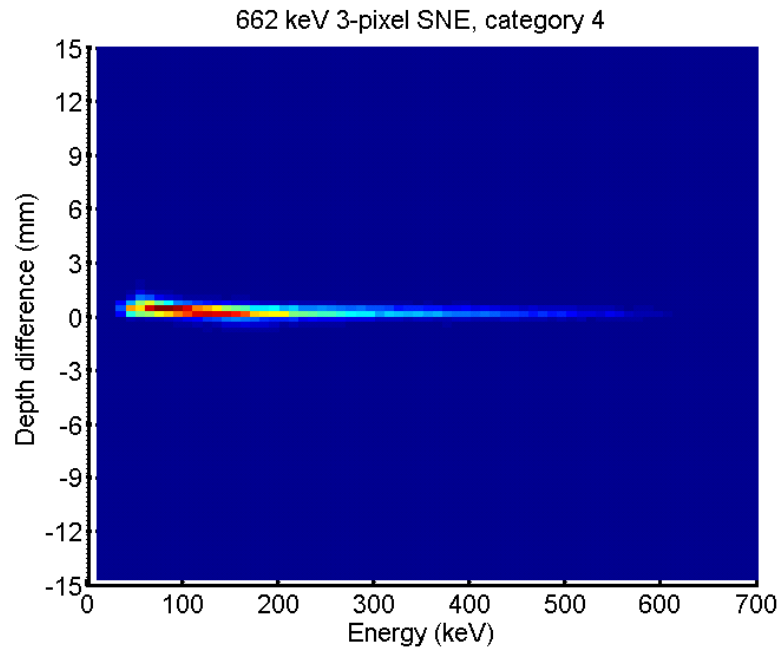
(b) Category 4

Figure 4.5: The distribution of the depth difference between two side-neighbor interactions at 662 keV.
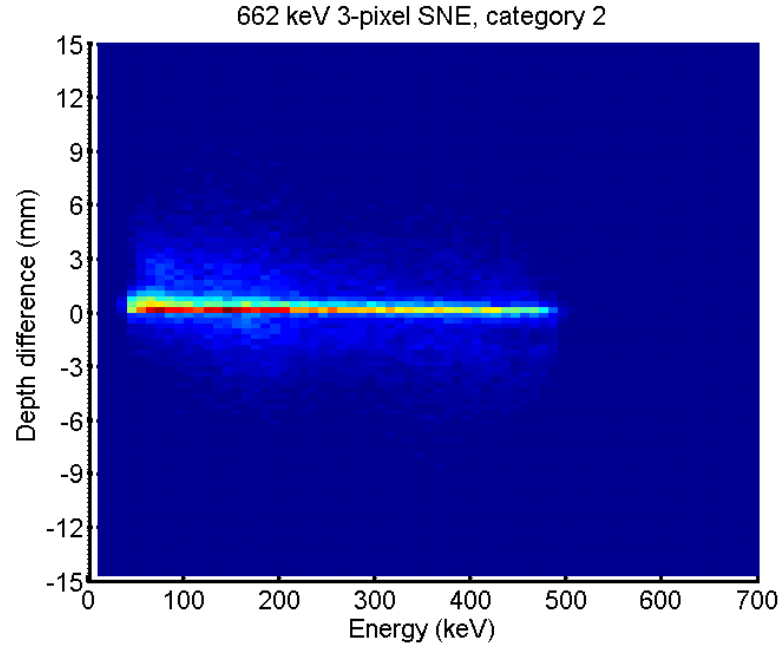
(a) Category 2
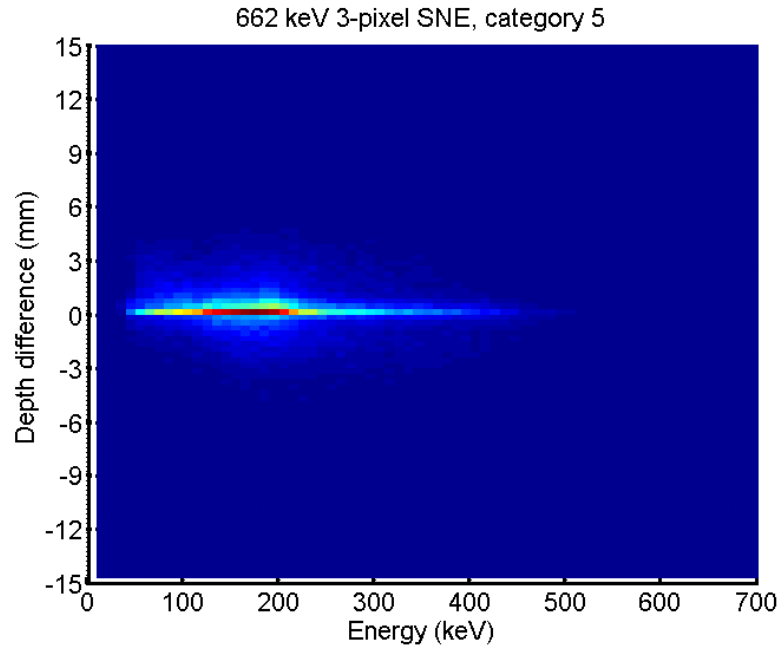
(b) Category 5

Figure 4.6: The distribution of the depth difference between two side-neighbor interactions at 662 keV.
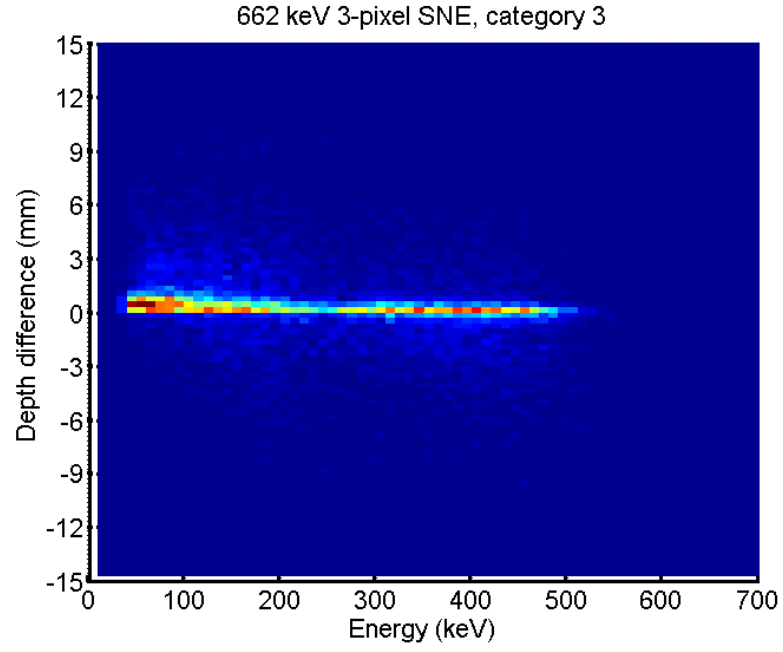
(a) Category 3
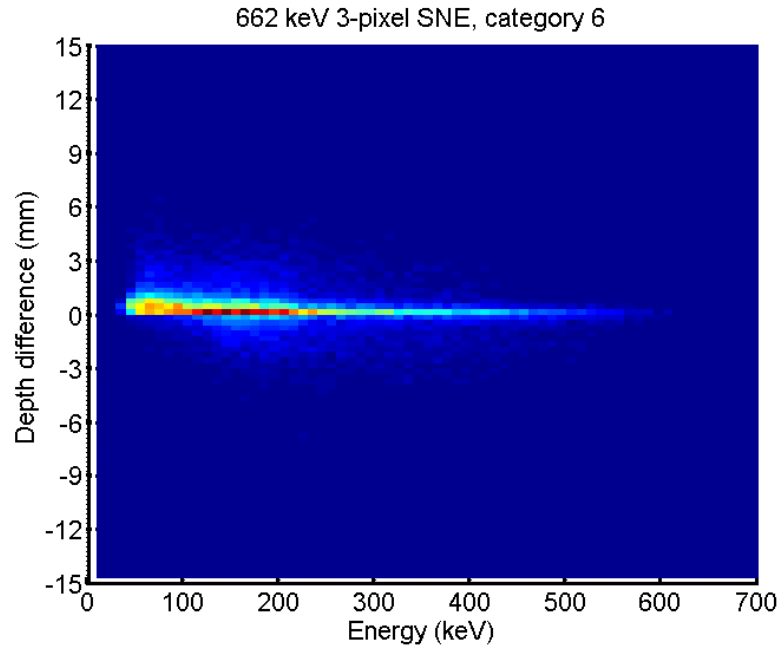
(b) Category 6

Figure 4.7: The distribution of the depth difference between two side-neighbor interactions at 662 keV.

All of these conclusions still hold for side-neighbor events with more than three triggered pixels as long as two or more unique interaction locations can be identified.

Table 4.2: The Definitions and the Event Fractions of Categories for Three-Pixel Side-Neighbor Events at 1333 keV

	Charge sharing	Compton scattering	Others
1st interaction is involved in the side-neighboring pixels	cat.1: 44.8%	cat.2: 14.1%	cat.3: 9.4%
1st interaction is not involved in the side-neighboring pixles	cat.4: 10.0%	cat.5: 13.5%	cat.6: 8.2%

4.2   Performance Verification with Measurements

A 10-μCi Cs-137 and a 1-μCi Co-60 point source is measured separately. Figure 4.9 shows the SBP image only using 25023 side-neighbor two-, three- and four-interaction events in the energy window from 600 keV to 720 keV from the Cs-137 measurement after combining the neighboring interactions. Figure 4.9 has a similar image quality compared to figure 4.8 which uses 55252 two-, three- and four-interaction non-side-neighbor events from the same measurement in the same energy window.

Figure 4.11 shows the SBP image only using 3996 side-neighbor two-, three- and four-interaction events in energy window from 1250 keV to 1400 keV from the Co-60 measurement. Figure 4.11 has a similar image quality compared to figure 4.10 which uses 2491 two-, three- and four-interaction non-side-neighbor events from the same measurement in the same energy window.

Thus, by combining all side-neighbor interactions, the imaging efficiency at 662 keV and 1333 keV is improved by about 45% and 160% respectively with no degradation of the image quality.

To use these side-neighbor events in probabilistic methods such as the MLEM algorithm which will be discussed in chapter V, both side-neighbor Compton scat-

ter and charge sharing possibilities must be considered and weighted based on their probabilities.
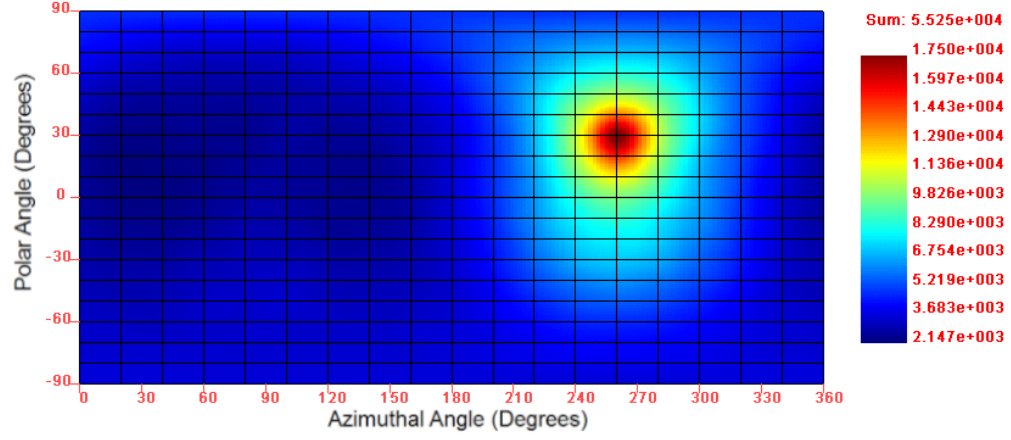
Figure 4.8: A SBP image with a Cs-137 source using 55252 two-, three- and four-interaction non-side-neighbor events. An energy window of 600 keV to 720 keV is used.
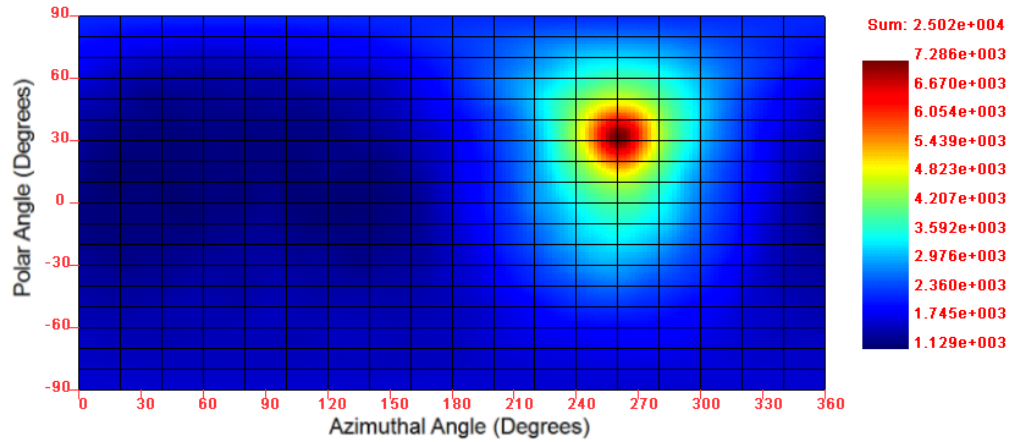
Figure 4.9: A SBP image using 25023 two-, three- and four-interaction side-neighbor events from the same measurement as figure 4.8. An energy window of 600 keV to 720 keV is used.
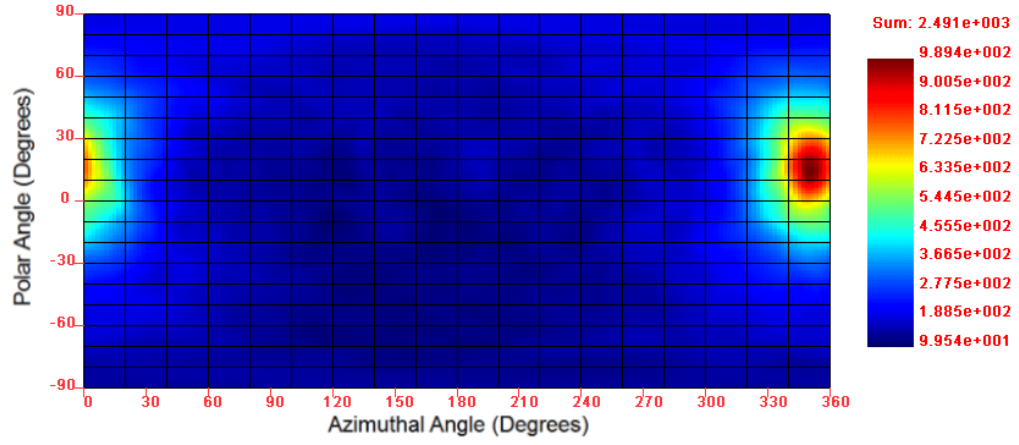
Figure 4.10: A SBP image with a Co-60 source using 2491 two-, three- and four-interaction non-side-neighbor events. An energy window of 1250 keV to 1400 keV is used.
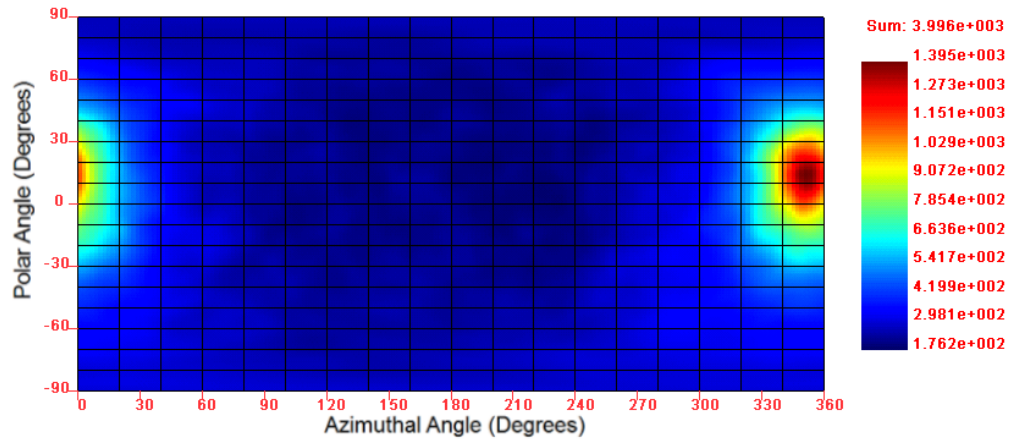
Figure 4.11: A SBP image using 3996 two-, three- and four-interaction side-neighbor events from the same measurement as figure 4.10. An energy window of 1250 keV to 1400 keV is used.

CHAPTER V

Maximum-Likelihood Deconvolution in the Spatial and Spatial-Energy Domain for Events with Any Number of Interactions

5.1   Maximum-Likelihood Expectation-Maximization Algorithm

The image reconstruction can be described as estimating the source distribution for which the set of measured events is most probable.

$$\mathbf{f} = \arg \max_{\mathbf{f} \geq 0} p(\mathbf{g}; \mathbf{f}) \tag{5.1}$$

in which, $\mathbf{f}$ is the source distribution in the image space we are trying to estimate and $\mathbf{g} = \{g_1, g_2, ..., g_I\}$ is the possible measurements. g_i is the number of occurrence for a measurement i.

The imaging system can be simplified to be represented by a linear model between the measurement and the source distribution. Assume the image space can be discretized into J pixels, the expected number of counts in each measurement bin is

$$\bar{\mathbf{g}}_{[I \times 1]} = \mathbf{t}_{[I \times J]} \mathbf{f}_{[J \times 1]} \tag{5.2}$$

in which, **t** is the system response matrix.

In this work, the measurements attributes are interaction energies and positions of every measured event, $g_i = \{\vec{E}, \vec{r}\}$, and the image space parameters are defined as directional 2D image pixels, or combined direction and source-energy bins in the energy-imaging integrated deconvolution (EIID) method which will be discussed in following sections in this chapter. Other ways one might describe the attributes of the measurement could be the amplitude of each pulse from the preamplifier and the timing signals, and the image space could be defined in three dimensions or isotope bins [44].

This type of parameter estimation problem is well-studied in the medical imaging field [45]. The widely-used maximum-likelihood (ML) method solves this problem from a statistical point of view. The ML solution produces less noise than other ways of directly solving this problem [46; 47; 5].

Since the number of photons emitted from each pixel is a Poisson random variable and the recorded attributes are assumed to be conditionally independent, the logarithmic likelihood can be derived as [11]

$$\mathbf{L}(f) = \sum_{i=1}^{I} \left[-\sum_{j=1}^{J} t_{ij} f_j + g_i \ln \sum_{j=1}^{J} t_{ij} f_j - \ln(g_i!) \right] \tag{5.3}$$

where t_{ij} is the probability of recording an event i given that it is from a photon in the direction j, and f_j is the source intensity in the direction j that we are trying to estimate.

Expectation maximization (EM) is a popular iterative algorithm that can be used to maximize the logarithmic likelihood in equation (5.3) [48; 49; 50]. The MLEM iterative solution for this photon-emission imaging problem is [11; 44]

$$f_j^{n+1} = \frac{f_j^n}{s_j} \sum_{i=1}^{I} \frac{g_i t_{ij}}{\sum_k t_{ik} f_k^n} \tag{5.4}$$

39

where f_j^n is the estimated intensity in the direction j at the nth iteration, and $s_j = \sum_{i=1}^{I} t_{ij}$ is the sensitivity factor which is the probability that a gamma ray emitted from j is detected as any event i.

In our detector-array system, there are 18 detectors, and 121 pixels per detector. If 15 depth bins and 500 energy bins are used, there are $(121 \times 15 \times 500 \times 18)^2 \approx 2.7 \times 10^{14}$ different possible measurement combinations for a two-interaction event. Practically, in order to get a solution in a reasonable time, we generally use up to ten thousand events for each image reconstruction. Therefore, our $\mathbf{g}$ matrix is extremely sparse. Instead of storing the number of occurrence in the bin of all possible measurements, we store our events in list-mode [51; 48; 46; 52]. In this way, $\mathbf{g}$ becomes a list of measured events and the term g_i in equation (5.4) can be replaced by 1. So the list-mode MLEM iterative solution is

$$f_j^{n+1} = \frac{f_j^n}{s_j} \sum_{i=1}^{I} \frac{t_{ij}}{\sum_k t_{ik} f_k^n} \tag{5.5}$$

where I becomes the number of measured events.

Due to the limitation of the timing resolution of our system, it is challenging to observe the sequence of the interactions in an event. Several algorithms have been developed to determine the interaction sequence with the maximum probability based on the interaction positions and energies [17; 53; 54]. However, the accurate system model should include all possible sequences. In this work, we consider all energetically possible sequences. Each sequence is weighted based on its probability. The image sharpens when more number of EM iterations are performed; however, the statistical noise increases as well. Usually, more iterations are performed than necessary so that the user can select the optimal iteration by eye where the best image resolution is achieved at an acceptable noise level.

5.2 System Response Function for Three-interaction Events in a Detector-Array System

In order to use the EM method, system matrix $\mathbf{t}$ needs to be obtained. The number of possible measurements is too large to be simulated and stored. In this work, the system matrix element for each measured event is analytically modeled.

The system response function t_{ij} is defined as the probability that a photon with a certain incident energy E_0 from a certain spatial direction (image pixel), defined as j, creates event i, a series of energy depositions, in the detector array. The detector-array system introduces uncertainty in recorded interaction position and deposited energy due to noise. Then each measurement is binned into a small volume ΔV_i around measurement i due to the digitization from ADC and pixelation of the detector system. Therefore, the system response function can be achieved in three steps:

1) The probability density function for a perfect detector-array system can be derived as $f(\tilde{i}; j)$, where $\tilde{i}$ is the real event created by a detected photon from energy and direction j.

2) Assuming the measurement uncertainty from the noise follows a Gaussian distribution, $f(\hat{i}|\tilde{i})$ can be derived, where $\hat{i}$ is the response of the detector-array system due to the uncertainty from the real event $\tilde{i}$.

3) The probability is then integrated over the bin volume ΔV_i to achieve the system response function.

In other words, the system response function can be calculated by [55; 56]:

$$t_{ij} = \int_{\Delta V_i} \mathrm{d}\hat{i} \int f(\hat{i}|\tilde{i}) f(\tilde{i}; j) \, \mathrm{d}\tilde{i} \tag{5.6}$$

Figure 5.1 shows the typical scenario of a three-interaction event. If the distance between the source and the detector array is much larger than the size of the detector array, a single stationary detector-array system cannot estimate the true three-dimensional source position, only the direction of the incident photon. Therefore the sources can be assumed to be located on the surface of an image sphere with a radius R, where R is much greater than the dimension of the detector array. A photon with energy E_0 originating from j can be denoted as (E_0, r_0), where r_0 is the position of the incident photon on the image sphere. The photon travels distance d_1 (entering distance) in the detector material before the first Compton-scatter interaction at location r_1 with energy deposition E_1, which can be described as (E_1, r_1). The scattered photon travels distance d_2 in the detector material before the second Compton scatter (E_2, r_2). The scattered photon, after the second Compton scatter, travels distance d_3 in the detector material, then has the third interaction (E_3, r_3). For the partial energy deposition case, the escaping photon travels distance d_4 (escaping distance) in the detector material before leaving the detector. The measurement of $\hat{i}$ and $\tilde{i}$ can be described as $(\hat{E}_1, \hat{r}_1, \hat{E}_2, \hat{r}_2, \hat{E}_3, \hat{r}_3)$ and $(\tilde{E}_1, \tilde{r}_1, \tilde{E}_2, \tilde{r}_2, \tilde{E}_3, \tilde{r}_3)$, respectively. Similarly, a measured four-interaction event i can be described as $(E_1, r_1, E_2, r_2, E_3, r_3, E_4, r_4)$. In a four-interaction case, d_1 and d_5 describe the entering distance and the escaping distance, while d_2, d_3, and d_4 describe the photon travel distance in material between the first and the second interaction, the second and the third interaction, and the third and the fourth interaction, respectively.
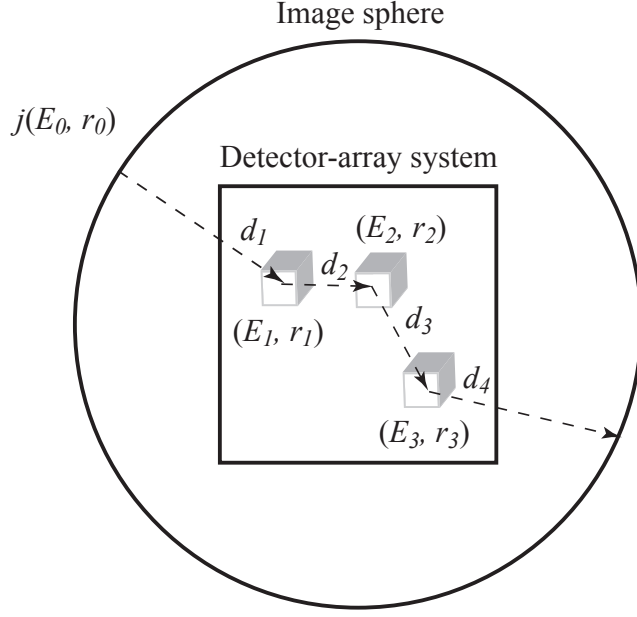
Figure 5.1: A three-interaction event $i(E_1, r_1, E_2, r_2, E_3, r_3)$ is created by a photon from energy and direction $j(E_0, r_0)$ in the image sphere.

5.2.1 Probability Calculation for Three-Interaction Events

Using the chain rule,

$$
\begin{aligned}
f(\tilde{i}|j) &= f(\tilde{E}_1, \tilde{r}_1, \tilde{E}_2, \tilde{r}_2, \tilde{E}_3, \tilde{r}_3, D_1^c, D_2^c, D_3; E_0, r_0) \\
&= f(\tilde{E}_3, D_3 | \tilde{E}_1, \tilde{r}_1, \tilde{E}_2, \tilde{r}_2, \tilde{r}_3, D_1^c, D_2^c; E_0, r_0) \\
&\quad \cdot f(\tilde{r}_3 | \tilde{E}_1, \tilde{r}_1, \tilde{E}_2, \tilde{r}_2, D_1^c, D_2^c; E_0, r_0) \\
&\quad \cdot f(\tilde{E}_2, D_2^c | \tilde{E}_1, \tilde{r}_1, \tilde{r}_2, D_1^c; E_0, r_0) \\
&\quad \cdot f(\tilde{E}_1, \tilde{r}_1, \tilde{r}_2, D_1^c; E_0, r_0)
\end{aligned}
\tag{5.7}
$$

where D_1^c represents that the first interaction is a Compton scatter, D_2^c represents that the second interaction is a Compton scatter, and D_3 represents that the third interaction is the last recorded interaction in this event.

The probability that the second interaction is a Compton event with energy de-

position of $\tilde{E}_2$ given that the interaction is at location $\tilde{r}_2$ is

$$f(\tilde{E}_2, D_2^c|\tilde{E}_1, \tilde{r}_1, \tilde{r}_2, D_1^c; E_0, r_0)$$
$$=f(\tilde{E}_2|\tilde{E}_1, \tilde{r}_1, \tilde{r}_2, D_1^c, D_2^c; E_0, r_0)f(D_2^c|\tilde{E}_1, \tilde{r}_1, \tilde{r}_2, D_1^c; E_0, r_0)$$

(5.8)

For computational simplicity, we neglect $f(D_2^c|\tilde{E}_1, \tilde{r}_1, \tilde{r}_2, D_1^c; E_0, r_0)$ for now. Future work is needed to study how to practically compute this term.

$$f(\tilde{E}_2, D_2^c|\tilde{E}_1, \tilde{r}_1, \tilde{r}_2, D_1^c; E_0, r_0)$$
$$\approx f(\tilde{E}_2|\tilde{E}_1, \tilde{r}_1, \tilde{r}_2, D_1^c, D_2^c; E_0, r_0)$$
$$=\frac{1}{\sigma_t(E_0 - \tilde{E}_1)} \left.\frac{d\sigma_c(E_0 - \tilde{E}_1)}{d\Omega}\right|_{\tilde{E}_2} \frac{d\Omega}{d\tilde{E}_2}$$
$$=\frac{N}{\mu_{E_0 - \tilde{E}_1}} \left.\frac{d\sigma_c(E_0 - \tilde{E}_1)}{d\Omega}\right|_{\tilde{E}_2} \frac{d\Omega}{d\tilde{E}_2}$$

(5.9)

in which N is the number of nuclei per unit volume, $\sigma_t(E)$ is the total cross section at energy E, and $\left.\frac{d\sigma_c(E)}{d\Omega}\right|_{E'}$ is the differential scattering cross section per solid angle defined by the Klein-Nishina formula for a photon with energy E depositing energy E' in the Compton scatter.

Define $\tilde{\lambda}_1 = \frac{\tilde{r}_1 - r_0}{|\tilde{r}_1 - r_0|}$, $\tilde{\lambda}_2 = \frac{\tilde{r}_2 - \tilde{r}_1}{|\tilde{r}_2 - \tilde{r}_1|}$ and $\tilde{\lambda}_3 = \frac{\tilde{r}_3 - \tilde{r}_2}{|\tilde{r}_3 - \tilde{r}_2|}$, which are the directions of the incident and the scattered photon. θ_{r_1} is the angle between $\tilde{\lambda}_1$ and $\tilde{\lambda}_2$. θ_{e_1} is the angle determined by the Compton scattering formula:

$$\cos\theta_{e_1} = 1 + \frac{m_e c^2}{E_0} - \frac{m_e c^2}{E_0 - \tilde{E}_1}$$

(5.10)

θ_{r_2} is the angle between $\tilde{\lambda}_2$ and $\tilde{\lambda}_3$, and θ_{e_2} is calculated from the Compton scattering

44

formula

$$\cos\theta_{e_2} = 1 + \frac{m_e c^2}{E_0 - \tilde{E}_1} - \frac{m_e c^2}{E_0 - \tilde{E}_1 - \tilde{E}_2} \tag{5.11}$$

The solid angle of a cone with an apex angle of $2\theta_{e_2}$ is

$$\Omega = 2\pi(1 - \cos\theta_{e_2}) = 2\pi(-\frac{m_e c^2}{E_0 - \tilde{E}_1} + \frac{m_e c^2}{E_0 - \tilde{E}_1 - \tilde{E}_2}) \tag{5.12}$$

where $m_e c^2$ is the rest energy of an electron. So,

$$\frac{d\Omega}{d\tilde{E}_2} = \frac{2\pi m_e c^2}{(E_0 - \tilde{E}_1 - \tilde{E}_2)^2} \tag{5.13}$$

The probability that the third interaction is at location $\tilde{r}_3$ given the first and second Compton scattering locations and energy depositions is

$$f(\tilde{r}_3|\tilde{E}_1, \tilde{r}_1, \tilde{E}_2, \tilde{r}_2, D_1^c, D_2^c; E_0, r_0)$$
$$= f(\tilde{\lambda}_3, d_3|\tilde{E}_1, \tilde{r}_1, \tilde{E}_2, \tilde{r}_2, D_1^c, D_2^c; E_0, r_0)$$
$$= f(\tilde{\lambda}_3|d_3, \tilde{E}_1, \tilde{r}_1, \tilde{E}_2, \tilde{r}_2, D_1^c, D_2^c; E_0, r_0)f(d_3|\tilde{E}_1, \tilde{r}_1, \tilde{E}_2, \tilde{r}_2, D_1^c, D_2^c; E_0, r_0)$$
$$= \frac{\delta(\theta_{r_2} - \theta_{e_2})}{2\pi d_3^2 \sin\theta_{e_2}} \cdot \mu_{E_0 - \tilde{E}_1 - \tilde{E}_2} e^{-\mu_{E_0 - \tilde{E}_1 - \tilde{E}_2} d_3} \tag{5.14}$$

where μ_E is the linear attenuation coefficient at energy E for the material, and $\tilde{r}_3$ is a function of $\tilde{\lambda}_3$ and d_3.

$$f(\tilde{E}_1, \tilde{r}_1, \tilde{r}_2, D_1^c; E_0, r_0) = f(\tilde{E}_1, \tilde{r}_1, \tilde{r}_2|D_1^c; E_0, r_0)f(D_1^c; E_0, r_0) \tag{5.15}$$

We neglect term $f(D_1^c; E_0, r_0)$ for calculation efficiency. According to Xu [55], given that the initial photon is from location r_0 and has an energy of E_0, the probability that the first interaction deposits energy $\tilde{E}_1$ at $\tilde{r}_1$ and the second interaction happens

45

at $\tilde{r}_2$ is:

$$f(\tilde{E}_1, \tilde{r}_1, \tilde{r}_2, D_1^c; E_0, r_0) \approx f(\tilde{E}_1, \tilde{r}_1, \tilde{r}_2 | D_1^c; E_0, r_0)$$

$$\approx \frac{1}{4\pi R^2} e^{-\mu_{E_0} d_1} N \frac{d\sigma_c(E_0)}{d\Omega}\bigg|_{\tilde{E}_1} \frac{2\pi m_e c^2}{(E_0 - \tilde{E}_1)^2} \mu_{E_0 - \tilde{E}_1} e^{-\mu_{E_0 - \tilde{E}_1} d_2} \frac{\delta(\theta_{r_1} - \theta_{e_1})}{2\pi d_2^2 \sin\theta_{e_1}} \qquad (5.16)$$

where $\frac{1}{4\pi R^2}$ is the geometric attenuation to reach $\tilde{r}_1$.

Combining equations (5.9), (5.13), (5.14), and (5.16), we have the probability that the initial photon (E_0, r_0) has the first Compton interaction $(\tilde{E}_1, \tilde{r}_1)$, the second Compton interaction $(\tilde{E}_2, \tilde{r}_2)$ and the third interaction at location $\tilde{r}_3$ in the detector-array system.

$$f(\tilde{E}_1, \tilde{r}_1, \tilde{E}_2, \tilde{r}_2, \tilde{r}_3, D_1^c, D_2^c; E_0, r_0)$$

$$= f(\tilde{r}_3 | \tilde{E}_1, \tilde{r}_1, \tilde{E}_2, \tilde{r}_2, D_1^c, D_2^c; E_0, r_0) f(\tilde{E}_2, D_2^c | \tilde{E}_1, \tilde{r}_1, \tilde{r}_2, D_1^c; E_0, r_0)$$

$$\cdot f(\tilde{E}_1, \tilde{r}_1, \tilde{r}_2, D_1^c; E_0, r_0)$$

$$= \frac{1}{4\pi R^2} N^2 e^{-\mu_{E_0} d_1 - \mu_{E_0 - \tilde{E}_1} d_2 - \mu_{E_0 - \tilde{E}_1 - \tilde{E}_2} d_3} \frac{d\sigma_c(E_0)}{d\Omega}\bigg|_{\tilde{E}_1} \frac{d\sigma_c(E_0 - \tilde{E}_1)}{d\Omega}\bigg|_{\tilde{E}_2}$$

$$\cdot \frac{2\pi m_e c^2}{(E_0 - \tilde{E}_1)^2} \frac{2\pi m_e c^2}{(E_0 - \tilde{E}_1 - \tilde{E}_2)^2} \frac{\delta(\theta_{r_1} - \theta_{e_1})\delta(\theta_{r_2} - \theta_{e_2})}{2\pi d_2^2 \sin\theta_{e_1} 2\pi d_3^2 \sin\theta_{e_2}} \mu_{E_0 - \tilde{E}_1 - \tilde{E}_2} \qquad (5.17)$$

For a three-interaction event, the third interaction can be a photoelectric interaction or a Compton interaction. Let $D_3 = D_3^p \cup D_3^c$, where D_3^p represents that the third interaction is a photoelectric interaction, and D_3^c represents that the scattered photon after the second interaction Compton scatters the third time then escapes from the detector array. Note $D_3^c \cap D_3^p = \emptyset$.

If the third interaction is a photoelectric interaction, $E_0 \approx E_1 + E_2 + E_3$. The probability for the photoelectric interaction depositing energy $\tilde{E}_3$ given that the photon

interacts at location $\tilde{r}_3$ is

$$f(\tilde{E}_3, D_3^p | \tilde{E}_1, \tilde{r}_1, \tilde{E}_2, \tilde{r}_2, \tilde{r}_3, D_1^c, D_2^c; E_0, r_0)$$

$$= f(\tilde{E}_3 | \tilde{E}_1, \tilde{r}_1, \tilde{E}_2, \tilde{r}_2, \tilde{r}_3, D_1^c, D_2^c, D_3^p; E_0, r_0) f(D_3^p | \tilde{E}_1, \tilde{r}_1, \tilde{E}_2, \tilde{r}_2, \tilde{r}_3, D_1^c, D_2^c; E_0, r_0)$$

$$\approx f(\tilde{E}_3 | \tilde{E}_1, \tilde{r}_1, \tilde{E}_2, \tilde{r}_2, \tilde{r}_3, D_1^c, D_2^c, D_3^p; E_0, r_0)$$

$$= \frac{\sigma_p(\tilde{E}_3) \delta(E_0 - \tilde{E}_1 - \tilde{E}_2 - \tilde{E}_3)}{\sigma_t(\tilde{E}_3)}$$

$$= \frac{N \sigma_p(\tilde{E}_3) \delta(E_0 - \tilde{E}_1 - \tilde{E}_2 - \tilde{E}_3)}{\mu_{E_0 - \tilde{E}_1 - \tilde{E}_2}} \tag{5.18}$$

where $\sigma_p(\tilde{E}_3)$ is the photoelectric cross section at energy $\tilde{E}_3$. For computational efficiency, we neglect $f(D_3^p | \tilde{E}_1, \tilde{r}_1, \tilde{E}_2, \tilde{r}_2, \tilde{r}_3, D_1^c, D_2^c; E_0, r_0)$. If the third interaction is a Compton scatter, instead, $E_0 > E_1 + E_2 + E_3$. The probability that the scattered photon after the second interaction deposits part of its energy $\tilde{E}_3$ in the third Compton interaction and the scatter photon travels distance d_4 in the detector material before escaping from the detector-array system is

$$f(\tilde{E}_3, D_3^c | \tilde{E}_1, \tilde{r}_1, \tilde{E}_2, \tilde{r}_2, \tilde{r}_3, D_1^c, D_2^c; E_0, r_0)$$

$$= f(\tilde{E}_3 | \tilde{E}_1, \tilde{r}_1, \tilde{E}_2, \tilde{r}_2, \tilde{r}_3, D_1^c, D_2^c, D_3^c; E_0, r_0) f(D_3^c | \tilde{E}_1, \tilde{r}_1, \tilde{E}_2, \tilde{r}_2, \tilde{r}_3, D_1^c, D_2^c; E_0, r_0)$$

$$\approx f(\tilde{E}_3 | \tilde{E}_1, \tilde{r}_1, \tilde{E}_2, \tilde{r}_2, \tilde{r}_3, D_1^c, D_2^c, D_3^c; E_0, r_0)$$

$$= \frac{N}{\mu_{E_0 - \tilde{E}_1 - \tilde{E}_2}} \left. \frac{\mathrm{d}\sigma_c(E_0 - \tilde{E}_1 - \tilde{E}_2)}{\mathrm{d}\Omega} \right|_{\tilde{E}_3}$$

$$\cdot \frac{2\pi m_e c^2}{(E_0 - \tilde{E}_1 - \tilde{E}_2 - \tilde{E}_3)^2} e^{-\mu_{E_0 - \tilde{E}_1 - \tilde{E}_2 - \tilde{E}_3} d_4} \tag{5.19}$$

For computational efficiency, we neglect $f(D_3^c | \tilde{E}_1, \tilde{r}_1, \tilde{E}_2, \tilde{r}_2, \tilde{r}_3, D_1^c, D_2^c; E_0, r_0)$. By combining equation (5.7), (5.17), (5.18) and (5.19) above, two equations are possible.

1. Three-interaction full-energy-deposition events

$$
\begin{aligned}
f_f(\tilde{i}|j) =& f(\tilde{E}_1, \tilde{r}_1, \tilde{E}_2, \tilde{r}_2, \tilde{E}_3, \tilde{r}_3, D_1^c, D_2^c, D_3^p; E_0, r_0) \\
=& f(\tilde{E}_3, D_3^p | \tilde{E}_1, \tilde{r}_1, \tilde{E}_2, \tilde{r}_2, \tilde{r}_3, D_1^c, D_2^c; E_0, r_0) f(\tilde{E}_1, \tilde{r}_1, \tilde{E}_2, \tilde{r}_2, \tilde{r}_3, D_1^c, D_2^c; E_0, r_0) \\
=& \frac{N \sigma_p(\tilde{E}_3) \delta(E_0 - \tilde{E}_1 - \tilde{E}_2 - \tilde{E}_3)}{\mu_{E_0 - \tilde{E}_1 - \tilde{E}_2}} f(\tilde{E}_1, \tilde{r}_1, \tilde{E}_2, \tilde{r}_2, \tilde{r}_3, D_1^c, D_2^c; E_0, r_0)
\end{aligned}
$$

$$(5.20)$$

2. Three-interaction partial-energy-deposition events

$$
\begin{aligned}
f_p(\tilde{i}|j) =& f(\tilde{E}_1, \tilde{r}_1, \tilde{E}_2, \tilde{r}_2, \tilde{E}_3, \tilde{r}_3, D_1^c, D_2^c, D_3^c; E_0, r_0) \\
=& f(\tilde{E}_3, D_3^c | \tilde{E}_1, \tilde{r}_1, \tilde{E}_2, \tilde{r}_2, \tilde{r}_3, D_1^c, D_2^c; E_0, r_0) f(\tilde{E}_1, \tilde{r}_1, \tilde{E}_2, \tilde{r}_2, \tilde{r}_3, D_1^c, D_2^c; E_0, r_0) \\
=& \frac{N}{\mu_{E_0 - \tilde{E}_1 - \tilde{E}_2}} \left. \frac{d\sigma_c(E_0 - \tilde{E}_1 - \tilde{E}_2)}{d\Omega} \right|_{\tilde{E}_3} \frac{2\pi m_e c^2}{(E_0 - \tilde{E}_1 - \tilde{E}_2 - \tilde{E}_3)^2} e^{-\mu_{E_0 - \tilde{E}_1 - \tilde{E}_2 - \tilde{E}_3} d_4} \\
& \cdot f(\tilde{E}_1, \tilde{r}_1, \tilde{E}_2, \tilde{r}_2, \tilde{r}_3, D_1^c, D_2^c; E_0, r_0)
\end{aligned}
$$

$$(5.21)$$

In equation (5.20) and (5.21), $f(\tilde{E}_1, \tilde{r}_1, \tilde{E}_2, \tilde{r}_2, \tilde{r}_3, D_1^c, D_2^c; E_0, r_0)$ is defined in equation (5.17).

5.2.2 Considering the Measurement Uncertainties

The measurement uncertainties will be considered in the following integration.

$$
\begin{aligned}
f(\hat{i}; j) =& \int f(\hat{i}|\tilde{i}) f(\tilde{i}; j) \, d\tilde{i} \\
=& \int f(\hat{E}_1, \hat{r}_1, \hat{E}_2, \hat{r}_2, \hat{E}_3, \hat{r}_3 | \tilde{E}_1, \tilde{r}_1, \tilde{E}_2, \tilde{r}_2, \tilde{E}_3, \tilde{r}_3) \\
& \cdot f(\tilde{E}_1, \tilde{r}_1, \tilde{E}_2, \tilde{r}_2, \tilde{E}_3, \tilde{r}_3, D_1^c, D_2^c, D_3; E_0, r_0) \, dV
\end{aligned}
$$

$$(5.22)$$

where dV is defined by differential elements in $\tilde{E}_1, \tilde{r}_1, \tilde{E}_2, \tilde{r}_2, \tilde{E}_3$ and $\tilde{r}_3$.

All measurements of the energy and the position are assumed to follow Gaussian

distributions. Given the true interaction energy deposition and position $\tilde{E}, \tilde{x}, \tilde{y}, \tilde{z}$ from an ideal detector-array system, the distribution of the probability of observing interaction $\hat{E}, \hat{x}, \hat{y}, \hat{z}$ is

$$f_E(\hat{E}|\tilde{E}) = \frac{1}{\sqrt{2\pi\sigma_E^2}} e^{-\frac{(\hat{E}-\tilde{E})^2}{2\sigma_E^2}} \tag{5.23}$$

$$f_E(\hat{x}|\tilde{x}) = \frac{1}{\sqrt{2\pi\sigma_x^2}} e^{-\frac{(\hat{x}-\tilde{x})^2}{2\sigma_x^2}} \tag{5.24}$$

$$f_E(\hat{y}|\tilde{y}) = \frac{1}{\sqrt{2\pi\sigma_y^2}} e^{-\frac{(\hat{y}-\tilde{y})^2}{2\sigma_y^2}} \tag{5.25}$$

$$f_E(\hat{z}|\tilde{z}) = \frac{1}{\sqrt{2\pi\sigma_z^2}} e^{-\frac{(\hat{z}-\tilde{z})^2}{2\sigma_z^2}} \tag{5.26}$$

So, $f(\hat{E}_1, \hat{r}_1, \hat{E}_2, \hat{r}_2, \hat{E}_3, \hat{r}_3 | \tilde{E}_1, \tilde{r}_1, \tilde{E}_2, \tilde{r}_2, \tilde{E}_3, \tilde{r}_3)$ is a joint Gaussian distribution, and

$$\int f(\hat{E}_1, \hat{r}_1, \hat{E}_2, \hat{r}_2, \hat{E}_3, \hat{r}_3 | \tilde{E}_1, \tilde{r}_1, \tilde{E}_2, \tilde{r}_2, \tilde{E}_3, \tilde{r}_3) \, \mathrm{d}V = 1 \tag{5.27}$$

In our system, the position uncertainty from pixelation contributes much more angular error than energy measurement uncertainty, so we assume θ_e is constant in this calculation. If the measurement uncertainty in energy and position is fine enough, $f(\tilde{E}_1, \tilde{r}_1, \tilde{E}_2, \tilde{r}_2, \tilde{E}_3, \tilde{r}_3, D_1^c, D_2^c, D_3; E_0, r_0)$ varies little within the scale of the uncertainty. It can be considered as a constant, and $(\tilde{E}_1, \tilde{r}_1, \tilde{E}_2, \tilde{r}_2, \tilde{E}_3, \tilde{r}_3)$ can be replaced by $(\hat{E}_1, \hat{r}_1, \hat{E}_2, \hat{r}_2, \hat{E}_3, \hat{r}_3)$. This approximation is valid for the partial-energy-deposition case. However, in the full-energy deposition case, the delta function $\delta(E_0 - \tilde{E}_1 - \tilde{E}_2 - \tilde{E}_3)$ in equation (5.20) will not vary slowly and has to be calculated separately.

1. Three-interaction full-energy-deposition events

$$f_f(\hat{i}; j) \approx f(\hat{E}_1, \hat{r}_1, \hat{E}_2, \hat{r}_2, \hat{r}_3, D_1^c, D_2^c, D_3^p; E_0, r_0) \frac{N \sigma_p(\hat{E}_3)}{\mu_{E_0 - \hat{E}_1 - \hat{E}_2}}$$

$$\cdot \iiint \delta(E_0 - \tilde{E}_1 - \tilde{E}_2 - \tilde{E}_3) \frac{1}{\sqrt{2\pi}^3 \sigma_{E_1} \sigma_{E_2} \sigma_{E_3}}$$

$$\cdot e^{-\frac{(\hat{E}_1 - \tilde{E}_1)^2}{2\sigma_{E_1}^2} - \frac{(\hat{E}_2 - \tilde{E}_2)^2}{2\sigma_{E_2}^2} - \frac{(\hat{E}_3 - \tilde{E}_3)^2}{2\sigma_{E_3}^2}} \, d\tilde{E}_1 \, d\tilde{E}_2 \, d\tilde{E}_3$$

$$= f(\hat{E}_1, \hat{r}_1, \hat{E}_2, \hat{r}_2, \hat{r}_3; E_0, r_0) \frac{N \sigma_p(\hat{E}_3)}{\mu_{E_0 - \hat{E}_1 - \hat{E}_2}}$$

$$\cdot \frac{1}{\sqrt{2\pi(\sigma_{E_1}^2 + \sigma_{E_2}^2 + \sigma_{E_3}^2)}} e^{-\frac{(E_0 - \hat{E}_1 - \hat{E}_2 - \hat{E}_3)^2}{2(\sigma_{E_1}^2 + \sigma_{E_2}^2 + \sigma_{E_3}^2)}} \quad (5.28)$$

2. Three-interaction partial-energy-deposition events

$$f_p(\hat{i}; j) \approx f(\hat{E}_1, \hat{r}_1, \hat{E}_2, \hat{r}_2, \hat{r}_3, D_1^c, D_2^c, D_3^c; E_0, r_0) \frac{N}{\mu_{E_0 - \hat{E}_1 - \hat{E}_2}}$$

$$\cdot \left. \frac{d\sigma_c(E_0 - \hat{E}_1 - \hat{E}_2)}{d\Omega} \right|_{\hat{E}_3} \frac{2\pi m_e c^2}{(E_0 - \hat{E}_1 - \hat{E}_2 - \hat{E}_3)^2}$$

$$\cdot e^{-\mu_{E_0 - \hat{E}_1 - \hat{E}_2 - \hat{E}_3} d_4} \quad (5.29)$$

5.2.3 Considering the Bin Volume

The probability density function needs to be integrated over the bin volume due to the energy binning and voxelation of the detector volume.

$$t_{ij} = \int_{\Delta V_i} f(\hat{i}; j) \, d\hat{i}$$

$$= \int_{\Delta V_i} f(\hat{E}_1, \hat{r}_1, \hat{E}_2, \hat{r}_2, \hat{E}_3, \hat{r}_3, D_1^c, D_2^c, D_3; E_0, r_0) \, d\hat{i} \quad (5.30)$$

where $d\hat{i} = d\hat{E}_1 \, d\hat{r}_1 \, d\hat{E}_2 \, d\hat{r}_2 \, d\hat{E}_3 \, d\hat{r}_3$. ΔV_i is the bin volume around measurement i.

If the binning volume is small enough that the non-delta function terms change

slightly in the bin volume, they can be approximated to be constants and moved out of the integral, and $(\hat{E}_1, \hat{r}_1, \hat{E}_2, \hat{r}_2, \hat{E}_3, \hat{r}_3)$ can be replaced by $(E_1, r_1, E_2, r_2, E_3, r_3)$, the binned and discretized event coordinates.

1. Three-interaction full-energy-deposition events

$$
\begin{aligned}
t_{ij} \approx {} & \frac{N^3}{4\pi R^2} \frac{1}{2\pi d_2^2 \sin\theta_{e_1} \cdot 2\pi d_3^2 \sin\theta_{e_2}} \\
& \cdot e^{-\mu_{E_0} d_1} \left.\frac{\mathrm{d}\sigma_c(E_0)}{\mathrm{d}\Omega}\right|_{E_1} \frac{2\pi m_e c^2}{(E_0 - E_1)^2} \\
& \cdot e^{-\mu_{E_0 - E_1} d_2} \left.\frac{\mathrm{d}\sigma_c(E_0 - E_1)}{\mathrm{d}\Omega}\right|_{E_2} \frac{2\pi m_e c^2}{(E_0 - E_1 - E_2)^2} \\
& \cdot e^{-\mu_{E_0 - E_1 - E_2} d_3} \frac{\sigma_p(E_3)}{\sqrt{2\pi(\sigma_{E_1}^2 + \sigma_{E_2}^2 + \sigma_{E_3}^2)}} \\
& \cdot e^{-\frac{(E_0 - E_1 - E_2 - E_3)^2}{2(\sigma_{E_1}^2 + \sigma_{E_2}^2 + \sigma_{E_3}^2)}} \int_{\Delta V_i} \delta(\theta_{r_1} - \theta_{e_1})\delta(\theta_{r_2} - \theta_{e_2}) \, \mathrm{d}\hat{i} \qquad (5.31)
\end{aligned}
$$

2. Three-interaction partial-energy-deposition events

$$
\begin{aligned}
t_{ij} \approx {} & \frac{N^3}{4\pi R^2} \frac{1}{2\pi d_2^2 \sin\theta_{e_1} \cdot 2\pi d_3^2 \sin\theta_{e_2}} \\
& \cdot e^{-\mu_{E_0} d_1} \left.\frac{\mathrm{d}\sigma_c(E_0)}{\mathrm{d}\Omega}\right|_{E_1} \frac{2\pi m_e c^2}{(E_0 - E_1)^2} \\
& \cdot e^{-\mu_{E_0 - E_1} d_2} \left.\frac{\mathrm{d}\sigma_c(E_0 - E_1)}{\mathrm{d}\Omega}\right|_{E_2} \frac{2\pi m_e c^2}{(E_0 - E_1 - E_2)^2} \\
& \cdot e^{-\mu_{E_0 - E_1 - E_2} d_3} \left.\frac{\mathrm{d}\sigma_c(E_0 - E_1 - E_2)}{\mathrm{d}\Omega}\right|_{E_3} \frac{2\pi m_e c^2}{(E_0 - E_1 - E_2 - E_3)^2} \\
& \cdot e^{-\mu_{E_0 - E_1 - E_2 - E_3} d_4} \cdot \int_{\Delta V_i} \delta(\theta_{r_1} - \theta_{e_1})\delta(\theta_{r_2} - \theta_{e_2}) \, \mathrm{d}\hat{i} \qquad (5.32)
\end{aligned}
$$

Both cases have the term $\int_{\Delta V_i} \delta(\theta_{r_1} - \theta_{e_1})\delta(\theta_{r_2} - \theta_{e_2}) \, \mathrm{d}\hat{i}$. In our detector-array system, the anode of each detector module is divided into 11×11 pixels with pixel
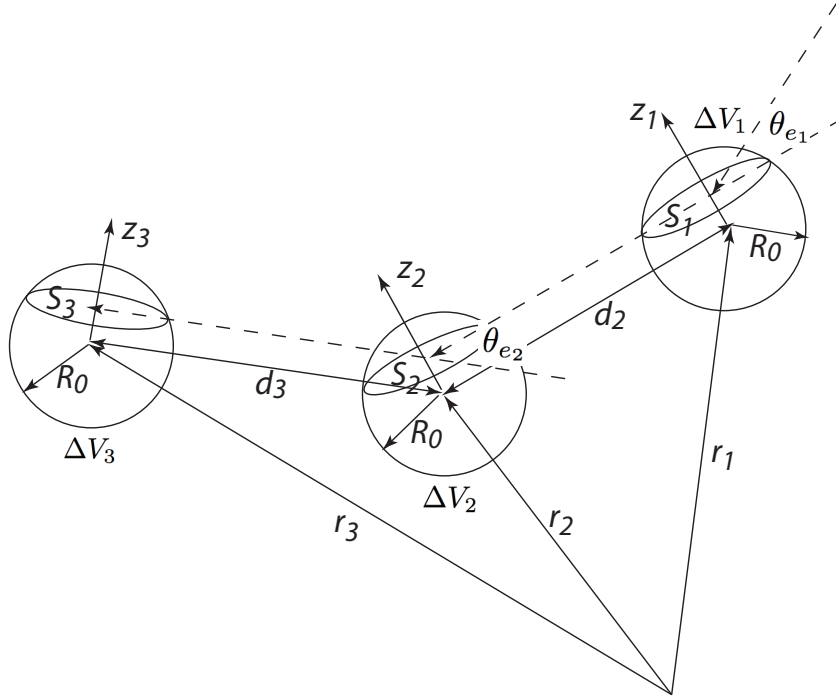
Figure 5.2: The binning volumes in the measurement space are approximated by three spheres in calculating the system response function.
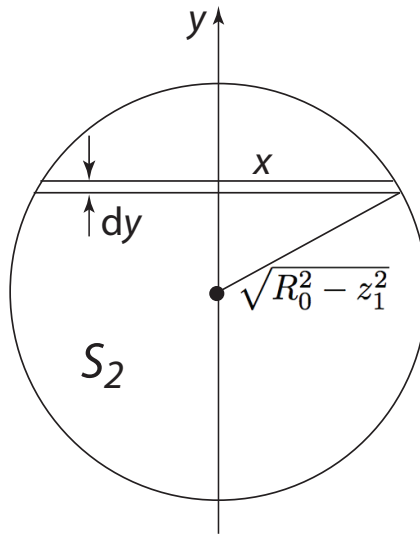
Figure 5.3: An illustration of the surface S_2 within ΔV_2 that satisfies $\theta_{e_1} = \theta_{r_1}$ for a point in ΔV_1. y crosses the origin of S_2 and is parallel with d_2. x is a line within S_2 that is perpendicular to both d_2 and y.

pitch of 1.72 mm. The x-y position of the interaction is determined by the anode pixel that collects the electrons. The interaction depth is found by the electron drift time and the cathode-to-anode signal ratio. The depth uncertainty due to digitization is about 0.5 mm. Therefore the bin volume in our system is a rectangular parallelepiped. In order to simplify the calculation, the bin volume for each event is approximated as a sphere with the same volume with a radius of R_0, as shown in figure 5.2. S_1 is a surface within ΔV_1, parallel to d_2, and containing the first interaction location. S_2 is a curved surface inside of ΔV_2 that satisfies $\theta_{e_1} = \theta_{r_1}$. S_3 is a curved surface within ΔV_3 that satisfies $\theta_{e_2} = \theta_{r_2}$. When $d_3 \gg R_0$, S_3 can be approximated by a plane and $dz_3 = d_3 \cdot d\theta_{r_2}$. Similarly, S_2 can be approximated by a plane and $dz_2 = d_2 \cdot d\theta_{r_1}$, when $d_2 \gg R_0$. z_1, z_2 and z_3 are perpendicular to S_1, S_2 and S_3, respectively. r_0 is on the back-projection cone defined by E_0, E_1, r_1 and r_2. The directions not on the back-projection cone will be approximated by a Gaussian function with its standard deviation equal to the angular uncertainty. So,

$$
\int_{\Delta V_i} \delta(\theta_{r_1} - \theta_{e_1})\delta(\theta_{r_2} - \theta_{e_2})\, d\hat{i}
$$

$$
= \Delta E_1 \Delta E_2 \Delta E_3 \int_{\Delta V_1} d\hat{r}_1 \int_{\Delta V_2} d\hat{r}_2 \delta(\theta_{r_1} - \theta_{e_1}) \int_{\Delta V_3} d\hat{r}_3 \delta(\theta_{r_2} - \theta_{e_2})
$$

$$
= \Delta E_1 \Delta E_2 \Delta E_3 \int_{\Delta V_1} d\hat{r}_1 \int_{\Delta V_2} d\hat{r}_2 \delta(\theta_{r_1} - \theta_{e_1}) \int_{-R_0}^{R_0} dz_3 \int_{S_3} d\hat{r}_3 \delta(\theta_{r_2} - \theta_{e_2})
$$

$$
= \Delta E_1 \Delta E_2 \Delta E_3 d_3 \int_{\Delta V_1} d\hat{r}_1 \int_{\Delta V_2} d\hat{r}_2 \delta(\theta_{r_1} - \theta_{e_1}) S_3
$$

$$
= \Delta E_1 \Delta E_2 \Delta E_3 d_3 \int_{\Delta V_1} d\hat{r}_1 \int_{-R_0}^{R_0} dz_2 \int_{S_2} d\hat{r}_2 \delta(\theta_{r_1} - \theta_{e_1}) S_3
$$

$$
= \Delta E_1 \Delta E_2 \Delta E_3 d_2 d_3 \int_{\Delta V_1} S_2 S_3 \, d\hat{r}_1 \tag{5.33}
$$

For each z_1 (S_1 moves along z_1), there is a different surface S_2 that satisfies $\theta_{e_1} = \theta_{r_1}$.

For each line x with a width $\mathrm{d}y$ in S_2, shown in figure 5.3, there will be a different S_3 which satisfies $\theta_{e_2} = \theta_{r_2}$. From geometry, for a specific z_1 and y, we can calculate that the area of S_3 is $\pi(R_0^2 - (z_1 \cos\theta_{e_2} + y \sin\theta_{e_2})^2)$ and $x = 2\sqrt{R_0^2 - z_1^2 - y^2}$. Therefore,

$$
\int\limits_{\Delta V_i} \delta(\theta_{r_1} - \theta_{e_1})\delta(\theta_{r_2} - \theta_{e_2})\,\mathrm{d}\hat{i}
$$

$$
= \Delta E_1 \Delta E_2 \Delta E_3 d_2 d_3 \int\limits_{-R_0}^{R_0} \mathrm{d}z_1 \pi(R_0^2 - z_1^2) \int\limits_{-\sqrt{R_0^2 - z_1^2}}^{\sqrt{R_0^2 - z_1^2}} \mathrm{d}y\, 2\sqrt{R_0^2 - z_1^2 - y^2}
$$

$$
\cdot\pi(R^2 - (z_1 \cos\theta_{e_2} + y \sin\theta_{e_2})^2)
$$

$$
= \Delta E_1 \Delta E_2 \Delta E_3 d_2 d_3 \pi^3 R_0^7 \frac{92 + 4\cos(2\theta_{e_2})}{105} \tag{5.34}
$$

5.2.4 System Response Function for Three-Interaction Events

Combining (5.31), (5.32) with (5.34), the two cases are

1. Three-interaction full-energy-deposition events

$$
t_{ij} = \frac{92 + 4\cos(2\theta_{e_2})}{105} \frac{\Delta E_1 \Delta E_2 \Delta E_3 N^3 R_0^7}{16 R^2 \cdot d_2 \sin\theta_{e_1} \cdot d_3 \sin\theta_{e_2}}
$$

$$
\cdot e^{-\mu_{E_0} d_1} \left.\frac{\mathrm{d}\sigma_c(E_0)}{\mathrm{d}\Omega}\right|_{E_1} \frac{2\pi m_e c^2}{(E_0 - E_1)^2}
$$

$$
\cdot e^{-\mu_{E_0 - E_1} d_2} \left.\frac{\mathrm{d}\sigma_c(E_0 - E_1)}{\mathrm{d}\Omega}\right|_{E_2} \frac{2\pi m_e c^2}{(E_0 - E_1 - E_2)^2}
$$

$$
\cdot e^{-\mu_{E_0 - E_1 - E_2} d_3} \frac{\sigma_p(E_3)}{\sqrt{2\pi(\sigma_{E_1}^2 + \sigma_{E_2}^2 + \sigma_{E_3}^2)}} e^{-\frac{(E_0 - E_1 - E_2 - E_3)^2}{2(\sigma_{E_1}^2 + \sigma_{E_2}^2 + \sigma_{E_3}^2)}} \tag{5.35}
$$

2. Three-interaction partial-energy-deposition events

$$t_{ij} = \frac{92 + 4\cos(2\theta_{e_2})}{105} \frac{\Delta E_1 \Delta E_2 \Delta E_3 N^3 R_0^7}{16R^2 \cdot d_2 \sin\theta_{e_1} \cdot d_3 \sin\theta_{e_2}}$$

$$\cdot e^{-\mu_{E_0} d_1} \left. \frac{\mathrm{d}\sigma_c(E_0)}{\mathrm{d}\Omega}\right|_{E_1} \frac{2\pi m_e c^2}{(E_0 - E_1)^2}$$

$$\cdot e^{-\mu_{E_0 - E_1} d_2} \left. \frac{\mathrm{d}\sigma_c(E_0 - E_1)}{\mathrm{d}\Omega}\right|_{E_2} \frac{2\pi m_e c^2}{(E_0 - E_1 - E_2)^2}$$

$$\cdot e^{-\mu_{E_0 - E_1 - E_2} d_3} \left. \frac{\mathrm{d}\sigma_c(E_0 - E_1 - E_2)}{\mathrm{d}\Omega}\right|_{E_3} \frac{2\pi m_e c^2}{(E_0 - E_1 - E_2 - E_3)^2}$$

$$\cdot e^{-\mu_{E_0 - E_1 - E_2 - E_3} d_4} \tag{5.36}$$

The definitions of the variables can be found in Table 5.1.

5.2.5 Simplified System Response Function of Three-Interaction Events for Combining with Other Events

The iterative list-mode MLEM algorithm is performed using equation (5.5)

$$f_j^{n+1} = \frac{f_j^n}{s_j} \sum_{i=1}^{I} \frac{t_{ij}}{\sum_k t_{ik} f_k^n} \tag{5.37}$$

where f_j^n is the estimated intensity in the direction and energy j at the nth iteration. The sensitivity s_j is the detection probability of a gamma ray emitted from j. I is the total number of events used in the reconstruction. t_{ij} is the system response function for event i from a detected photon j. For a particular event, t_{ij} appears in both the numerator and the denominator of equation (5.37), so the constant terms for this event will cancel. For a certain event in a specific system, ΔE_1, ΔE_2, ΔE_3, N, R_0, R are constant so can be canceled. d_2, d_3, $\sin\theta_{e_1}$ and $\sin\theta_{e_2}$ cannot be canceled because they are not the same for different sequences of one event. $\frac{92 + 4\cos(2\theta_{e_2})}{105}$ introduces only very small variation in the reconstructed image and can be considered constant

Table 5.1: Definitions of Variables

Variables	Definitions
E_0	incident photon energy
E_1, E_2, E_3	measured energy depositions
d_1	photon entering distance through detector material
d_2, d_3	photon in-material travel distance between the first and the second, the second and the third interaction
d_4	escaping distance though detector material in partial-energy deposition case
μ_E	linear attenuation coefficient at energy E for the detector material
$\sigma_p(E)$, $\sigma_c(E)$	photoelectric and Compton-scatter cross sections at energy E
$\frac{\mathrm{d}\sigma_c(E)}{\mathrm{d}\Omega}\big|_{E'}$	Klein-Nishina differential scattering cross section for a photon with energy E depositing energy E' in a Compton scatter
θ_{e_1}, θ_{e_2}	the first and second scattering angles determined using deposited energies and the Compton-scatter formula for the interaction indicated in the subscript
σ_E	uncertainty in recorded energy
N	number of nuclei per unit volume
R_0	radius of the sphere with the same volume as the pixelation and the depth uncertainty volume
$m_e c^2$	rest mass energy of an electron

and ignored [57; 58].

The simplified system response functions that can be used for deconvolving a single image with all possible sequences of a particular three-interaction event and events with other numbers of interaction are:

1. Three-interaction full-energy-deposition events

$$t_{ij} = \left[e^{-\mu_{E_0} d_1} \frac{\mathrm{d}\sigma_c(E_0)}{\mathrm{d}\Omega}\bigg|_{E_1} \frac{1}{(E_0 - E_1)^2}\right]$$

$$\cdot \left[e^{-\mu_{E_0 - E_1} d_2} \frac{1}{d_2 \sin\theta_{e_1}} \frac{\mathrm{d}\sigma_c(E_0 - E_1)}{\mathrm{d}\Omega}\bigg|_{E_2} \frac{1}{(E_0 - E_1 - E_2)^2}\right]$$

$$\cdot \left[e^{-\mu_{E_0 - E_1 - E_2} d_3} \frac{1}{d_3 \sin\theta_{e_2}} \cdot \frac{\sigma_p(E_3)}{\sqrt{2\pi(\sigma_{E_1}^2 + \sigma_{E_2}^2 + \sigma_{E_3}^2)}} e^{-\frac{(E_0 - E_1 - E_2 - E_3)^2}{2(\sigma_{E_1}^2 + \sigma_{E_2}^2 + \sigma_{E_3}^2)}}\right] \quad (5.38)$$

2. Three-interaction partial-energy-deposition events

$$t_{ij} = \left[e^{-\mu_{E_0} d_1} \frac{\mathrm{d}\sigma_c(E_0)}{\mathrm{d}\Omega}\bigg|_{E_1} \frac{1}{(E_0 - E_1)^2}\right]$$

$$\cdot \left[e^{-\mu_{E_0 - E_1} d_2} \frac{1}{d_2 \sin\theta_{e_1}} \frac{\mathrm{d}\sigma_c(E_0 - E_1)}{\mathrm{d}\Omega}\bigg|_{E_2} \frac{1}{(E_0 - E_1 - E_2)^2}\right]$$

$$\cdot \left[e^{-\mu_{E_0 - E_1 - E_2} d_3} \frac{1}{d_3 \sin\theta_{e_2}} \frac{\mathrm{d}\sigma_c(E_0 - E_1 - E_2)}{\mathrm{d}\Omega}\bigg|_{E_3} \frac{2\pi m_e c^2}{(E_0 - E_1 - E_2 - E_3)^2}\right]$$

$$\cdot e^{-\mu_{E_0 - E_1 - E_2 - E_3} d_4} \quad (5.39)$$

The simplified equations (5.38) and (5.39) are written in a modular way following the interaction sequence. The first square bracket in both equations represents the process of a photon entering the detector-array system and interacting by Compton scattering. The second square bracket in both equations represents the process that the scattered photon penetrates the detector material towards the second interaction location and Compton scatters the second time. The third square bracket in the full-energy deposition case, equation (5.38), represents the process that the scattered photon penetrates the detector material towards the third interaction location and deposits all its energy. The third square bracket in the partial-energy deposition case, equation (5.39), represents the process that the scattered photon penetrates the detector material towards the third interaction location, Compton scatters the third

time, and the last line in equation (5.39) represents the probability that the scattered photon escapes from the detector array.

5.3 System Response Function for Events with Any Number of Interactions

The system response functions for events with any number of interactions can be extrapolated by changing and adding probability modules which represent the additional physics of penetrations and interactions to equations (5.38) and (5.39) .

1. n-interaction full-energy-deposition events

$$
\begin{aligned}
t_{ij} &= \frac{1}{d_2 \sin \theta_{e_1} \cdot d_3 \sin \theta_{e_2} \cdot \cdots \cdot d_n \sin \theta_{e_{n-1}}} \\
&\cdot e^{-\mu_{E_0} d_1} \left. \frac{\mathrm{d}\sigma_c(E_0)}{\mathrm{d}\Omega} \right|_{E_1} \frac{1}{(E_0 - E_1)^2} \\
&\cdot e^{-\mu_{E_0 - E_1} d_2} \left. \frac{\mathrm{d}\sigma_c(E_0 - E_1)}{\mathrm{d}\Omega} \right|_{E_2} \frac{1}{(E_0 - E_1 - E_2)^2} \\
&\cdots \\
&\cdot e^{-\mu_{E_0 - E_1 - \cdots - E_{n-2}} d_{n-1}} \left. \frac{\mathrm{d}\sigma_c(E_0 - E_1 - \cdots - E_{n-2})}{\mathrm{d}\Omega} \right|_{E_{n-1}} \frac{1}{(E_0 - E_1 - \cdots - E_{n-1})^2} \\
&\cdot e^{-\mu_{E_0 - E_1 - E_2 - \cdots - E_{n-1}} d_n} \frac{\sigma_p(E_n)}{\sqrt{2\pi(\sigma_{E_1}^2 + \sigma_{E_2}^2 + \sigma_{E_3}^2 + \cdots + \sigma_{E_n}^2)}} \\
&\cdot e^{-\frac{(E_0 - E_1 - E_2 - E_3 - \cdots - E_n)^2}{2(\sigma_{E_1}^2 + \sigma_{E_2}^2 + \sigma_{E_3}^2 + \cdots + \sigma_{E_n}^2)}}
\end{aligned} \tag{5.40}
$$

2. n-interaction partial-energy-deposition events

$$t_{ij} = \frac{1}{d_2 \sin\theta_{e_1} \cdot d_3 \sin\theta_{e_2} \cdot \cdots \cdot d_n \sin\theta_{e_{n-1}}}$$

$$\cdot e^{-\mu_{E_0} d_1} \frac{\mathrm{d}\sigma_c(E_0)}{\mathrm{d}\Omega}\bigg|_{E_1} \frac{1}{(E_0 - E_1)^2}$$

$$\cdot e^{-\mu_{E_0-E_1} d_2} \frac{\mathrm{d}\sigma_c(E_0 - E_1)}{\mathrm{d}\Omega}\bigg|_{E_2} \frac{1}{(E_0 - E_1 - E_2)^2}$$

$$\cdots$$

$$\cdot e^{-\mu_{E_0-E_1-\cdots-E_{n-2}} d_{n-1}} \frac{\mathrm{d}\sigma_c(E_0 - E_1 - \cdots - E_{n-2})}{\mathrm{d}\Omega}\bigg|_{E_{n-1}} \frac{1}{(E_0 - E_1 - \cdots - E_{n-1})^2}$$

$$\cdot e^{-\mu_{E_0-E_1-E_2-\cdots-E_{n-1}} d_n} \frac{\mathrm{d}\sigma_c(E_0 - E_1 - E_2 - \cdots - E_{n-1})}{\mathrm{d}\Omega}\bigg|_{E_n}$$

$$\cdot \frac{2\pi m_e c^2}{(E_0 - E_1 - E_2 - \cdots - E_n)^2}$$

$$\cdot e^{-\mu_{E_0-E_1-E_2-\cdots-E_n} d_{n+1}} \tag{5.41}$$

Particularly, for single-interaction events, the system response functions are:

1. Single-interaction full-energy-deposition events

$$t_{ij} = e^{-\mu_{E_0} d_1} \frac{\sigma_p(E_1)}{\sqrt{2\pi\sigma_{E_1}^2}} e^{-\frac{(E_0-E_1)^2}{2\sigma_{E_1}^2}} \tag{5.42}$$

2. Single-interaction partial-energy-deposition events

$$t_{ij} = e^{-\mu_{E_0} d_1} \frac{\sigma_c(E_0)}{\mathrm{d}\Omega}\bigg|_{E_1} \frac{2\pi m_e c^2}{(E_0 - E_1)^2} e^{-\mu_{E_0-E_1} d_2} \tag{5.43}$$

Equations (5.42) and (5.43) can also be derived without using the approximation of a spherical pixelation-binning volume.

In order to perform the maximum-likelihood deconvolution for single-interaction events (attenuation imaging), the attenuation distance d_1 and d_2 have to be calculated for every direction for every event. This calculation is very computationally intensive. Compared to multiple-interaction events, single-interaction events provide poorer angular resolution in the reconstructed image due to less concentrated directional information. The source can be located at any direction for a single-interaction event, but it can only be located on a small set of Compton cones for a multiple-interaction event. The image from single-interaction events solely depends on the penetration distance of the photon; hence, it is largely influenced by the geometry and nonuniform detector response.

5.4 Discussion

There are several factors that are not included in the system model and may affect the reconstructed image.

- 11×11 electrodes are attached to the anode surface of the detector. The peripheral pixels have slightly larger effective volume than inner pixels.

- In order to eliminate noise triggers, a software trigger threshold was set to 30 keV. Interactions with energies less than 30 keV are ignored. Due to the small scatter angle produced by small energy depositions, ignoring interactions with energy less than 30 keV has little impact on 2D directional image reconstruction.

- Multiple interactions can occur under the same pixel. Due to the limitation of the analog ASIC, multiple events will be reconstructed as a single interaction with the combined energy. For multiple-pixel events, the reconstructed depth from drift time is determined by the interaction that is closest to the collecting anode, so there is a systematic bias for the reconstructed depth towards the anode side.

- Studies have shown that the electron cloud may migrate to its neighbor pixels as it drifts toward the collecting anode pixel from its interaction location [38]. This pixel-jumping effect is more severe on the cathode side [35], and behaves differently in different crystals. This pixel-jumping effect changes the reconstructed axis of the Compton cone slightly. Compton image reconstruction is less sensitive to the pixel-jumping effect than some other imaging methods (such as coded aperture). More study is needed to map the pixel-jumping probability for each pixel experimentally for each detector, if this effect were to be included in the system model.

- Photons which interact close to the anode produce a smaller signal that is sometimes below the trigger threshold. The thickness of this dead layer depends on the photon energy and the software trigger threshold level. An experiment shows for 662 keV the thickness of the dead layer near the anode surface is around 1 mm [39]. This effect has a huge impact on the image reconstruction for single-interaction events. Future study is needed to include this effect in the sensitivity factor.

- By digitizing the cathode waveform, a new study [40] shows the electric field is a function of sub-pixel interaction position for some detectors. As a consequence, the depth resolution is also a function of sub-pixel interaction position. This effect is impossible to correct or model with the current analog ASIC.

5.5 Sensitivity Calculation

If we calculate the sensitivity image directly

$$s_j = \sum_i t_{ij} \tag{5.44}$$

the t_{ij} for all possible interaction combinations needs to be computed for each direction and energy. If the x, y, z location and the energy are separated into 11, 11, 15 and 500 bins, respectively, in a 18 detector system, there are more than 1.6×10^7, 2.6×10^{14}, 4.3×10^{21} and 7.1×10^{28} different events we need to consider for single-, two-, three and four-interaction events for each direction and energy, respectively. This direct calculation would take years to compute. Another way to acquire the sensitivity image is to directly measure or simulate the detection probability for each direction and energy. One can simulate or measure sources for all energy and directional bins then calculate the fraction of detected photons to the total photon emission from the source for each source energy and direction. Direct measurement is preferable since it can include some of the model miss matches such as the dead layer near the anode surface. However, it is nearly impossible to measure the detection probability for 500 energy bins and impractical to measure 18×18 source directions individually. Measuring a handful of energy lines for several unique directions and interpolating the detection probability for other directional and energy bins may be a practical solution.

Xu [11; 59; 60] proposed a way to compute the sensitivity by performing Monte Carlo simulation with just one source. A large sampling of the detector response for a source that is uniformly distributed over all energies of interest and all directions is simulated. Then the MLEM deconvolution method in combined energy and spatial domain is applied to the recorded events from this simulation. The first iteration of MLEM solution f^1 is the sensitivity image. This method is deduced from the fact that if we start with the true source distribution (a uniform image in energy and space in this case), the next MLEM iteration should converge toward the MLEM solution. With enough statistic, the MLEM solution and the true source distribution are very close to each other. So it is reasonable to assume $f^0 \approx f^1$. In other words, if the true source image is the start image, the result image after the first iteration of MLEM
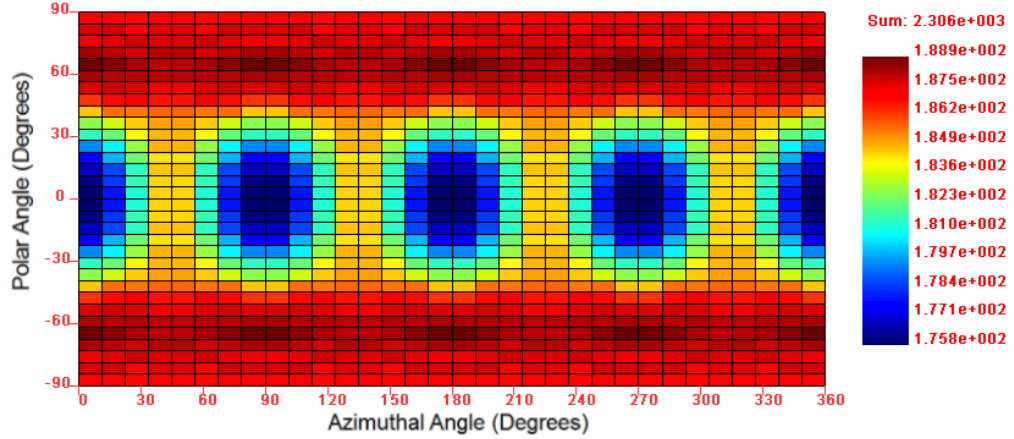
Figure 5.4: The sensitivity image for a 18-detector array in the energy range of 200 keV to 250 keV.

divided by the sensitivity factor should be the very close to the start image which is the true source distribution. From equation (5.5)

$$f_j^1 = \frac{f_j^0}{s_j} \sum_{i=1}^{I} \frac{t_{ij}}{\sum_k t_{ik} f_k^0} \tag{5.45}$$

$$\hat{s}_j \approx \sum_{i=1}^{I} \frac{t_{ij}}{\sum_k t_{ik} f_k^0} \tag{5.46}$$

Figure 5.4 shows the sensitivity image in the source energy range of 200 keV to 250 keV for a 18-detector array system. As expected, the dominant factor of the detection probability for a low energy photon is the area of the cross section, while the depth is more important for the high energy photon detection probability as shown in figure 5.5. Figure 5.5 is the sensitivity image in the energy range of 1600 keV to 1650 keV for the same 18-detector array.
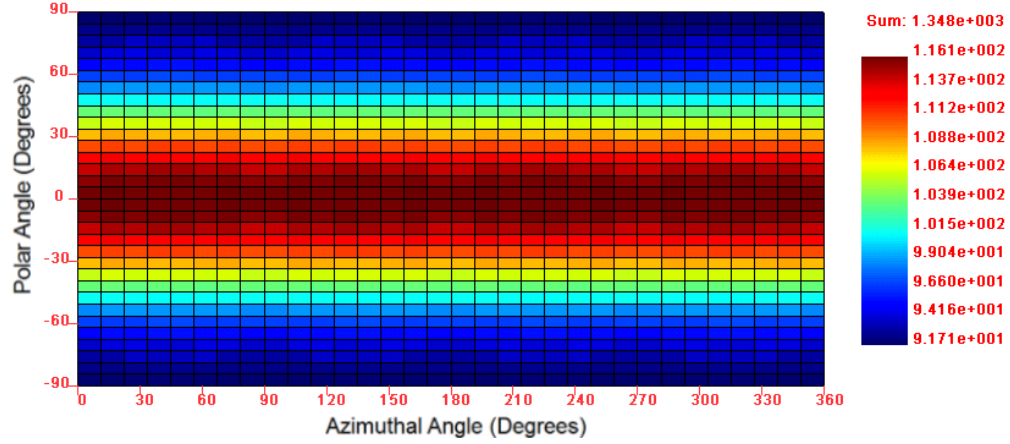
Figure 5.5: The sensitivity image for a 18-detector array in the energy range of 1600 keV to 1650 keV.

5.6   Performance

The angular resolution of an imaging system can be indirectly measured from the FWHM of the image of a point source. However, the definition of the angular resolution is the minimal angular distance between two sources that can be differentiated in the reconstructed image. The angular resolution varies for different detector geometries. For a single large CdZnTe detector (2 cm × 2 cm × 1.5 cm), the simplified MLEM spatial-only deconvolution has an angular resolution of less than 10 degrees.

In this chapter, a measurement of three different radioactive sources is used to examine the imaging performance of the system response functions derived in this section. In addition, multiple repetitions of an experiment with a single source are performed to find the statistical uncertainty in these maximum-likelihood deconvolution results. Due to the reasons described in the previous section, single-interaction events are not used in the reconstructions. In this section, two-, three- and four-interaction events are used in the deconvolutions.

For each experiment two algorithms are performed. First, deconvolution is done in a combined spatial and energy space using the full system model considering both full-

energy- and partial-energy-depositions; second, a simplified spatial-only deconvolution only using the full-energy case is also performed. For this spatial-only maximum-likelihood deconvolution, energy windows around the photopeaks are used to select the full-energy-deposition events that match the photopeak-only system model. No sensitivity image is used in this simplified deconvolution method since reconstructed intensities will be skewed anyway due to the Compton continuum from higher energies.

The detector array consisted of four 2 cm × 2 cm × 1.5 cm CdZnTe detectors. Since this array was designed for testing purposes, the detectors used had relatively poor spectroscopic performance and uniformity compared to other detectors we have tested. The full width at half maximum (FWHM) energy resolution at 662 keV was 1.07% for single-pixel events from the whole array.

5.6.1   Maximum-Likelihood Expectation-Maximization Image Reconstruction Using Multiple-Interaction Events

A measurement was performed with three sources in three different directions: a 14-μCi Cs-137 source 30 cm away from the center of the detector array, a 24-μCi Na-22 source 46 cm away from the center of the detector array and a 2-μCi Co-60 9 cm away from the center of the detector array, as shown in figure 5.6.

First, maximum-likelihood spatial deconvolutions were performed in energy windows for each of the three sources: 460 keV to 560 keV for Na-22, 600 keV to 700 keV for Cs-137 and 1100 keV to 1200 keV for Co-60. In the energy window from 1100 keV to 1200 keV, there were 9405 single-interaction events, 35331 two-interaction events, 28402 three-interaction events, and 12044 four-interaction events. Therefore, including three- and four-interaction events with the two-interaction events increased imaging efficiency by 110%. Figure 5.7 shows the superposition of the maximum-likelihood spatial-only deconvolution image from each energy window with a panoramic picture

of the laboratory. The image was reconstructed with a 180×180 rectangular mesh, and the expectation-maximization algorithm was performed with 25 iterations. The reconstructed image from each energy window is shown in a different color. The hotspots in the image are located in the correct source directions.

In another reconstruction, figure 5.8 shows the angular FWHM from each of the image hotspots by using spatial-only deconvolution method with two-, three-, and four-interaction events individually and combined. Figure 5.8 is from the first iteration of the deconvolution, starting with a uniform image, using 500 events in each reconstruction. The first iteration of the deconvolution is similar to the SBP image where the blur is introduced by the position and energy resolution of the detector-array system. In figure 5.8, the width of the hotspot decreases as the number of interactions increases due to less interaction-sequence ambiguity [53]. Compared to the Cs-137 measurement, the angular FWHM from combined two-, three-, and four-interaction events from a Co-60 source is closer to the FWHM from only four-interaction events, due to the fact that four-interaction events are more common in higher-energy events. These relative widths persist through iterations.

Figure 5.9 is a three-dimensional view of the results from the maximum-likelihood deconvolution in a combined spatial and energy domain using both the full- and partial-energy-deposition model. The reconstruction was performed with two-, three-, and four-interaction events in an energy range of 0 MeV to 2 MeV. The 4π spatial domain was divided into a 64×64 mesh and the energy domain was divided into 500 energy bins. The sensitivity image used in this deconvolution was calculated from a Monte-Carlo simulation [55]. The three axes are the dimensions of energy, polar angle and azimuthal angle. The intensity in each image voxel is the estimated incident intensity of photons from each incident direction and energy. In the reconstructed image, the hot regions are located in the energy range of 660 keV to 664 keV in the Cs-137 direction, 508 keV to 512 keV and 1272 keV to 1276 keV in the Na-22 direction,
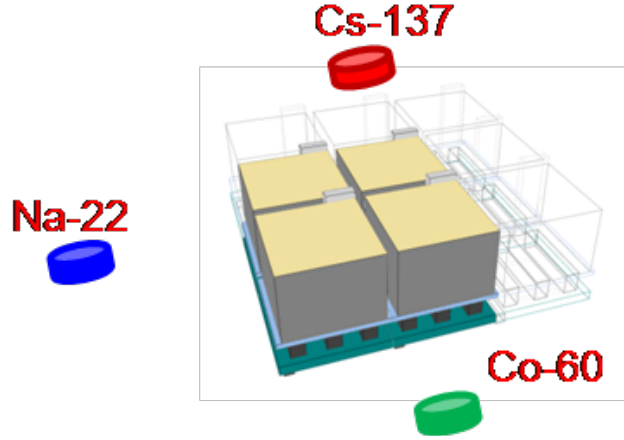
Figure 5.6: A diagram of the source arrangement for a measurement with Cs-137, Na-22 and Co-60 sources.

and 1172 keV to 1176 keV and 1332 keV to 1336 keV in the Co-60 direction. From this three-dimensional view, it can be seen that the results from this deconvolution algorithm using both the full- and the partial-energy deposition model give the source direction at the peak energies as well as the incident spectrum for each direction. As in the simplified deconvolution case, a larger fraction of the events were used in the reconstruction by including three- and four-interaction events in the deconvolution; the deconvolved spectra preserve the same Compton-continuum-free property as only using two-interaction events.

5.6.2 Statistical Uncertainty of the Deconvolution

Figure 5.10 shows the average reconstructed image using the maximum-likelihood deconvolution in the spatial domain with 1000 two-, three-, and four-interaction pho-topeak events from a measurement with a 30-μCi Cs-137 source after 20 iterations. Figure 5.10(a) shows the full reconstructed image. It is clear that the point source can be found in the detector array's cathode direction at the top of the image. This experiment was repeated 20 times. After 20 iterations, the total image value within 15 degrees of the cathode direction is on average more than 870 counts. Since the
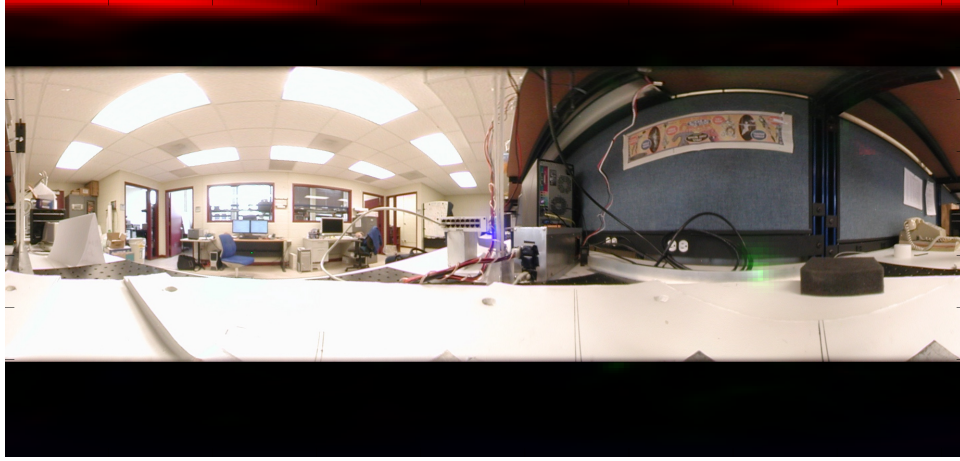
Figure 5.7: The spatial deconvolved image from a simultaneous measurement with Cs-137, Na-22, and Co-60 sources, overlaid on an optical panoramic image. The images for energy windows around the primary emission lines of Cs-137, Na-22, and Co-60 are shown in red, green, and blue, respectively.
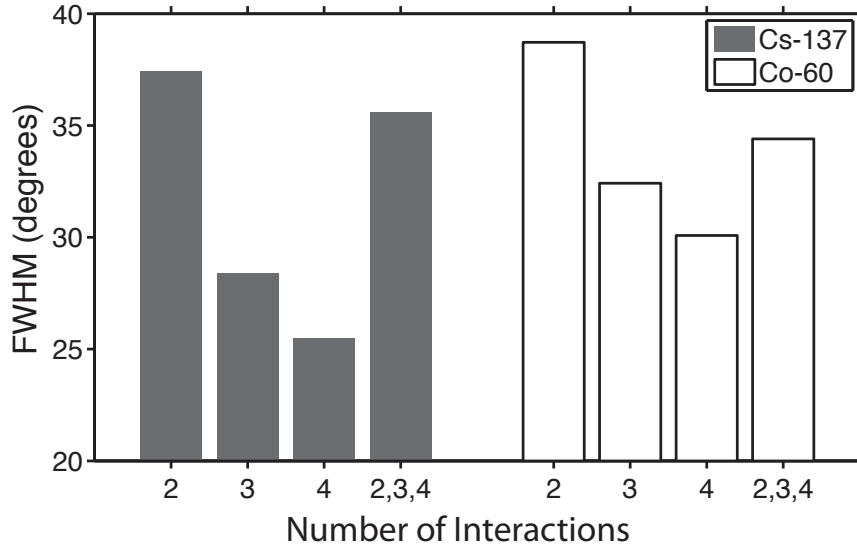
Figure 5.8: The comparison of the spatial FWHM in the first iteration of MLEM reconstruction with 500 two-interaction, three-interaction, and four-interaction events individually and 500 combined two-, three-, and four-interaction events from a Cs-137 and a Co-60 source. For the Cs-137 source, the reconstructed events were selected with total energy between 620 keV and 680 keV. For the Co-60 source, the reconstructed events were selected with total energy between 1140 keV and 1350 keV.
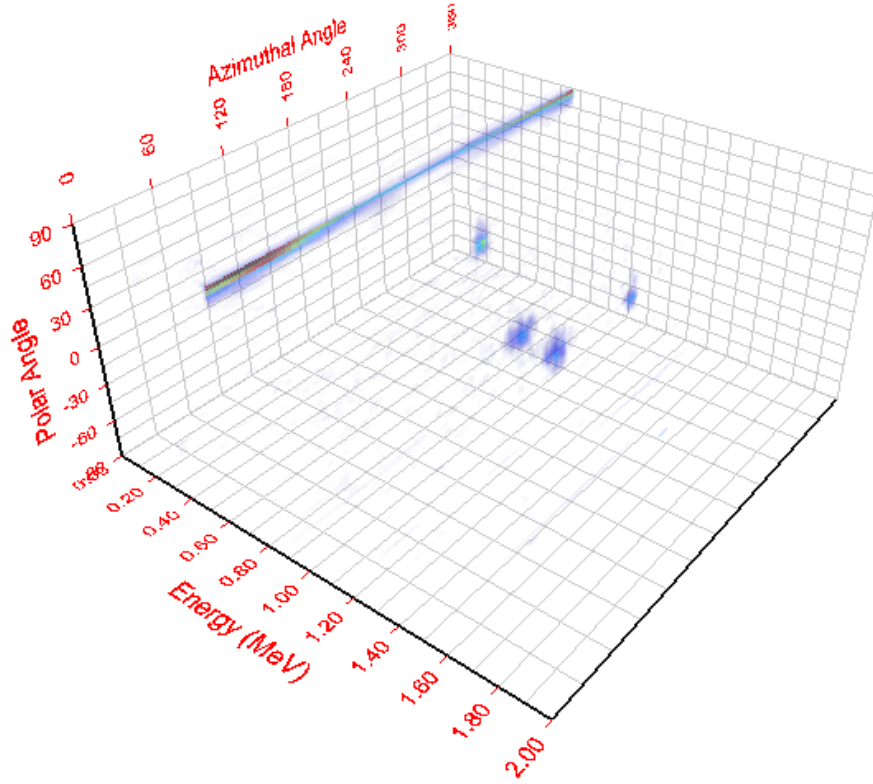
Figure 5.9: Reconstructed energy-image using maximum-likelihood deconvolution in a combined spatial and energy domain with the three-source measurement in figure 6.1.

maximum-likelihood expectation-maximization algorithm conserves the total number of counts, more than 87% of the 1000 reconstructed events were located around the correct direction after 20 iterations. Figure 5.10(b) shows the percentage mean and the standard deviation of the image value in each pixel around the source direction.

The same method was used to find the uncertainty when deconvolving in both energy and spatial domains with the full system model. A single 30-μCi Cs-137 source was measured, and 1000 two-, three-, and four-interaction events were used in the reconstruction. The image was divided into a 18×18 mesh, and each energy bin was 4 keV wide. This experiment was performed 20 times. Figure 5.11 shows the mean deconvolved spectrum in the source direction and the standard deviation from repetitions. The centroid of the peak is 662.4 keV $\pm$ 0.9 keV.
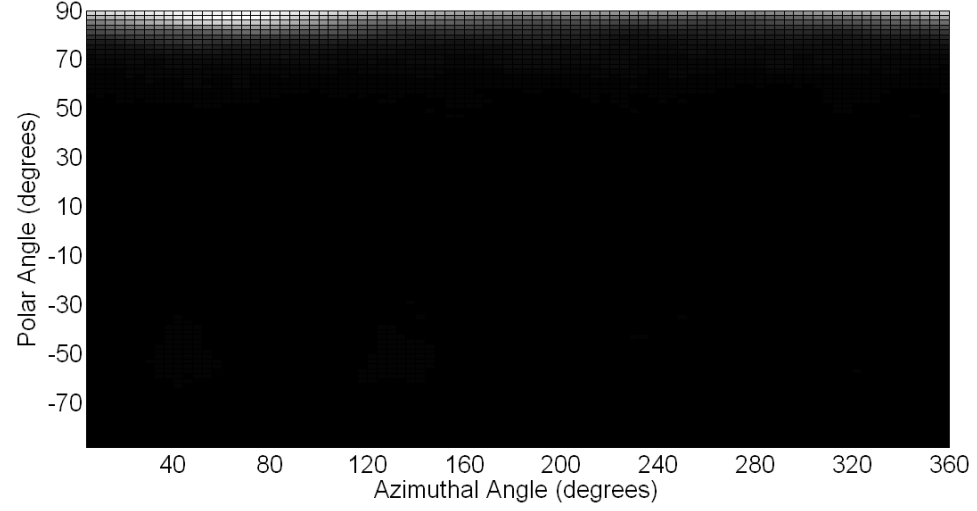
(a)
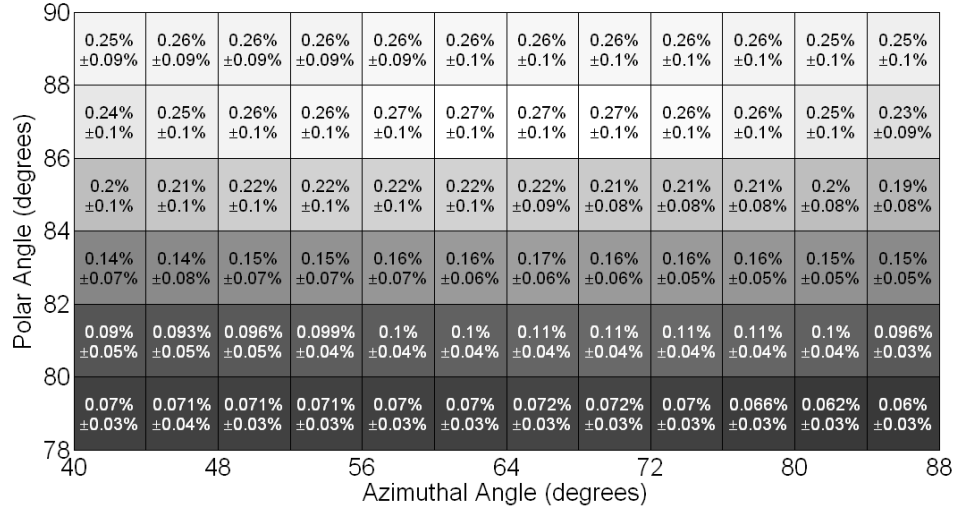
(b)

Figure 5.10: (a) The reconstructed image from 1000 photopeak events from a Cs-137 source placed almost in the cathode direction of the detector array. (b) A detail of the hot region (polar angle of 78 degrees to 90 degrees and azimuthal angle of 40 degrees to 88 degrees). The mean and the standard deviation of the number of counts for each pixel after 20 iteration is shown in each pixel as a percentage of the total image value.
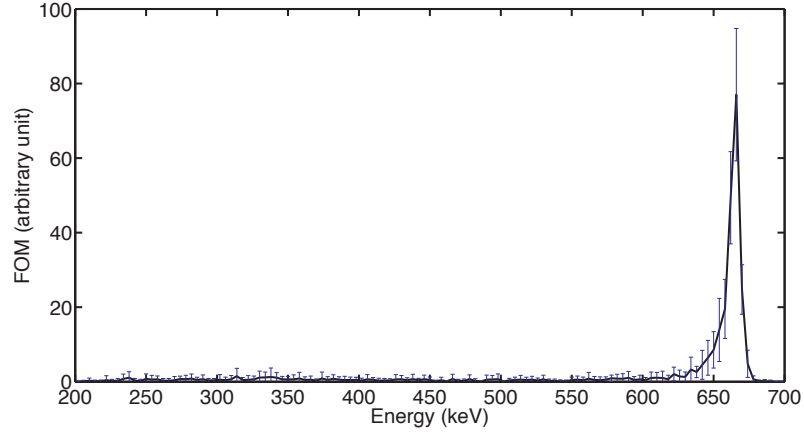
Figure 5.11: The mean and the standard deviation of each energy bin in the deconvolved spectrum for the source direction by using the maximum-likelihood deconvolution in a combined spatial and energy domain with 25 iterations for 1000 two-, three, and four-interaction events. 20 repetitions are used to calculate the mean and standard deviation.

71

CHAPTER VI

Applications of the Energy-Imaging Integrated Deconvolution Algorithm for Source Characterization

6.1 EIID with A Three-Source Measurement

We use the same measurement described in section 5.6.1. The measurement was performed with three sources, a 14-μCi Cs-137 at 30 cm away, a 24-μCi Na-22 at 46 cm away, and a 2-μCi Co-60 at 9 cm away from the center of the detector array, in three different directions, as shown in figure 6.1. Figure 6.2 is the result from the MLEM deconvolution in the combined energy and directional image domain, also known as the energy-imaging integrated deconvolution (EIID) algorithm. The three axes are the deconvolution dimensions of energy, and polar and azimuthal angles, and the intensity of the image voxel is the estimate of the spectral intensity of photons from each direction striking the detector. As expected from this algorithm, this deconvolved spectrum reflects the theoretical branching ratio emitted from each source, as shown in figure 6.3. The ratio of the peak areas at 511 keV and 1274 keV in the Na-22 direction is almost 1.99, shown in the red bar. It is very close to the ratio of the theoretical emission probabilities of 2, shown as the dotted line in figure 6.3(a). For the Co-60 direction, the ratio of peak areas at 1173 keV and 1333 keV is about 0.99,

which is also very close to the theoretical ratio of 1.0. The green bars show the ratio of peak areas from the raw spectrum over all directions, which is very different from the theoretical branching ratio.
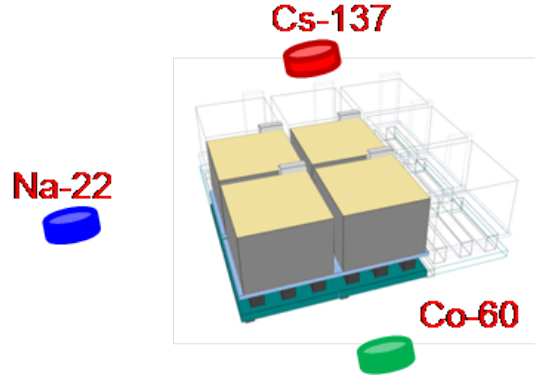
Figure 6.1: A diagram of the source arrangement for a measurement with Cs-137, Na-22 and Co-60 sources.

6.2 Estimation of the Source Intensity

From these incident spectra we can estimate the source intensity. The absolute magnitude of the deconvolved spectrum was calibrated by measuring a Cs-137 source. After applying EIID, the calibration factor can be calculated using the source activity, measurement time, emission probability, solid angle, and dead-time factor compared to the total area of the deconvolved spectrum.

$$calibration\ factor = \frac{number\ of\ emitted\ photon}{deconvolved\ spectrum\ area} \tag{6.1}$$

With this single calibration factor we can turn this spectrum into the number of emitted photons at a certain distance. If the isotope is known, the activity of the source can be estimated. The measurement with Cs-137, Na-22 and Co-60 was performed 50 times to get the statistical uncertainty of the estimated source intensity. Figure 6.4 shows the estimation of the number of photons emitted from the sources for the known
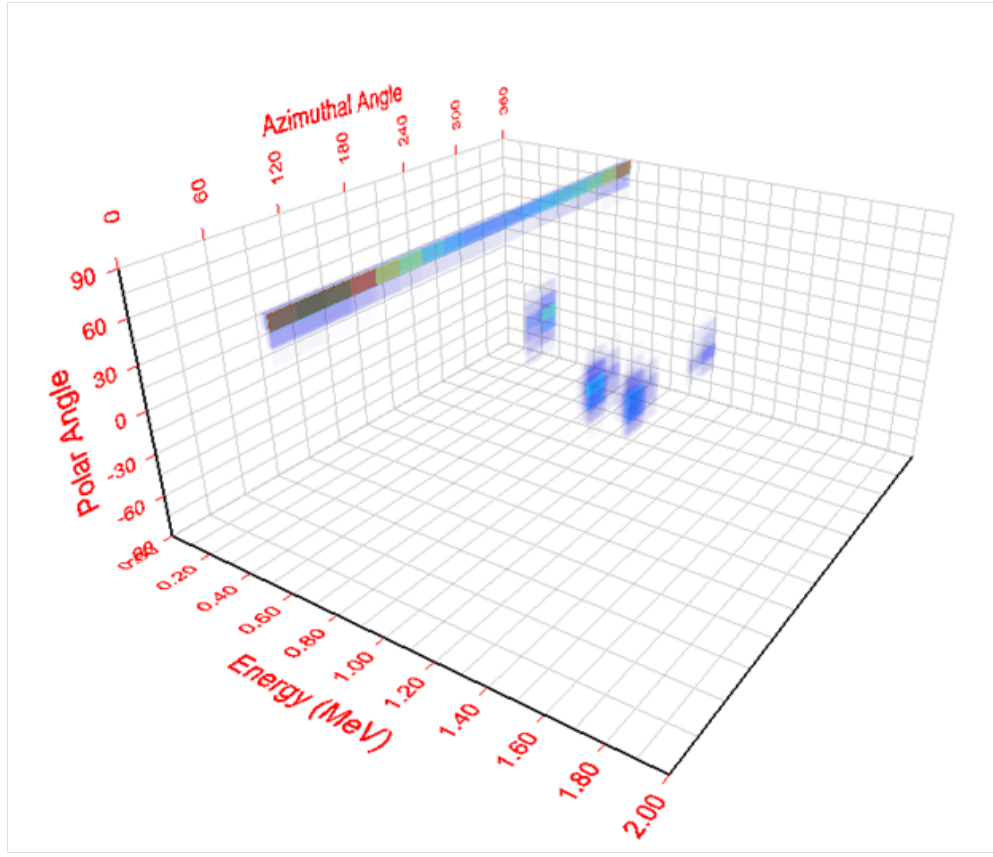
Figure 6.2: Reconstructed energy-image using the EIID algorithm with the three-source measurement in figure 6.1.

(a) Na-22 direction

(b) Co-60 direction
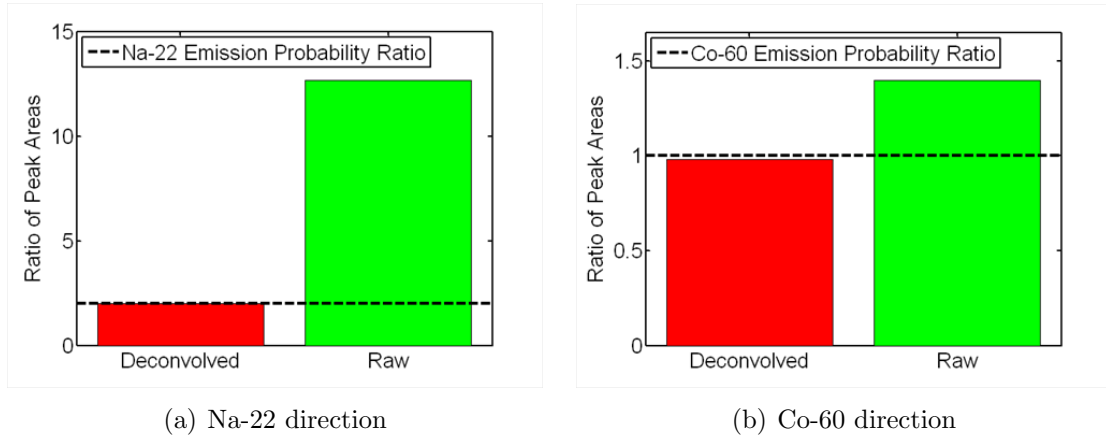
Figure 6.3: Comparison of the peak areas ratio for the two emission lines of the given source using the raw (green bar) and the deconvolved spectra (red bar) with the ratio of the emission probabilities of the source (dashed line). The deconvolved spectra were selected from the source directions

distance. With a simulated sensitivity image to correct for both energy and spatial efficiency variation, the estimated source intensity, shown in red, is within 10% of the true intensity, which is shown as the dotted line. As expected the estimated source intensity is closer to the true intensity when applying the efficiency correction. The statistical uncertainty of the source intensity estimates ranges from 1% to 5%.
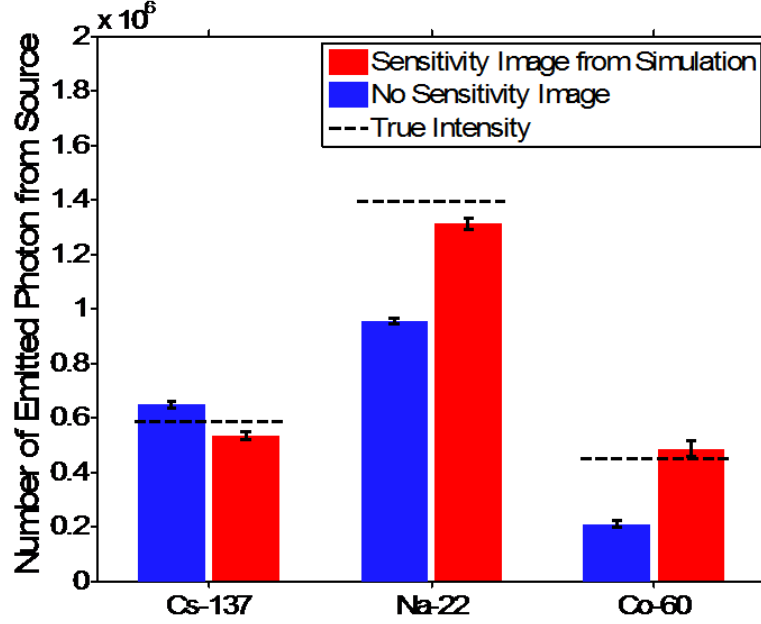
Figure 6.4: Estimates of the number of emitted photons from each source from the EIID spectrum in the direction of each source.

It is difficult to theoretically predict the uncertainty of the estimated source intensity from a single EIID result. In order to study the statistical error of the EIID deconvolved spectrum in a certain direction, a Cs-137 source was measured multiple times at 30-cm away from the center of the detector array on the cathode direction. 1000 events were used for each EIID reconstruction. The statistical uncertainty in the deconvolved full-energy peak area is just below 10%, as shown in figure 6.5. Multiple repetitions of a simulation were also performed using Geant4 [61] with the same source and detector geometry in order to see the effect of reducing the model mismatch when experimental effects, such as shielding from the detector housing,

pixel-jumping, weighting potential anode dead layer and non-Gaussian peak shape, are removed. The uncertainty was reduced to 5.5%, so a large portion of the statistical uncertainty seems to be due to model mismatch. By changing the source from 30-cm away to far-field in the simulation, the uncertainty reduced to about 4%. So, a small portion of the statistical uncertainty is due to the near-field effect. By increasing the number of events in each reconstruction to 2×10^4 and still using the far-field simulation, the uncertainty further dropped to around 1%. Therefore, counting statistics seem to be a limiting factor on statistical precision even after 1000 collected events.
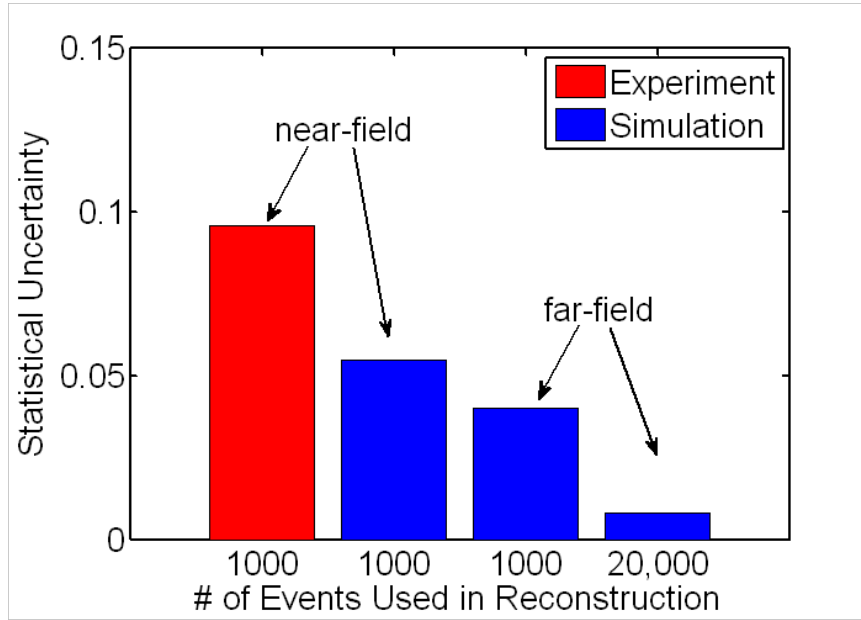
Figure 6.5: Statistical uncertainty of the EIID spectrum area using different types of data and different number of events.

6.3 Directional Isotope Identification

Isotopes can also be identified with the EIID spectrum in the source direction using the fact that an unshielded source will have peak area proportional to the theoretical branching ratios. A method [62] is proposed to calculate a figure of merit (FOM) that each isotope is present, defined as the ratio of the peak area to the

emission probability that is associated with the peak energy. For example, in order to calculate the FOM for Na-22 in a certain direction, we measure the spectrum area of the 511 keV and 1274 keV first, and then divide the peak area by the associated emission probabilities, which is 2 for 511 keV and 1 for 1274 keV. Now we have two FOM values from two energy lines of Na-22. The smaller FOM will be selected for this isotope in order to prevent amplifying the noise due to small emission probabilities or incorrectly identifying due to the presence of just a subset of the expected peaks. For the same reason, this method was only applied for the energy lines that have an emission probability above 1%. The FOM values for other isotopes can be achieved by following the same procedure. After going through every source in a library of 20 sources, the results in figure 6.6 show Co-60, Na-22 and Cs-137 have the largest figure of merit for the Co-60, Na-22 and Cs-137 source directions, respectively. The FOM value of K-40 in the Na-22 direction is caused by amplifying the noise by dividing the emission probability of 10.7% around 1462 keV. The figure 6.7 is a histogram of 50 repetitions of this experiment. The x-axis is the FOM for each direction, and the y-axis shows the frequency of each FOM value. This histogram shows that in this experiment, the correct isotopes for each direction can easily be identified. However, the disadvantage of this method is that it does not use all peaks to form the FOM value, so more statistical noise is present.

In order to use all peaks to determine the presence of isotopes in each direction, another method is developed by summing all spectrum areas that are associated with the peak energies of an isotope. Since the deconvolved spectrum is the directional incoming spectrum, the summation of the peak areas in the deconvolved spectrum is a FOM that represents an estimate of the number of photons that strike the detector surface from an isotope in each direction. The same data from the three-source measurement is used to evaluate this algorithm. Figure 6.8 is the result from this peak-area-summation method in the Na-22 source direction. Using this new result,
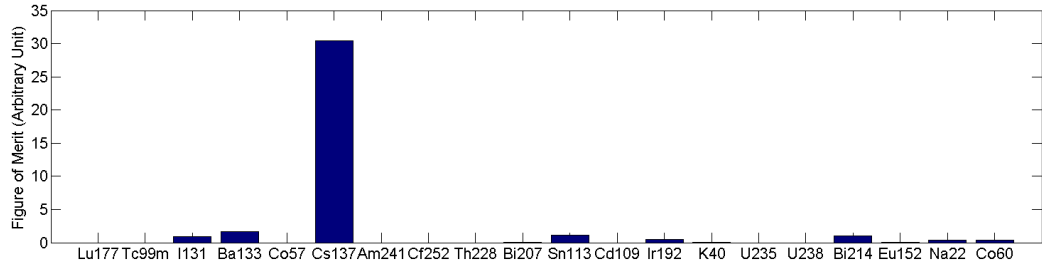
(a) Cs-137 direction
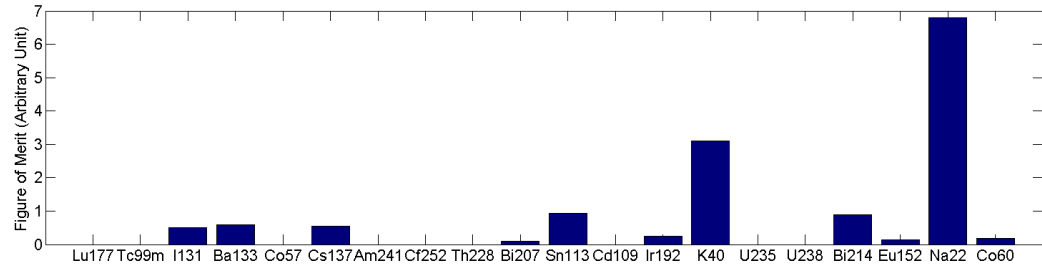
(b) Na-22 direction
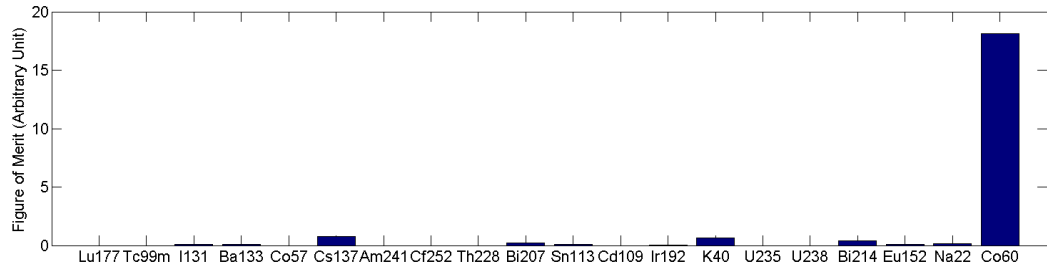
(c) Co-60 direction

Figure 6.6: The FOM of each source in the library for each source direction.
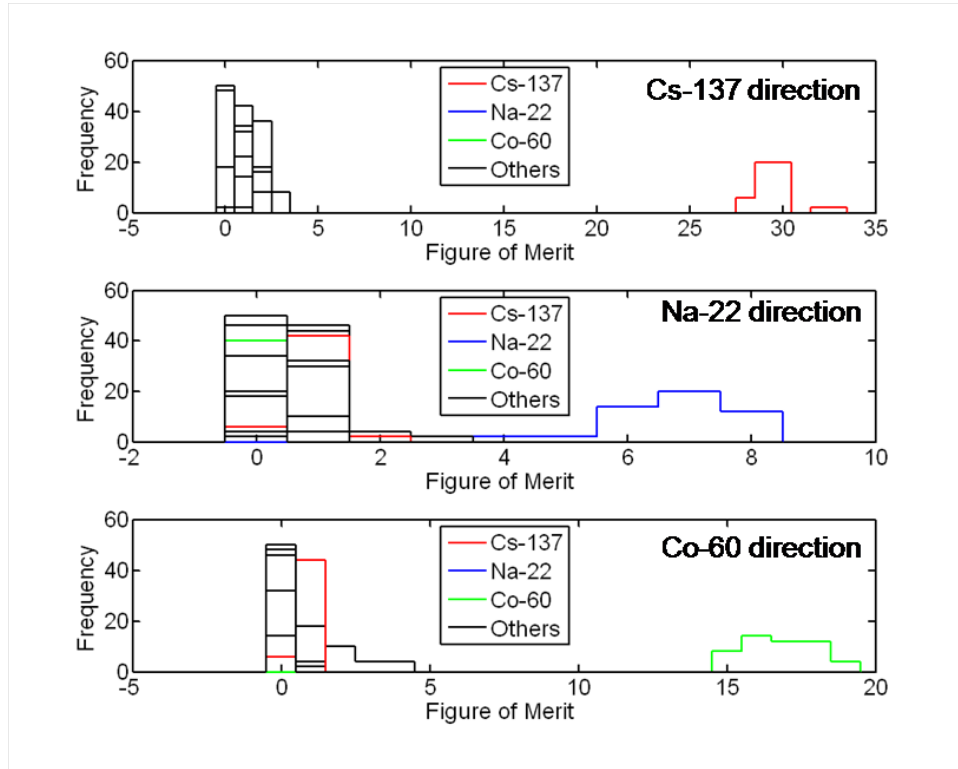
Figure 6.7: Histograms of 50 isotope identification experiments from the three-source measurement. The top, middle and the bottom figures are from the spectra in the Cs-137, Na-22 and Co-60 directions, respectively. The x-axis is the FOM value and the y-axis is the frequency of each FOM value.

the FOM values of the wrong sources are less pronounced compared to the previous result shown in figure 6.6(b). The FOM of K-40 in figure 6.6(b) is created from amplifying the noise around its photopeak energy at 1462 keV more than 9 times after dividing its emission probability of 10.7%. This noise is only summed once and is not amplified by small branching ratios in the peak-area-summation method. However, due to the non-negativity property of the MLEM estimator, all statistical noise in the deconvolved spectrum has a positive value. Therefore, this peak-area-summation method is inherently biased toward isotopes with more photopeaks since more statistical noise and background counts contribute to the FOM. In order to suppress the background level, the mean amplitude of all energy bin in the deconvolved spectrum is subtracted from each energy bin of the deconvolved spectrum. In this way, the correct isotope always has the largest FOM value. After 50 repetitions of this experiment, the histogram of the FOM values of each source in each source direction, shown in figure 6.9, has a bigger gap between the correct and incorrect sources than the previous result in figure 6.7.
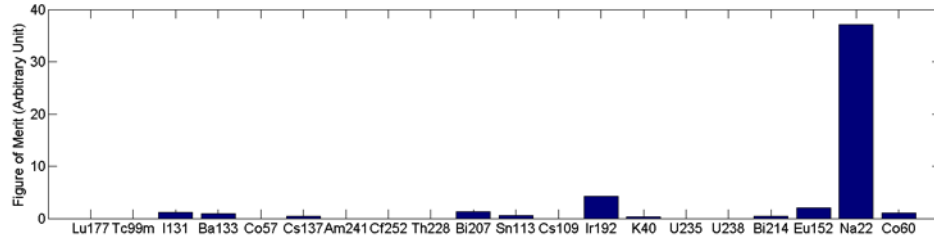
Figure 6.8: The FOM in Na-22 source direction by using the peak-area-summation method with the deconvolved spectrum from the three-source measurement.

When it is possible that more than one source is present in the direction of interest, this method is performed to initially identify the isotope with the largest FOM. The identification method is then repeated after removing the peaks from identified sources until no peak in the deconvolved spectrum is greater than three standard deviations of
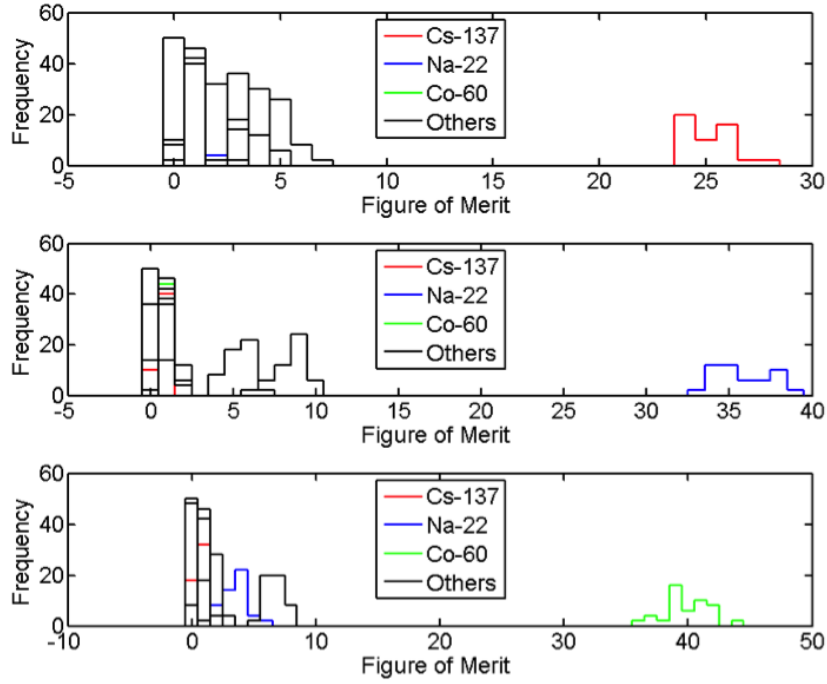
Figure 6.9: Histograms of 50 isotope identification experiments from the three-source measurement. The top, middle and the bottom figures are from the spectra in the Cs-137, Na-22 and Co-60 directions, respectively. The x-axis is the FOM value and the y-axis is the frequency of each FOM value. This figure is created using the peak-area-summation method with the same data used in figure 6.7.

the spectrum. When multiple isotopes contribute to a peak region, one of the isotopes with unique photopeaks is identified. The peak areas of this identified isotope are calculated from the area of its biggest unique photopeak and the relative emission probabilities at each photopeak energies. The calculated peak areas are than removed from the deconvolved spectrum. Figure 6.10 can be achieved by using this method with the deconvolved spectrum in all directions from the three-source measurement.
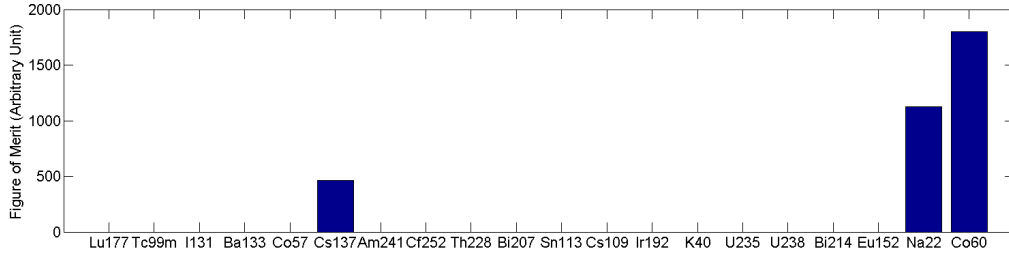
Figure 6.10: The FOM of identified isotopes in all directions by using the peak-area-summation method with the deconvolved spectrum from the three-source measurement.

Traditional isotope identification methods using the raw measured spectrum may have better performance due to the fact that a significant number of single-interaction events in the raw spectrum can not be used in the EIID algorithm (in a practical timely fashion). However, the isotope identification methods presented in this section provide a unique direction-dependent result.

A probability-based directional isotope identification method, isotope-imaging integrated deconvolution (IIID), is described by Wahl [44]. IIID essentially uses the same method and system model as EIID, but it uses a set of isotope bins instead of evenly distributed energy bins as basis functions. The IIID algorithm performs better in the scenario of multiple isotopes that share the same photopeak in the spectrum since it can estimate the most probable contribution from each possible isotope based on the emission probabilities. The flip side of this advantage is, compared to the methods presented in this chapter, the results from the IIID are more dependent on the agreement between the measurement and the model. In addition, when back-

ground from the environment is present in the measurement, EIID deconvolves the background events into a large number of energy bins, instead of forcing them into a handful of isotope bins. Therefore, the isotope identification methods from the EIID spectrum have less background noise for each isotope.

6.4 Image Shielded Sources

As illustrated in figure 6.11, if a gamma-ray source is shielded, some photons from the source will be scattered in the shielding material before reaching the detector, while other photons will reach the detector without any interaction in the shield. The scattered photon will often carry lower energy than the initial photon from the source. Therefore, the image from a shielded source should appear more blurred around the true source location at lower energies compared to that from an unshielded source. If the photons only scattered once in the shield by Compton scattering, photons scattered to lower energies correspond to greater scattering angles, so the image at lower energies should have a wider diffuse source region. Photons scattered more than once in the shield will result in a more blurred image. [63]

A single 2-cm × 2-cm × 1.5-cm three-dimensional position-sensitive room-temperature CdZnTe detector was used in an experiment. A 30-μCi Cs-137 source was placed near the detector. Figure 6.12 shows the reconstructed image using the MLEM deconvolution in combined energy and spatial domain. A point-like hotspot is clearly shown in the reconstructed image at 662 keV. By placing a 3.7-cm thick steel block between the source and the detector, the image in figure 6.13 is produced using the same deconvolution algorithm. A diffuse image from the scattered photons can be seen at energies less than 662 keV. The area of the high-intensity region increases for image slices at lower energies, which agrees with the theoretical expectation from the Compton scatter formula. This bowl-shaped smear is also shown in figure 6.14 for a 1-μCi Co-60 source shielded with 2.7 cm of lead.

Another experiment was performed by measuring a 30-μCi Eu-152 source behind 1.8 cm of steel on one side of the detector and a 10-μCi Cs-137 source without any shielding on the opposite side of the detector. Figure 6.15 shows the reconstructed image where a point-like hotspot appears at the Cs-137 direction, while the smear from the scattered photons can be easily identified in the Eu-152 direction at energies lower than the photopeaks. The deconvolved (incident) spectrum at the Eu-152 source direction with and without the 1.8-cm steel shield is shown in figure 6.16. The low-energy peaks are significantly smaller compared to the others, which agrees with the fact that the attenuation coefficient in the shield increases for lower energy photons.
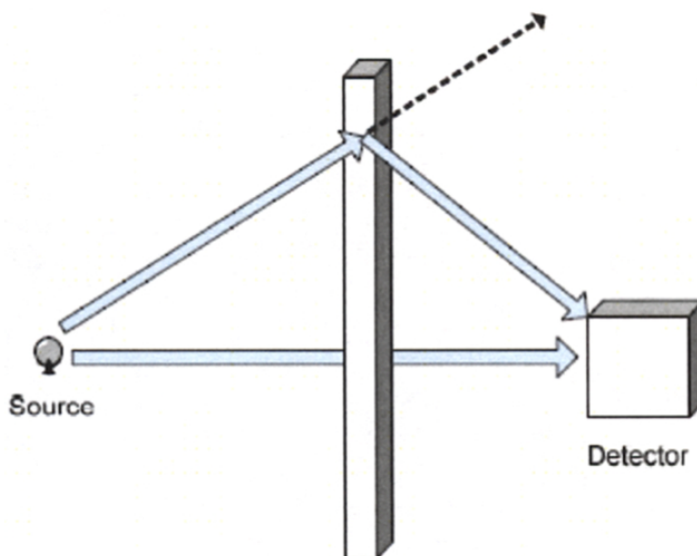
Figure 6.11: A block of shielding material exists between a source and a detector.

6.5   Estimation of the Shielding Material

A direct way to estimate the shielding material is by trying to detect the characteristic X-ray peaks in the recorded spectrum. For example, figure 6.17 shows the recorded spectrum from the measurement that created figure 6.14 in section 6.4. The characteristic X-ray from lead can be seen clearly around 80 keV. However, the characteristic peak can only be detected if its energy is above the software trigger
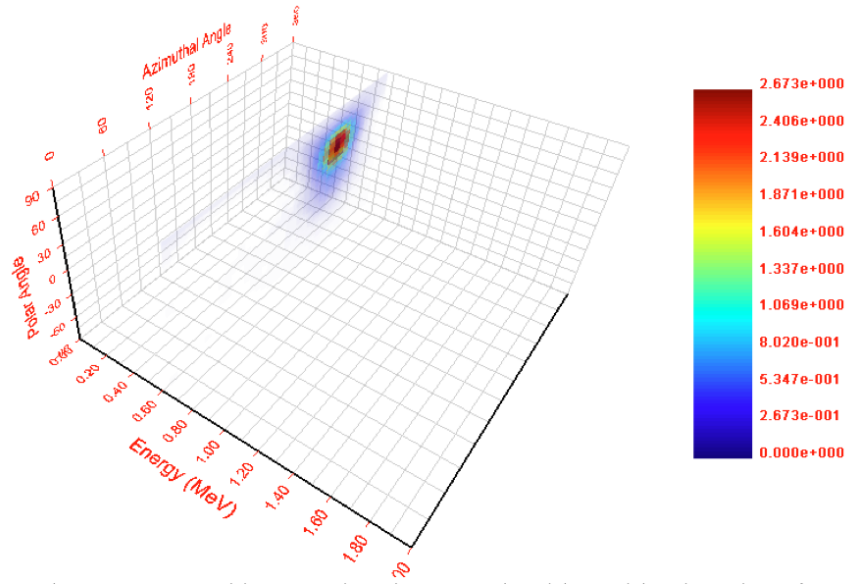
Figure 6.12: The reconstructed image using the EIID algorithm with 5 iterations for 21879 two-interaction events from a Cs-137 source with no shielding. Two axes of this plot show the angular positions around the detector and the last shows the incident energy of the photons. The color is proportional to the intensity.
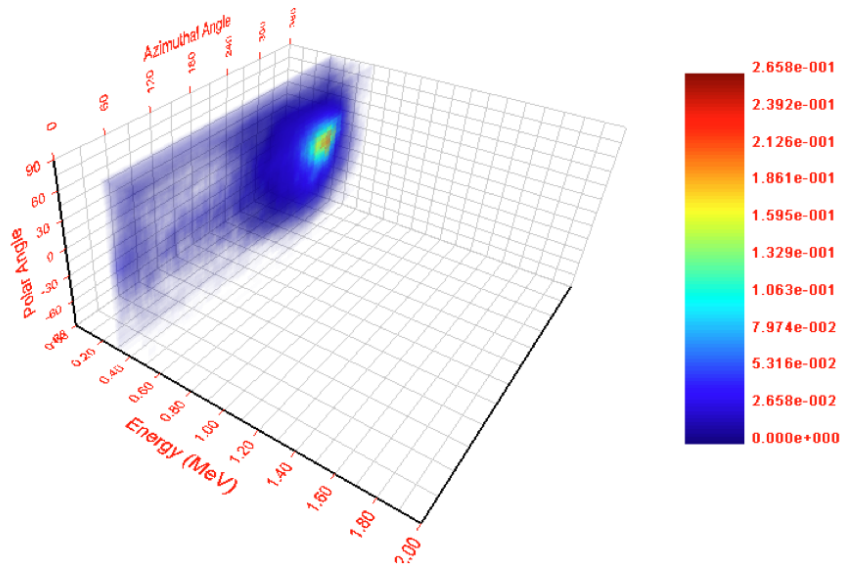
Figure 6.13: The reconstructed image using the EIID algorithm with 5 iterations for 21879 two-interaction events from a Cs-137 source behind 3.7 cm of steel shielding. Two axes of this plot show the angular positions around the detector and the last shows the incident energy of the photons. The color is proportional to the intensity.
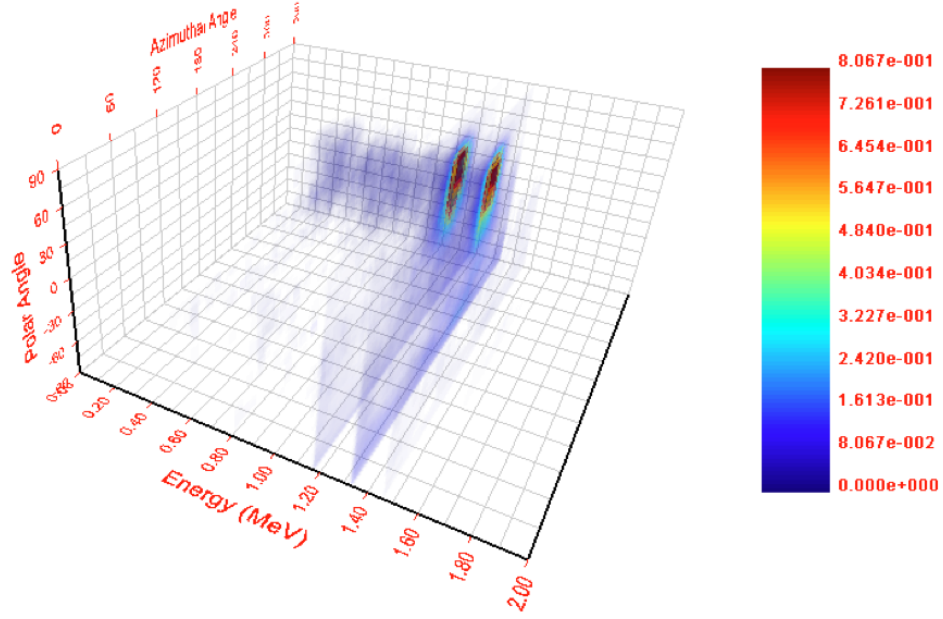
Figure 6.14: The reconstructed image using the EIID algorithm with 5 iterations for 28120 two-interaction events from a Co-60 source shielded by a 2.7cm-thick lead block. Two axes of this plot show the angular positions around the detector and the last shows the incident energy of the photons. The color is proportional to the intensity.

threshold (30 keV) of our detector system. Therefore, the characteristic X-ray from steel, which has an energy around 7 keV, cannot be detected.

As shown in figure 6.16, the change in peak area depends on the gamma-ray energy. The changes of the peak areas in the deconvolved spectrum at different energies can be used to estimate the material's atomic number and thickness. [62] The attenuation of two emission energies from a single source can be described by equations of the form

$$I'_1 = I_1 e^{-\mu_1 x} \tag{6.2}$$

$$I'_2 = I_2 e^{-\mu_2 x} \tag{6.3}$$

where I_1 and I_2 are the initial intensities, I'_1 and I'_2 are the attenuated intensities, μ_1 and μ_2 are the attenuation coefficients at those energies, and x is the thickness of the shielding.
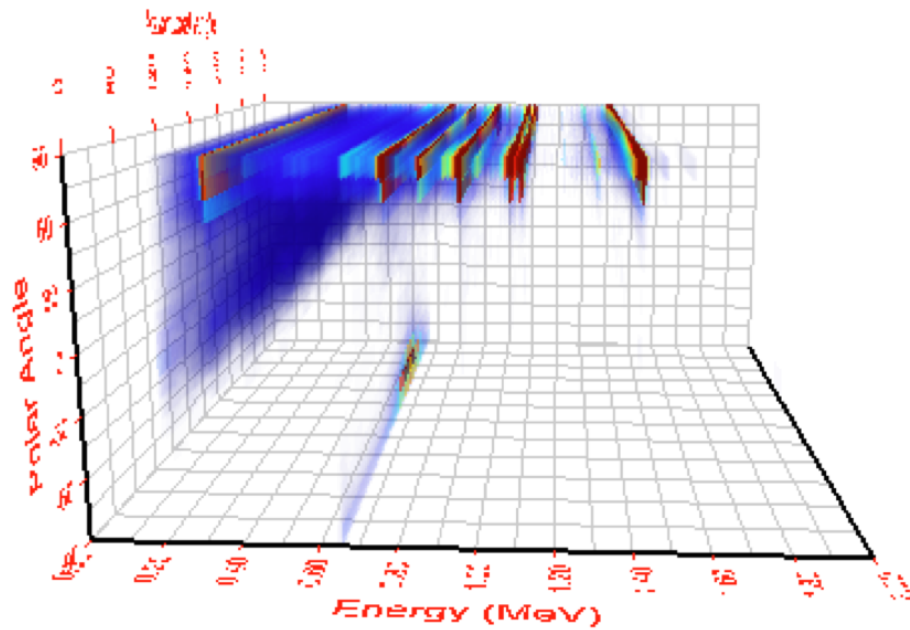
Figure 6.15: The reconstructed image using the EIID algorithm with 10 iterations for 457285 two-interaction events from a Eu-152 source behind 1.8 cm of steel shielding and a Cs-137 source without any shielding. Two axes of this plot show the angular positions around the detector and the last shows the incident energy of the photons. The color is proportional to the intensity.
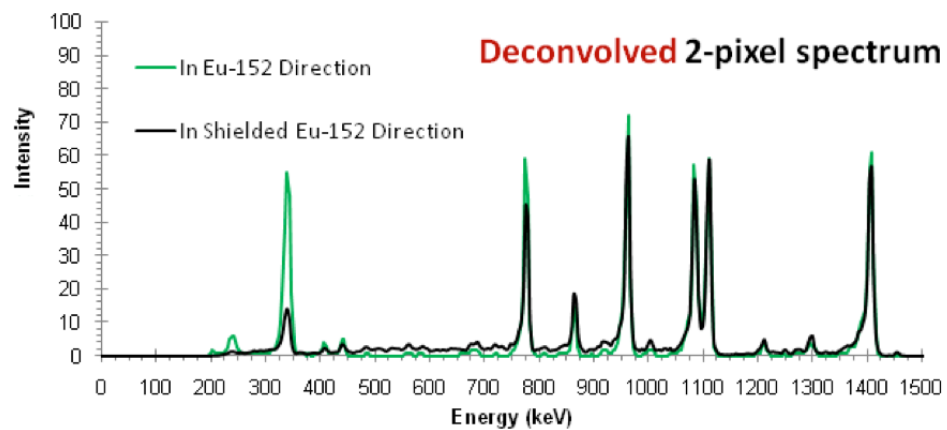
Figure 6.16: The deconvolved spectrum in the Eu-152 source direction with and without 1.8 cm of steel shielding. The EIID algorithm was used to deconvolve the incident spectrum.
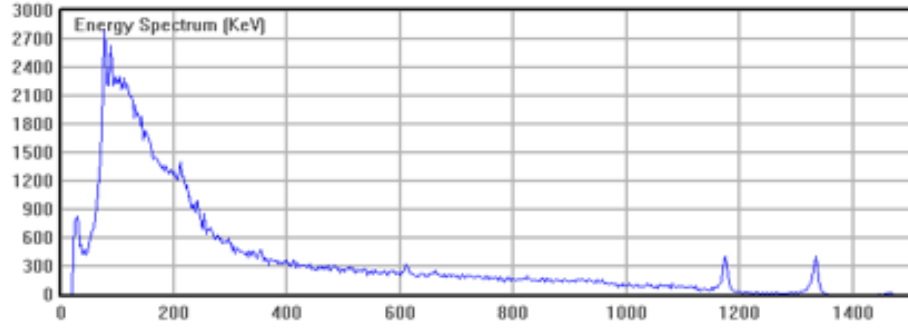
Figure 6.17: The raw energy spectrum recorded by the detector from a Co-60 source behind 2.7 cm of lead shielding.

Assume the atomic number z and the thickness x are constants. The difference between the log of the ratio of attenuated intensities and the log of the ratio of initial intensities should have a linear relationship with the difference of the attenuation coefficients, as

$$\ln(\frac{I'_1}{I'_2}) - \ln(\frac{I_1}{I_2}) = x(\mu_2 - \mu_1) \tag{6.4}$$

Therefore the z number can be determined by the attenuation coefficients that give the best linear fit. Then the thickness of the shielding x can be calculated based on the slope of the line.

A 30-μCi Eu-152 source was used in this experiment. The results reported from this algorithm are shown in table 6.1. Figure 6.18 shows the reported best linear fit for the data from 1.9 cm of steel. Although the algorithm cannot estimate the z number exactly, it can detect if the shielding material has a high atomic number, which is useful for many applications.

Table 6.1: The Results of the Estimated Atomic Numbers and the Thickness of Shielding Materials

Shielding z	Thickness (cm)	Estimated z	Estimated thickness (cm)
26 (steel)	1.9	27	1.5
50 (tin)	1.0	64	3.2
82 (lead)	1.0	80	1.1
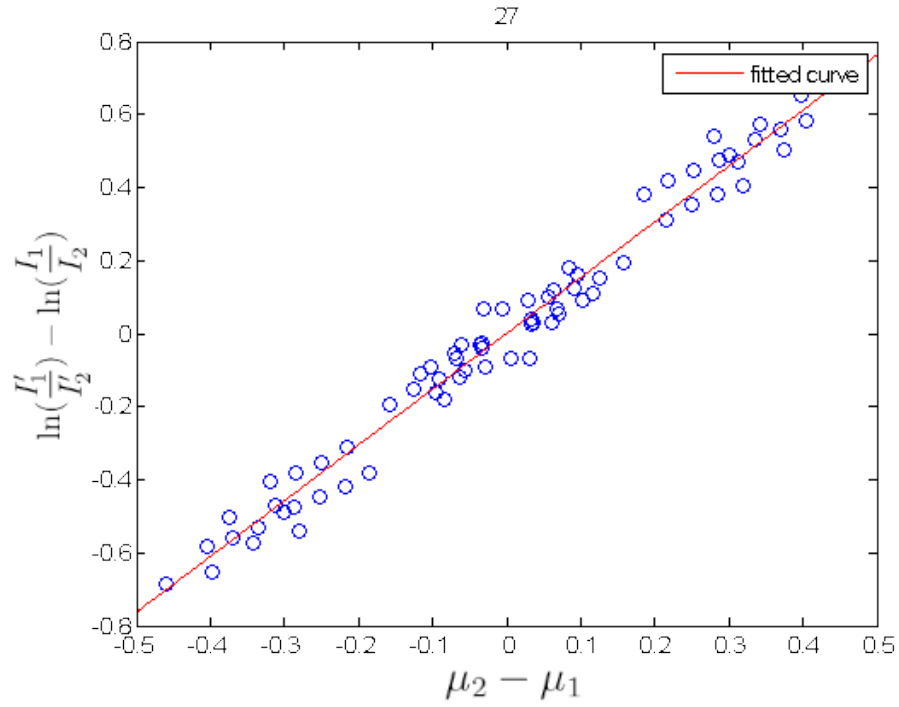
Figure 6.18: The best linear fit between $\ln(\frac{I_1'}{I_2'}) - \ln(\frac{I_1}{I_2})$ and $\mu_2 - \mu_1$ for the data from 1.9 cm of steel. The estimated atomic number from the best linear fit is 27. The thickness of the shielding is estimated to be 1.5 cm from the slope of the linear fit.

CHAPTER VII

Visualizing Natural Radiation Background

Humans have evolved in the presence of a natural radiation background. The radio-isotopes K-40, Th-232, and U-238 are responsible for the majority of natural radioactivity and human radiation dose. Radon, a decay product of U-238, is the second leading cause of lung cancer behind smoking [64]. Alpha-particles are the most biologically dangerous emissions from natural radioactive decay, but are difficult to detect and image due to a very short range. However, all the natural decay chains have unique gamma-ray emission signatures that are easy to identify with spectroscopy. Non-imaging spectrometers have been used in a series of static measurements to survey the natural gamma-ray background of an extended area [65].

7.1 Image Extended Sources

In order to show our imaging techniques are capable of reconstructing radiation distributions with a large spatial extent, a Monte Carlo simulation is performed using Geant 4 to model the detector response of a uniform part-spherical area source which emits 662 keV gamma rays. The uniform extended source covers a polar angle of -30 degrees to 30 degrees and an azimuthal angle of 150 degrees to 210 degrees. Figure 7.1 and figure 7.2 shows the reconstructed image by using the SBP method and the MLEM deconvolution in the spatial domain with 29 iterations, respectively.

The SBP image shows the correct source area with the highest intensity while having a high level background around the source area due to the build up of the incorrect portion of the Compton cones. The MLEM image has correct clear edges but is not uniform. The four corners are hotter than the middle. In order to prove that the non-uniformity of the reconstructed image is due to the sensitivity variation, the location of the extended source was moved 45 azimuthal degrees in the simulation. The new source covers polar angles of -30 degrees to 30 degrees and azimuthal angles of 195 degrees to 255 degrees. Figure 7.3 is the MLEM solution after 29 iterations. The hottest region is at an azimuthal angle of 225 degree which corresponds to the corner of the detector that has the largest cross section. This sensitivity variation can be included in the sensitivity factor for this particular energy [44]. However, if there is another source has a energy line higher than 662 keV that exists in the measurement, the sensitivity factor will be determined by the relative intensity of the two sources due to the fact that the simplified spatial-only MLEM deconvolution can not deconvolve the Compton continuum back to the photopeaks. Therefore, without the prior knowledge of the source energy, no single sensitivity image can be selected.
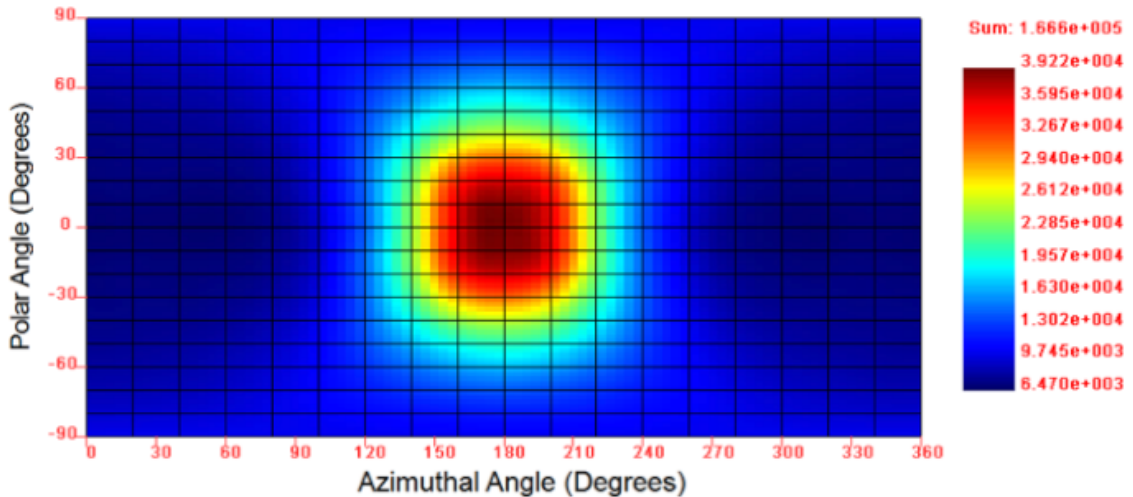
Figure 7.1: The reconstruction of a 60 degrees (polar) by 60 degrees (azimuthal) spherical source by using SBP reconstruction. Only photopeak events are used in this reconstruction.
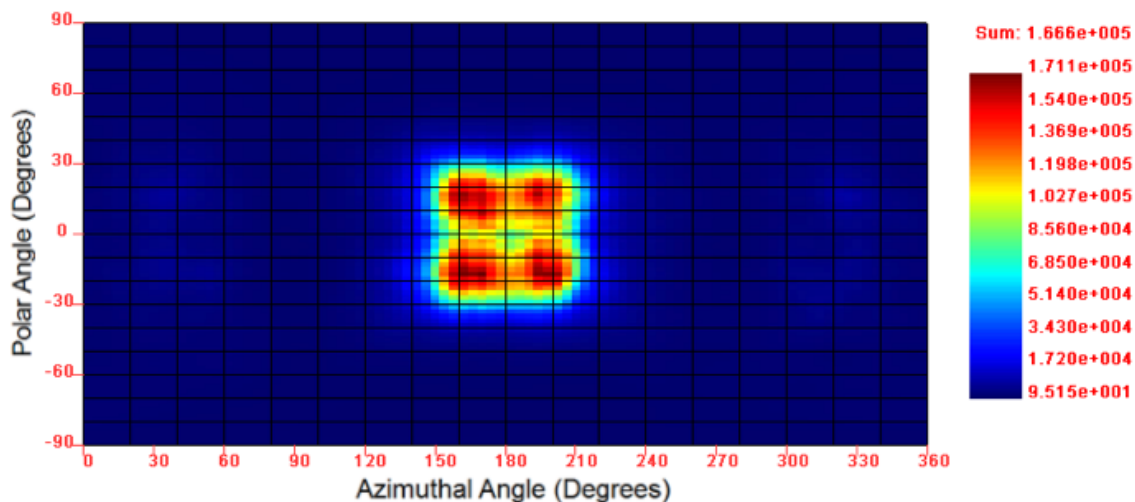
Figure 7.2: The reconstruction of a 60 degrees (polar) by 60 degrees (azimuthal) spherical source using MLEM deconvolution in spatial domain with 29 iterations. Only photopeak events are used in this reconstruction.
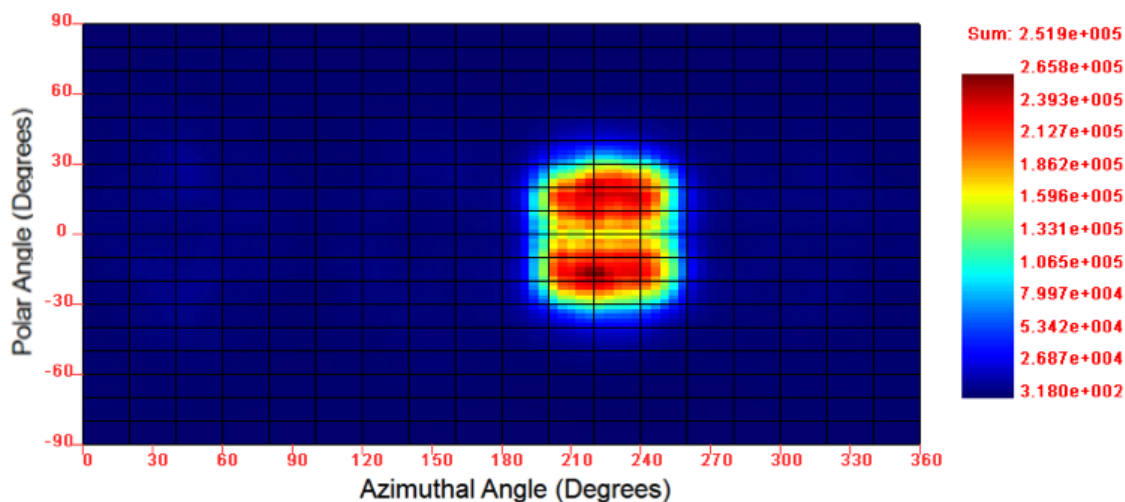
Figure 7.3: The reconstruction of a 60 degrees (polar) by 60 degrees (azimuthal) spherical source using MLEM deconvolution in spatial domain with 29 iterations. Compare to figure 7.2, the source was shifted 45 degrees in the azimuthal direction. Only photopeak events are used in this reconstruction.

Two sources with different activities were simulated using Geant 4. Both sources cover polar angles of -30 degrees to 30 degrees. The stronger source covers azimuthal angles of 60 degrees to 120 degrees while the weaker source covers azimuthal angles

of 240 degrees to 300 degrees. The stronger one is twice as active as the weaker one. In the reconstructed images, shown as figure 7.4 and figure 7.5, the intensity ratio between the two sources were close to 2 to 1.
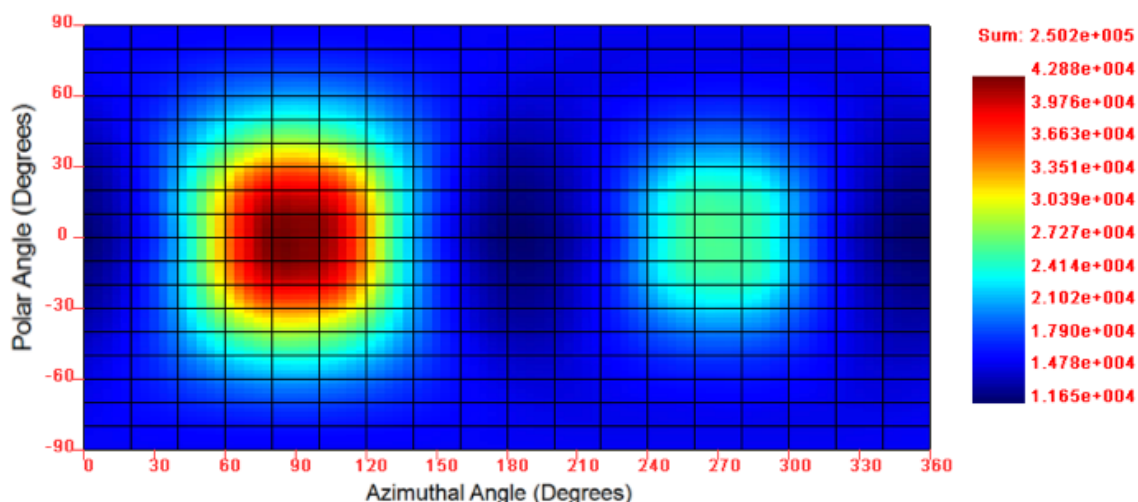
Figure 7.4: The SBP reconstruction of two extended sources. The ratio of activity of the left source to the right source is 2. Only photopeak events are used in this reconstruction.
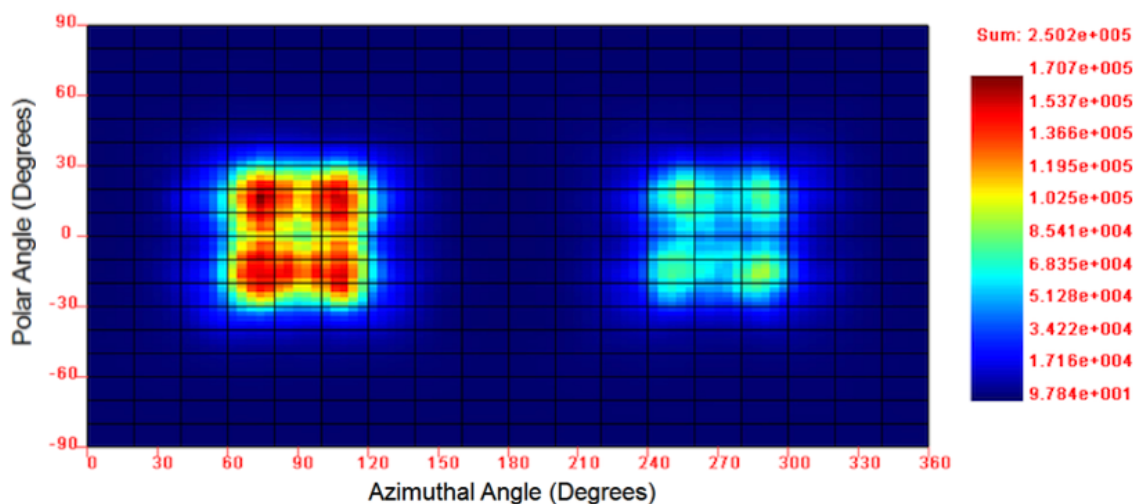
Figure 7.5: The reconstruction of two extended sources using MLEM deconvolution in spatial domain with 29 iterations. he ratio of activity of the left source to the right source is 2. Only photopeak events are used in this reconstruction.

7.2 Image the Natural Radiation Background

Xu [11] successfully reconstructed the natural radiation background using the SBP algorithm. However, there was a Cs-137 source present behind the nearest concrete wall. So the reconstructed image around 609 keV can be explained by the scattered photons in the concrete wall from the Cs-137 source in the next room.

In the new experiments, all experimental radioactive sources in the laboratory were heavily shielded to avoid contamination of the background. Two different natural background scenarios were imaged in our research laboratory to demonstrate the imaging capability of our system. First, we imaged a small room to show the contrast between large windows and concrete walls. Then, we imaged a room with concrete walls on all sides, but with shielding around the detector in certain directions, in order to create a known background scenario. A single CdZnTe detector with dimensions of 2 cm $\times$ 2 cm $\times$ 1.5 cm was used.

The geometry of the small lab used for the first experiment is shown in Figure 7.7[1]. The natural background was measured for one day. A conventional gamma-ray spectrometer would only be able to provide the energy distribution of the background environment, as shown in Figure 7.6. However, our system measures the intensity of the background radiation emissions in all directions. Figure 7.8 shows the reconstructed image using a SBP algorithm. Comparing figure 7.8 to figure 7.7, the most intense region of the reconstructed image is correlated with the closest concrete wall, centered at an azimuthal angle of 270 degrees. The least intense region of the reconstructed image is correlated with the window region, centered at an azimuthal direction of 180 degrees. The image regions associated with the partial window direction at 0 degrees and the distant wall at 90 degrees are of moderate intensity. All these observations agree with expectation: more gamma rays reach the detector when the source of natural background emission is in close proximity.

---

[1]Image from Feng Zhang, University of Michigan, Ann Arbor.
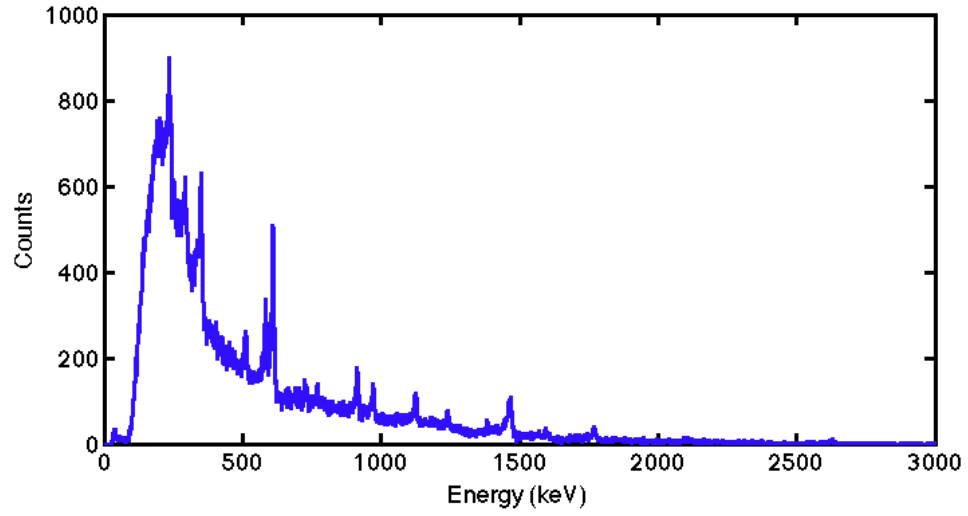
Figure 7.6: Energy spectrum of the natural radiation background.
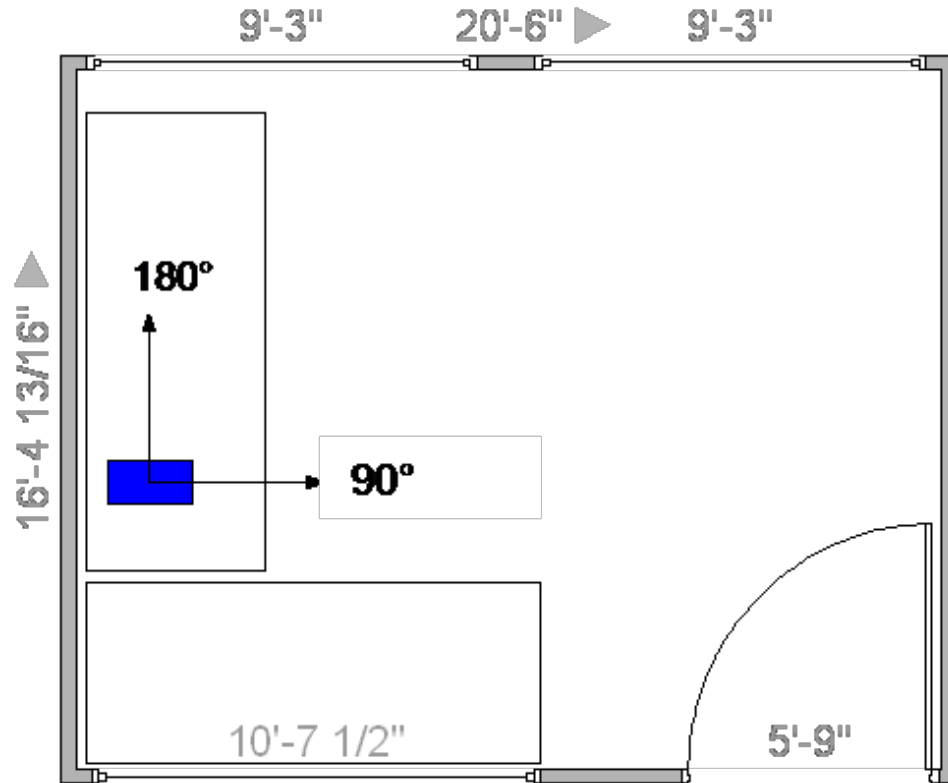
Figure 7.7: The configuration of the lab and the detector.
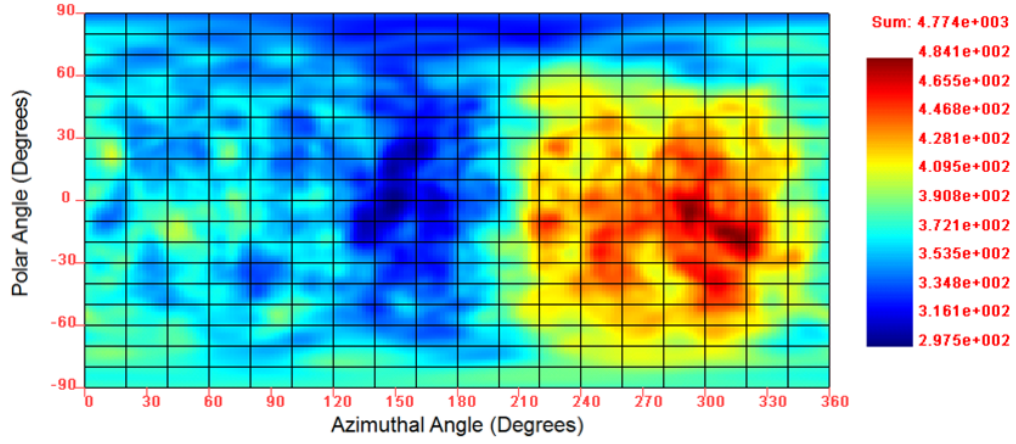
Figure 7.8: A reconstructed image of distribution of Bi-214 in the concrete wall by using SBP with 4774 events in energy window of 600-630 keV.

The detector was rotated 90 degrees, as illustrated in figure 7.9[2], in order to eliminate the possibility that the reconstructed image was influenced by a systematic bias. The SBP image generated from the rotated detector orientation is shown in figure 7.10. As expected, the features of the image have been rotated 90 degrees when comparing figure 7.8 to figure 7.10. Figure 7.11 and figure 7.12 show the result of overlaying an optical panoramic picture of the laboratory with the Compton image before and after the detector rotation, respectively. A camera with a panoramic lens was placed at the same location of the detector and rotated with the detector. In both figure 7.11 and figure 7.12, the distribution of the image intensity agrees with the proximity to the natural radiation source in each direction, such as a concrete wall.

The background images in our lab provide anecdotal evidence of the correlation between background sources and image intensity. More gamma-rays are observed in the direction of the concrete wall than in the direction of the window, and the image rotates with the detector. However, this experiment does not provide a rigorous comparison between a reconstructed image and a well defined background emission

---

[2]Image from Feng Zhang, University of Michigan, Ann Arbor.

96
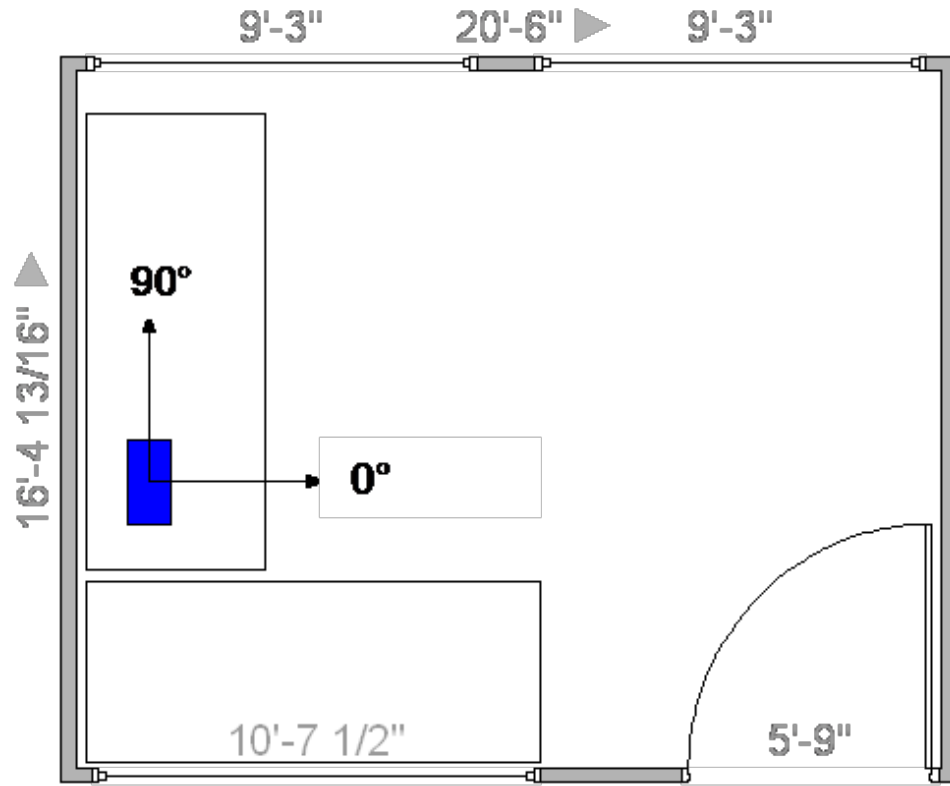
Figure 7.9: The configuration of the lab and the detector after 90 degrees rotation.
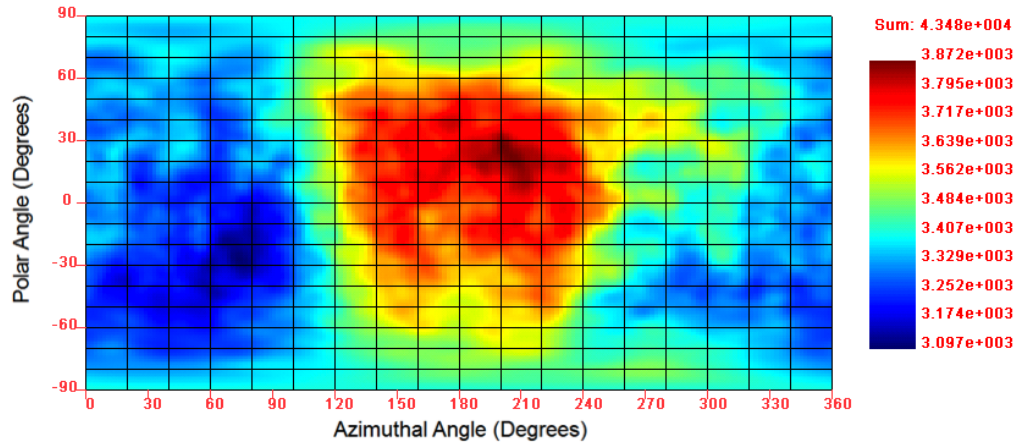
Figure 7.10: A reconstructed image of the distribution of Bi-214 in the concrete wall after rotating the detector 90 degrees by using SBP with 8219 events in energy window of 600-630 keV.

Figure 7.11: The result of overlaying Compton image with optical panoramic image before detector rotation.

Figure 7.12: The result of overlaying Compton image with optical panoramic image after 90 degrees of detector rotation.

scenario. The difficulty lies in creating a known background distribution when our detector system is the only device capable of creating such detailed images of the natural background. In order to overcome this difficulty, the detector was placed inside a lead tunnel with two openings equidistant from two concrete walls.

The use of 5-cm thick lead walls around the detector absorbs the vast majority of the natural radiation background. Therefore, the gamma-ray intensity should be at least an order of magnitude larger in the directions of the openings of the tunnel. Furthermore, the high intensity regions of the image can be predicted from the position of the detector within the lead tunnel. A change in detector position should correlate to a predictable shift in the reconstructed image.

The presence of the lead shielding eliminated most of the background events, requiring a very long measurement time of three days. In this experiment, two similar CdZnTe detectors were placed in different positions inside the lead tunnel. Figure 7.13 shows the reconstructed images from both detectors as well as the directions associated with cave openings for each detector. The reconstructed images are in good agreement with the cave openings, indicating the proper reconstruction of this known background scenario.

The recorded data from both experiments are then reconstructed by the MLEM deconvolution in the combined spatial and energy domain. Figure 7.14 shows the reconstructed image from the lead tunnel experiment. The two openings can be seen clearly. Every background energy line has a higher intensity in the concrete wall direction than the window direction in the deconvolved incoming spectra shown in Figure 7.15. Figure 7.16 shows the deconvolved spectrum in the lead direction which is near the statistical noise level while the opening has a much stronger radiation level from the concrete wall.
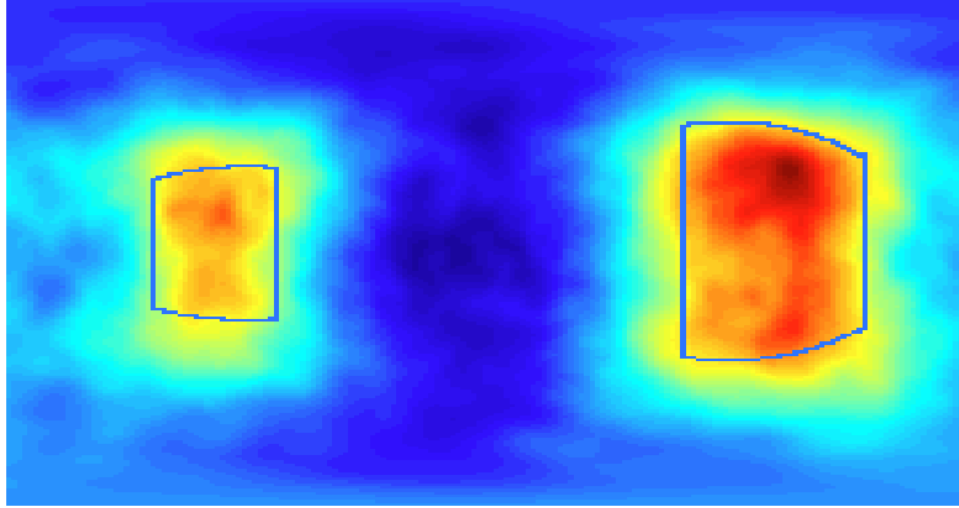
(a) Reconstructed image from detector 1. 55110 events are used in the SBP reconstruction.
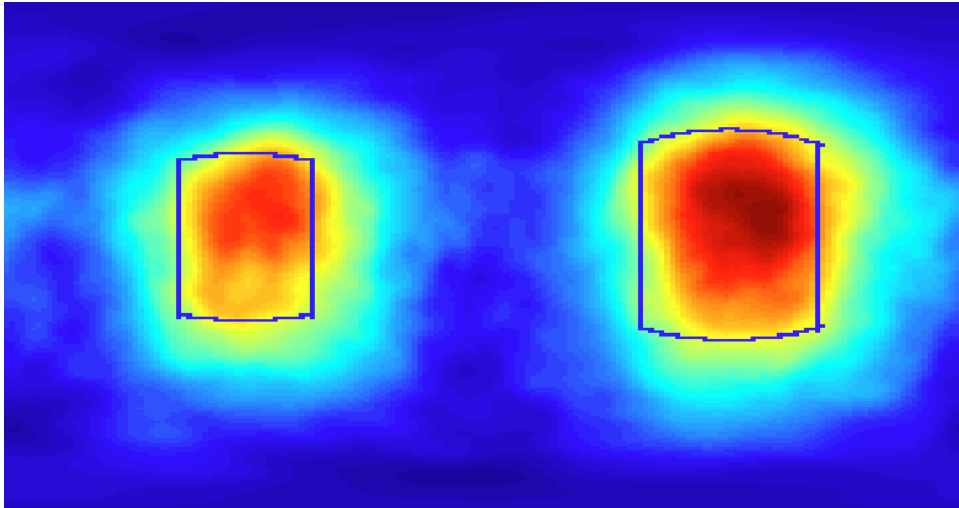
(b) Reconstructed image from detector 2. 53056 events are used in the SBP reconstruction.

Figure 7.13: The reconstructed image of the natural radiation distribution in the concrete through two openings of a lead tunnel by using SBP for two side-by-side detectors with events in the energy window of 300-2000 keV. The blue lines indicate the openings of the lead tunnel.
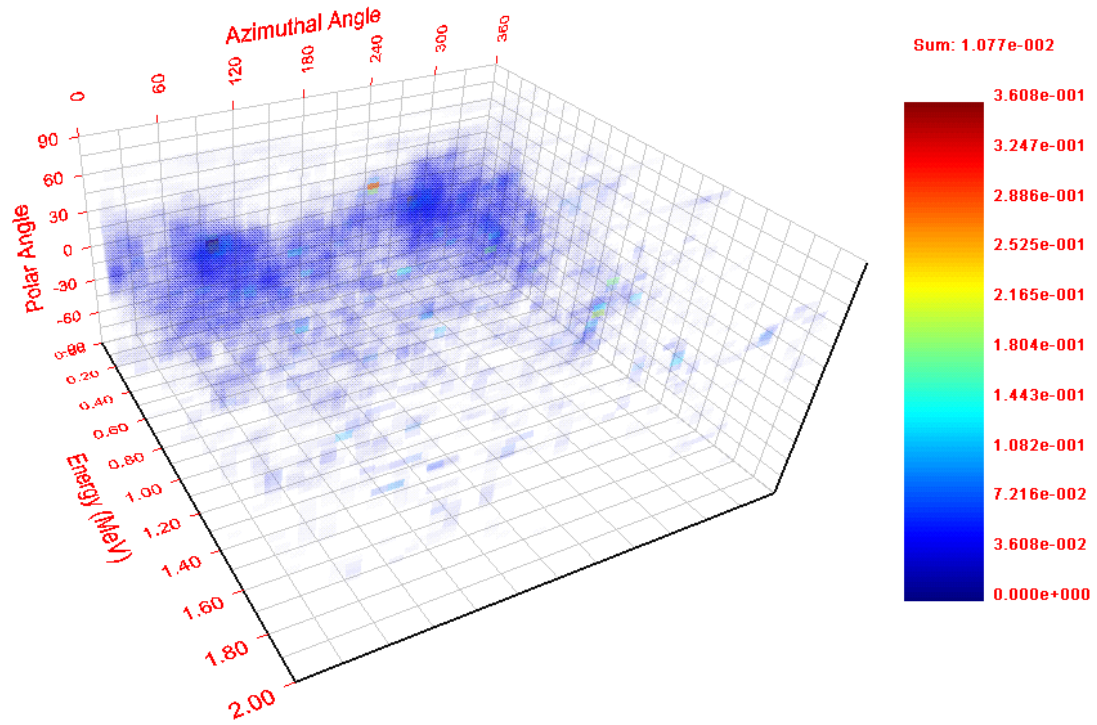
Figure 7.14: The result image from MLEM deconvolution in combined energy and spatial domain. Two tunnel openings can be seen clearly.
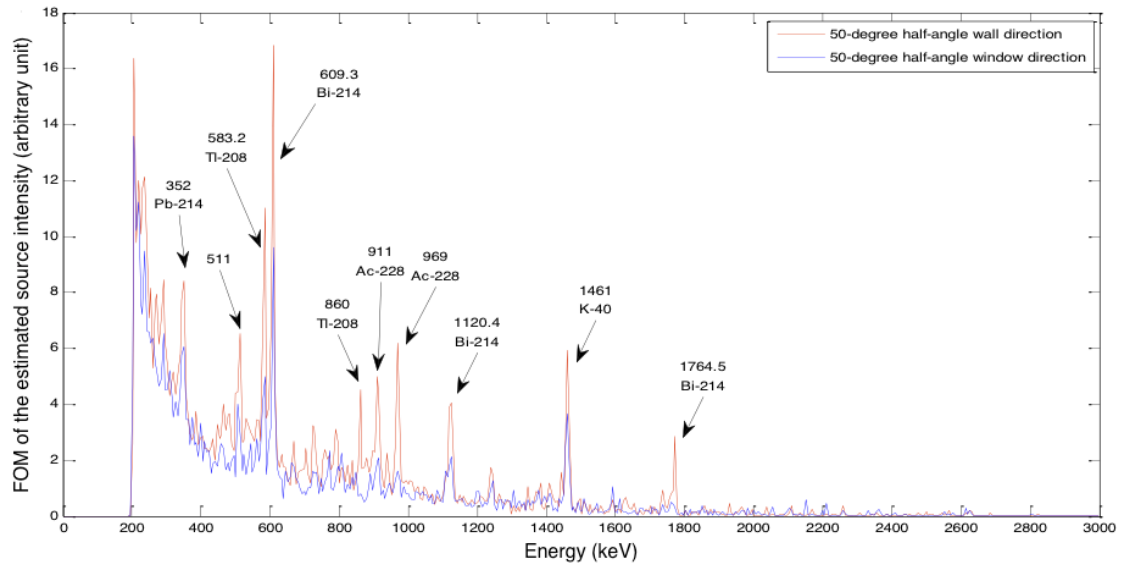
Figure 7.15: The deconvolved spectrum of a 50-degree half-angle region in the wall and window direction. The y axis is the figure of merit of the source intensity.
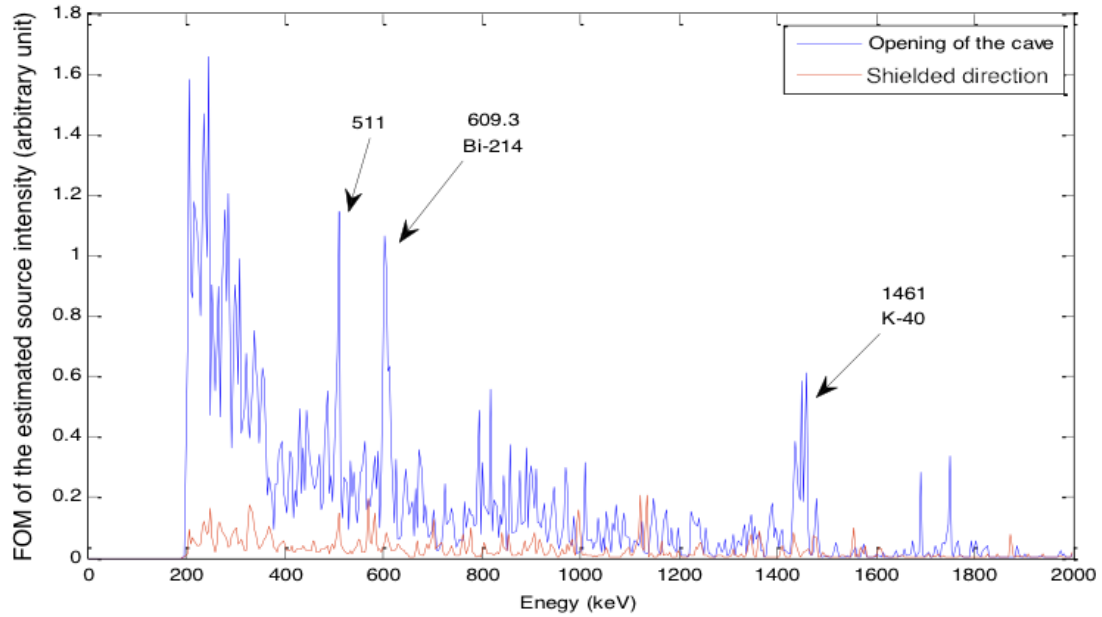
Figure 7.16: The deconvolved spectrum of a 30-degree half-angle region in one of the openings of the lead tunnel and the cathode direction which is blocked by 5 cm of lead. The y axis is the figure of merit of the source intensity.

7.3   Image a Bottle of K-Salt

Lite Salt is a trademarked salt alternative that has a lighter or smaller sodium content than regular salt. It contains a blend of regular salt and potassium chloride, according to Morton Salt [66; 67]. Lite Salt is sometimes used by people who want less sodium intake. K-40 produces 1462-keV gamma rays with an emission probability around 10%. We once used several bottles of Lite Salt to check the calibration of our detector when no check source was available. K-40 exists in both Lite Salt and concrete, so without the prior knowledge of the background level, a spectrometer can not determine if there is concentrated K-40 sources in a room.

A bottle of Morton Lite Salt™ which contains 311 gram of mixed salt was placed near the anode side of an array of two large CdZnTe detectors. The source was measured for about 8 hours due to extremely low activity of the salt and the background.

Around 33% of the recorded 1462 keV photons are from the salt. Figure 7.17 shows the raw recorded spectrum.
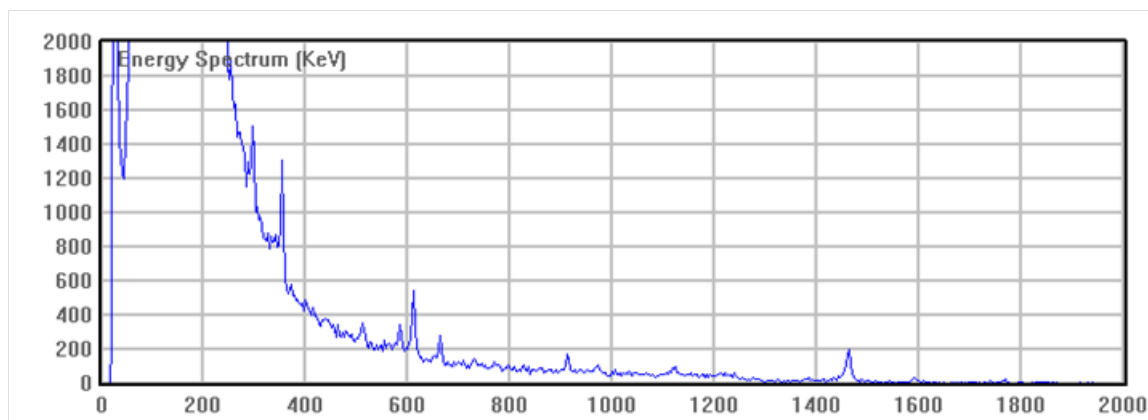
Figure 7.17: The raw recorded spectrum from the K-salt and the natural radiation background. Note the 1462 keV photopeak from K-40 is smaller than 609 keV photopeak from Bi-214.

After the MLEM deconvolution in combined spatial and energy domain, figure 7.18 can be achieved. A concentrated hotspot in the anode direction is located in the energy bin from 1460 keV to 1464 keV in the deconvolved image. This localized image indicates the presence of a concentrated source instead of the distributed natural background. The deconvolved spectrum in the cathode direction, shown as figure 7.19, shows that the 1462 keV photopeak has the same level of radiation compared to other background energy lines. Figure 7.20 shows that the deconvolved incident spectrum in the K-salt direction has a 1462 keV energy line dominating over all other background energy lines.

An interesting note of this experiment is that there is a faint yellow dot in 660 keV to 664 keV energy bin in the deconvolved image (figure 7.18). We followed the direction shown in the image. A Cs-137 source was found behind a concrete wall in the next room.
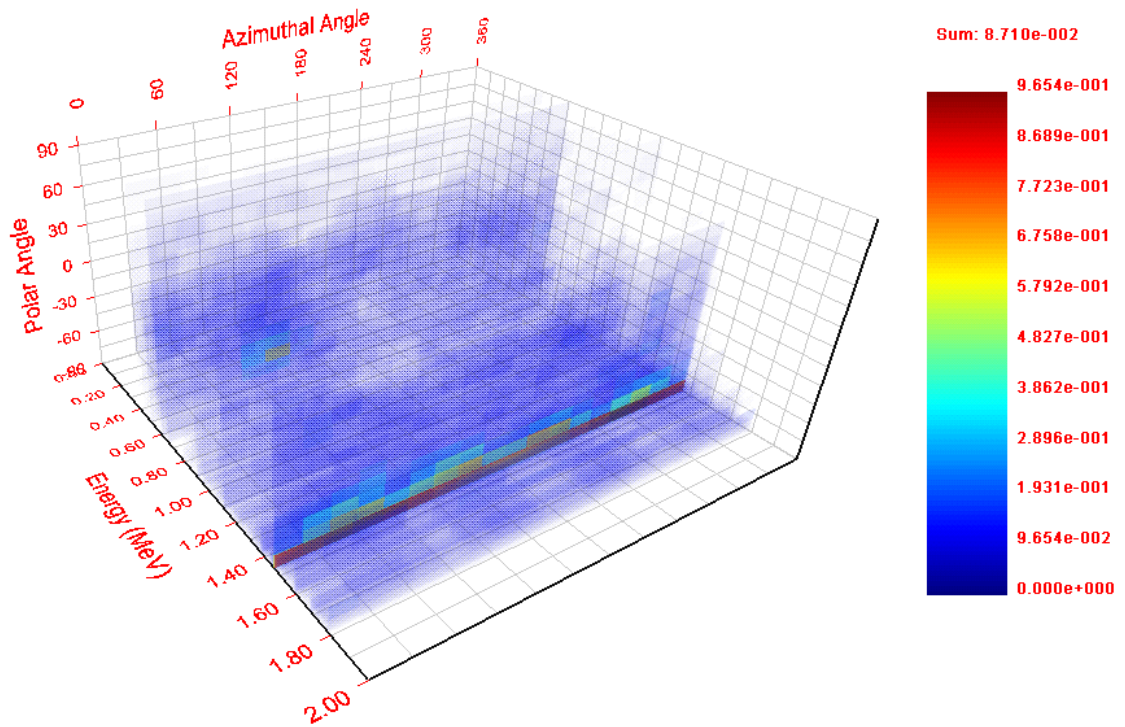
Figure 7.18: The deconvolved image from the K-salt measurement using MLEM method.
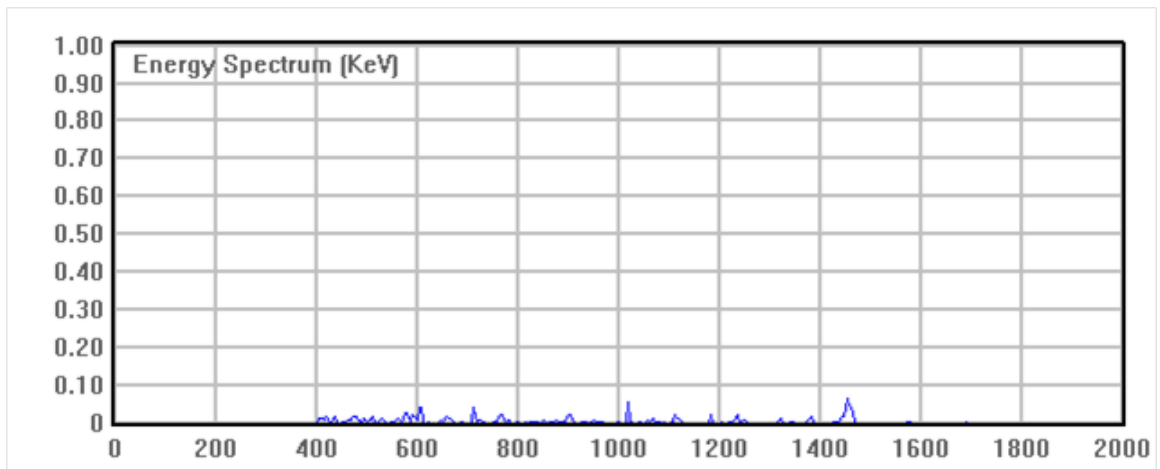
Figure 7.19: The deconvolved incoming spectrum in the direction which does not have the bottle of K-salt.
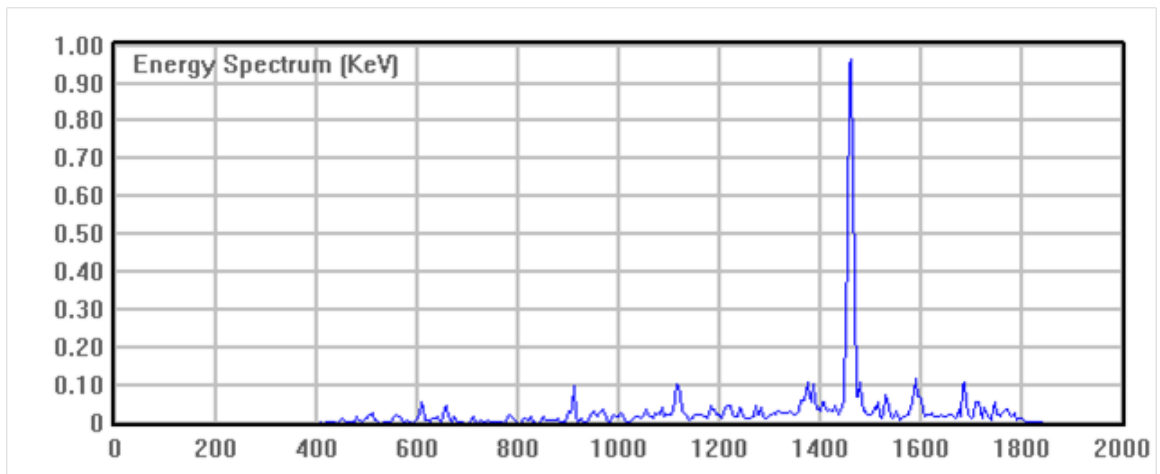
Figure 7.20: The deconvolved incoming spectrum in the direction of K-salt.

CHAPTER VIII

Imaging Sources with Known Motion

Radiation sources are not always stationary relative to the detector. For example, for homeland security applications, it is desired to image or detect sources in a moving vehicle [9; 68] or with a pedestrian. Multiple sources with different motion may present at the same time. Without motion compensation, the moving source will create a blurred image with a shape from the track of the motion. Figure 8.3 shows a reconstructed SBP image from a moving point source without motion compensation. The details of this experiment will be discussed in the following sections. If we have knowledge of the target motion as a function of time from an optical tracking system [69; 70; 71] and the time-stamp of each recorded event, source motion can be compensated. A similar problem has been studied for compensating respiratory motion in PET image reconstruction [72; 73; 74].

This work focuses on two ways of compensating the known motion of the tracked targets. The first is to rotate the entire image reference frame that follows the location of the target, so the target stays stationary in the image reference frame. The second is accumulating the reconstructed image intensity at the target direction for each time stamp in a separate target image bin. Both methods can be applied to SBP and MLEM reconstructions.

8.1 Experimental Setup

An 18-detector array was used in this experiment. Sources with known motion as a function of time are required for the presented algorithms. Figure 8.1 shows a picture of the apparatus that rotated a source around the detector array. A computer controlled actuator was mounted at the top of a table and was set to rotate the L-shaped arm with a constant angular velocity. A source was attached to the bottom of the L-shaped aluminum arm, where is in the plane of the detector array. The center of the detector array was placed directly under the pivot point of the actuator. In this experimental setup, the source can revolve around the center of the detector array 360 degrees.
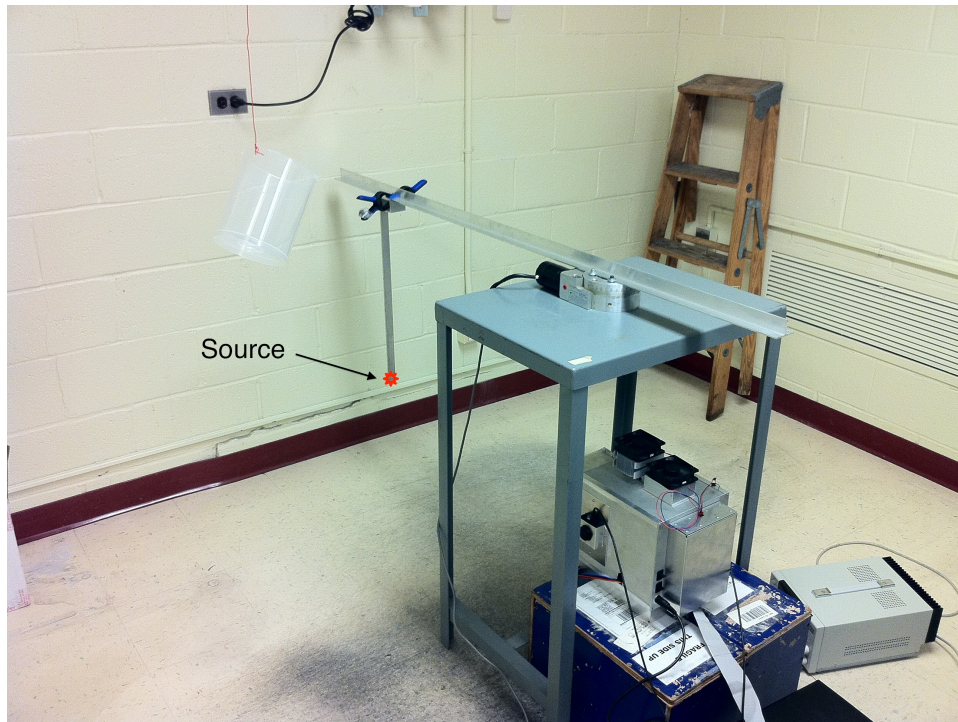
Figure 8.1: The experimental setup.

Two sources were measured separately. A 30-μCi Cs-137 source was measured while revolving around the detector 360 degrees counterclockwise. A 30-μCi Na-22 source was measured while revolving around the detector 360 degrees clockwise. The

two recorded event data sets were mixed together to create a scenario with two sources with different motion. This mixed data set is used to demonstrate different motion compensation methods throughout this chapter.
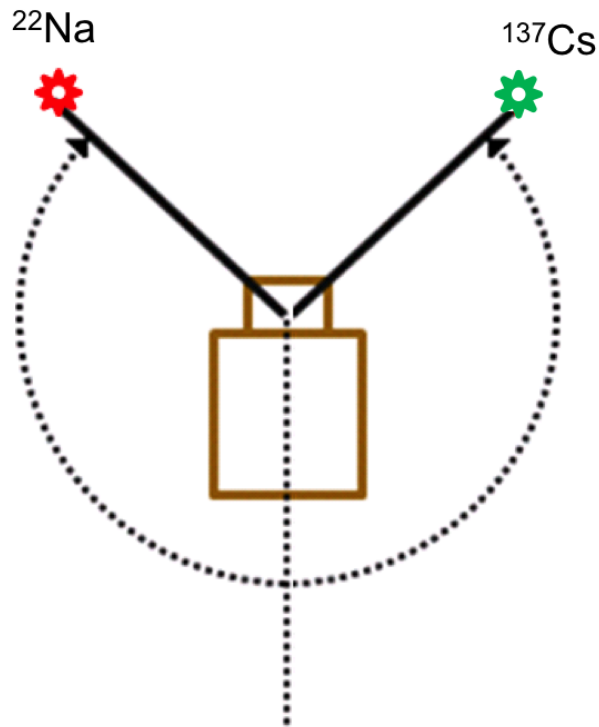
Figure 8.2: The illustration of a Cs-137 source and a Na-22 source rotating 360 degrees around the 18-detector array in different directions.[75]

8.2   Reference Frame Rotation Method

The reason of reconstructing a blurred uncompensated image, shown as figure 8.3, is that the source moves relative to the detector, illustrated in figure 8.4[1]. The most straightforward method to compensate the relative source motion is to rotate the image reference frame so the tracked target always keeps stationary relative to the detector as illustrated in figure 8.5[2].

---

[1]Image from Jason Jaworski, University of Michigan, Ann Arbor.
[2]Image from Jason Jaworski, University of Michigan, Ann Arbor.

Since the two sources in this experiment have different motion, it is impossible to keep both sources stationary at the same time. So separate reconstructions have to be performed to follow each source. As a consequence, the reconstruction time varies linearly with the number of targets. Figure 8.6 and figure 8.7 can be reconstructed using the SBP method when the reference frame is rotated to follow the motion of the Cs-137 source and the Na-22 source, respectively. Point-like images are clearly shown when the source is tracked to be stationary in the image reference frame with less than 600 events. As expected, when the image reference frame follows the motion of the Cs-137 source, the Na-22 photopeak events make a blurred image due to the fact that the Na-22 is not stationary relative to the detecter array, and vice versa.
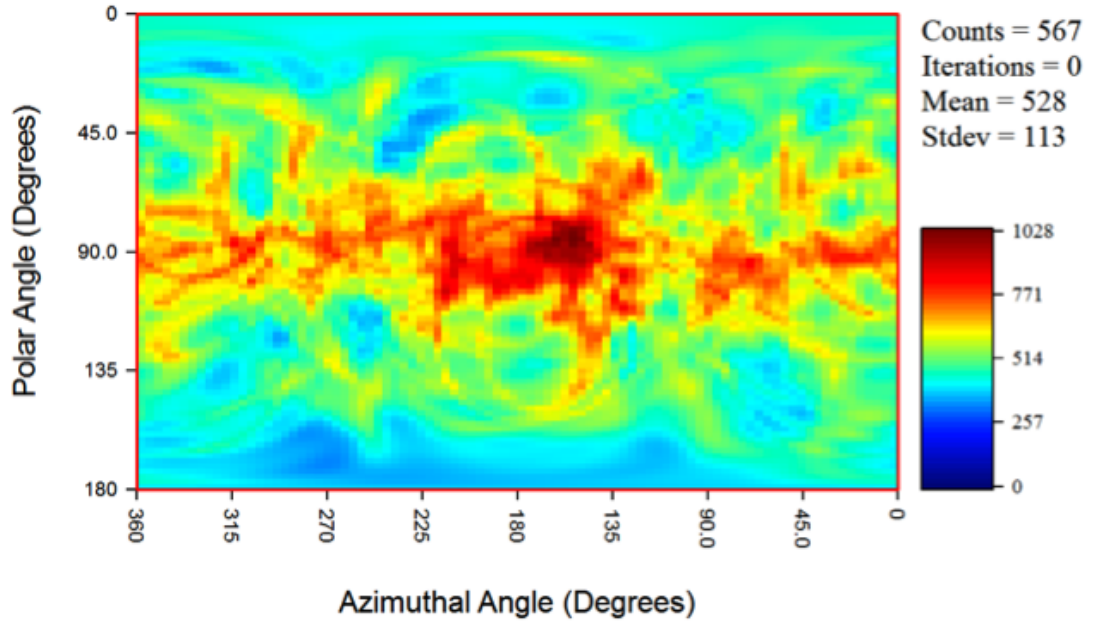
Figure 8.3: The SBP reconstructed image of a moving Cs-137 source in the Cs-137 photopeak energy window.

This reference frame rotation method can also be applied to the MLEM reconstruction. Instead of shifting the reconstructed Compton cone, the probability matrix shifts according to the direction of the target at the time of each event. From the
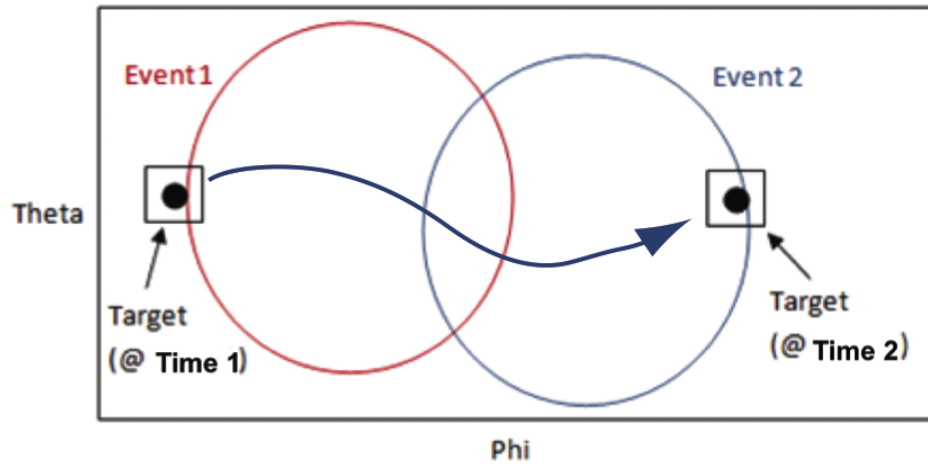
Figure 8.4: Illustration of Compton cones from a moving source at different time.
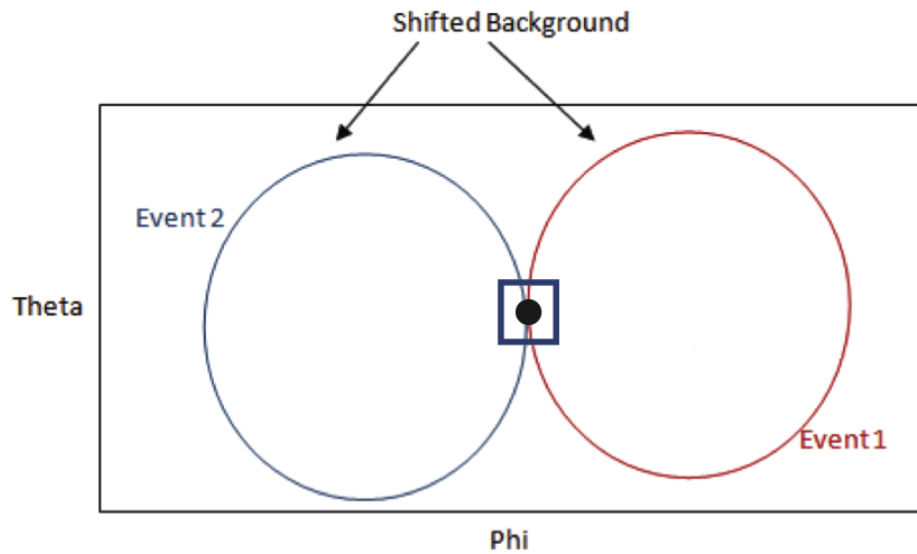
Figure 8.5: Illustration of Compton cones shifted according to the direction of the source at different times.

Counts = 567
Iterations = 0
Mean = 530
Stdev = 229

(a) Events in Cs-137 photopeak

Counts = 567
Iterations = 0
Mean = 528
Stdev = 129
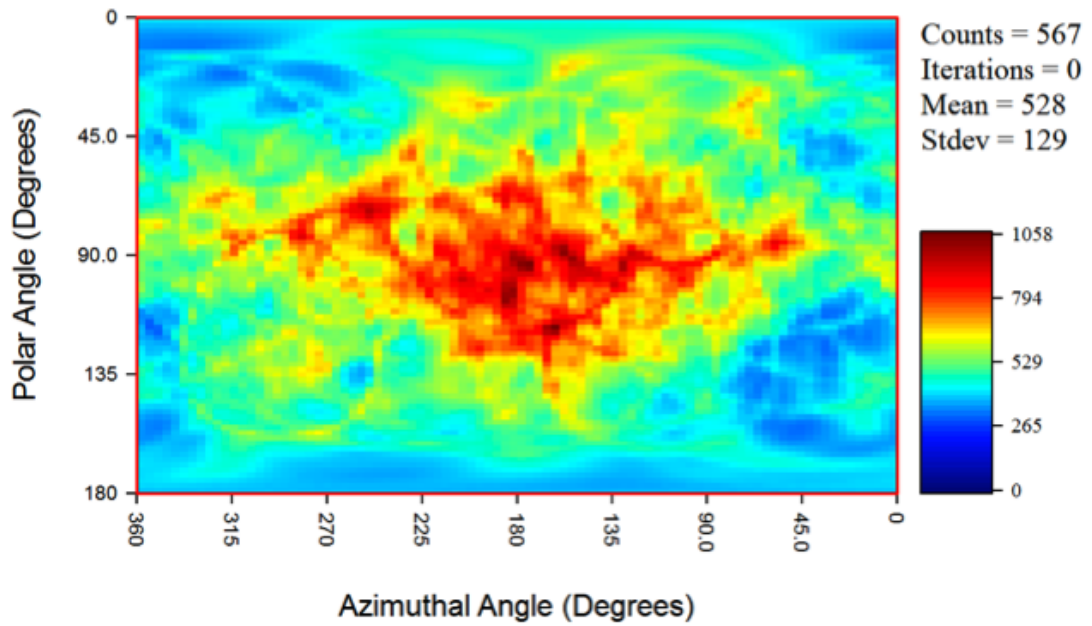
(b) Events in Na-22 photopeaks

Figure 8.6: The reconstructed image using SBP method with a rotated reference frame that follow the motion of the Cs-137 source.
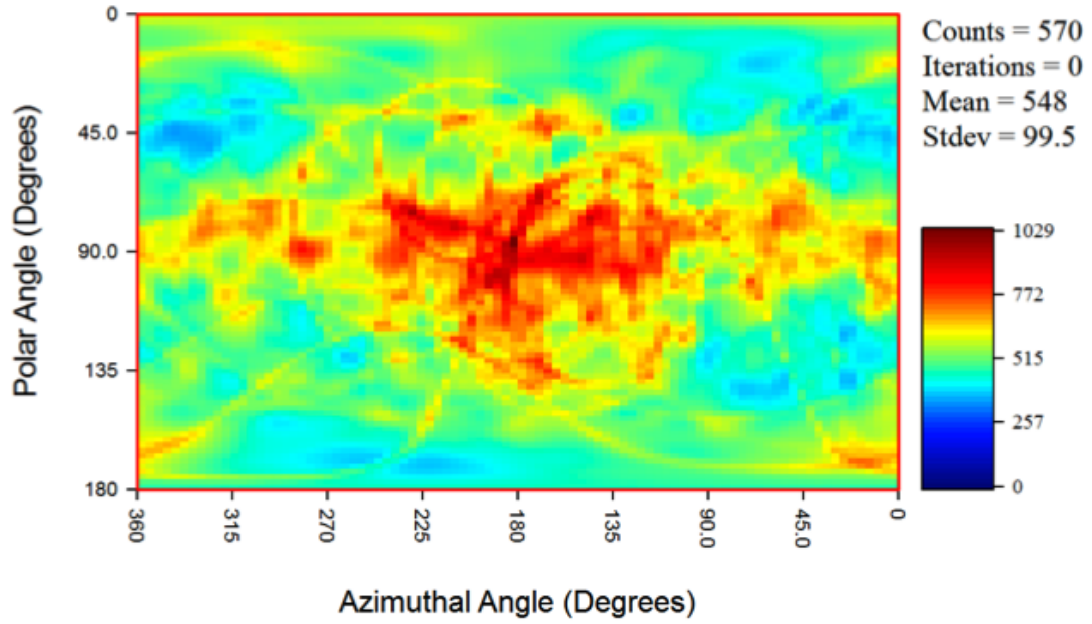
(a) Events in Cs-137 photopeak
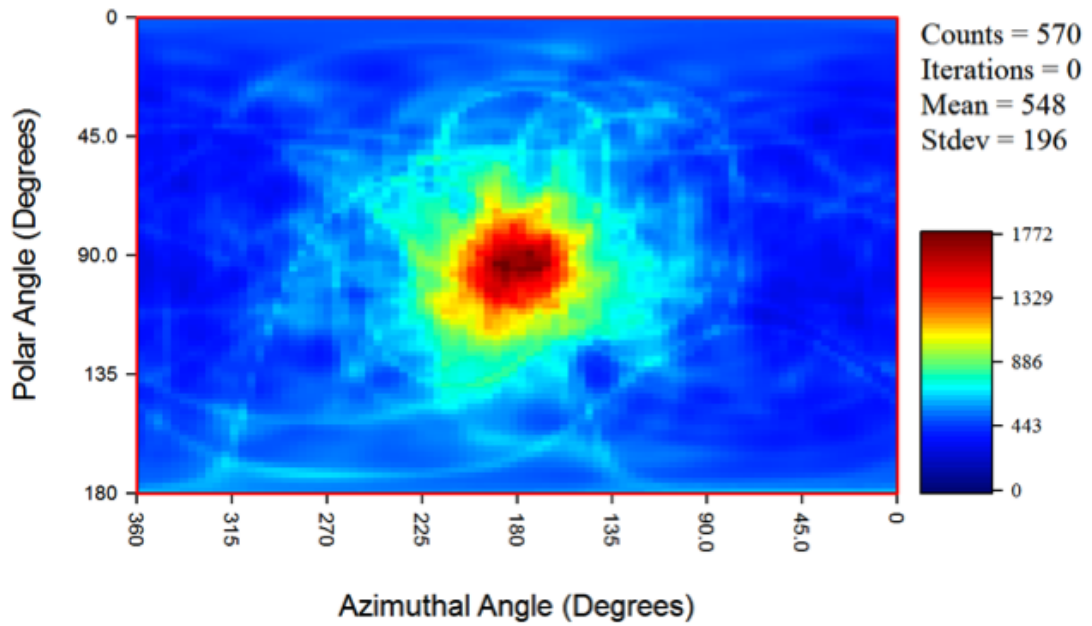
(b) Events in Na-22 photopeaks

Figure 8.7: The reconstructed image using the SBP method with a rotated reference frame that follows the motion of the Na-22 source.

detector's point of view, the target direction changes as a function of time. Since the sensitivity factor varies at different directions in our system, we need to include the change of the sensitivity factor in the list-mode EM solution (5.5). The new iterative list-mode EM solution

$$f_j^{n+1} = f_j^n \sum_{i=1}^{I} \frac{t_{ij}}{s_{ij} \sum_k t_{ik} f_k^n} \tag{8.1}$$

has a sensitivity term s_{ij} which is determined by the direction of the target at the time of event i.

Figure 8.8 and figure 8.9 show the results from MLEM deconvolution in spatial-only domain with 10 iterations with and without motion compensation, respectively, for events in the photopeak of the Cs-137 source. A nice sharp image was reconstructed by using the reference frame rotation method.
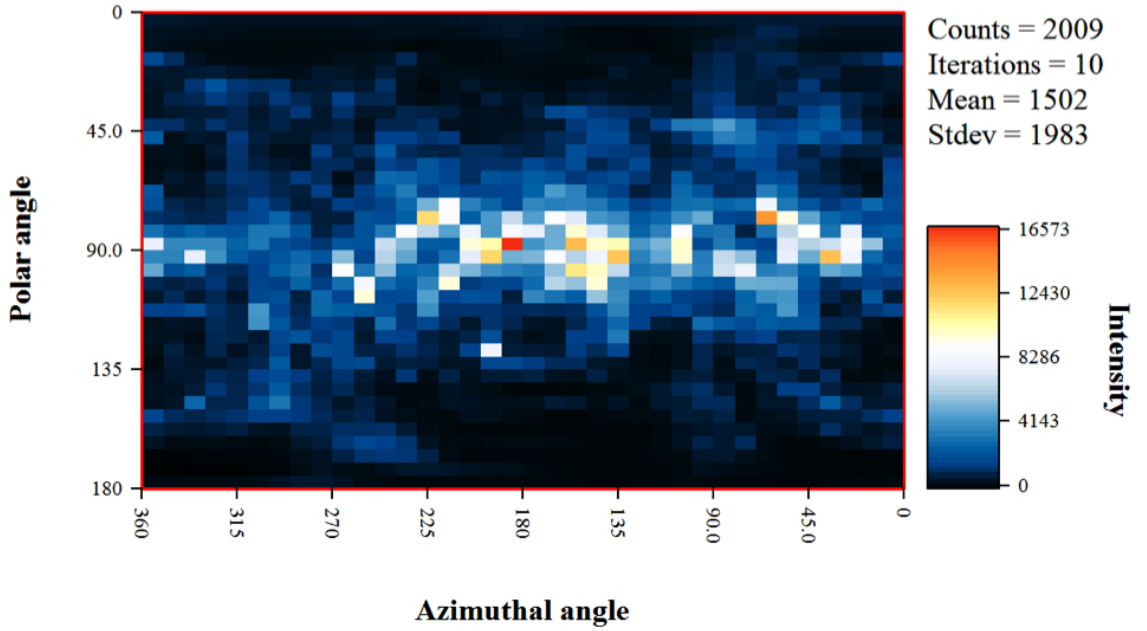
Figure 8.8: The reconstructed image using MLEM deconvolution in the spatial domain with 10 iterations without motion compensation.

Besides only capable of compensating one target motion at a time, another un-
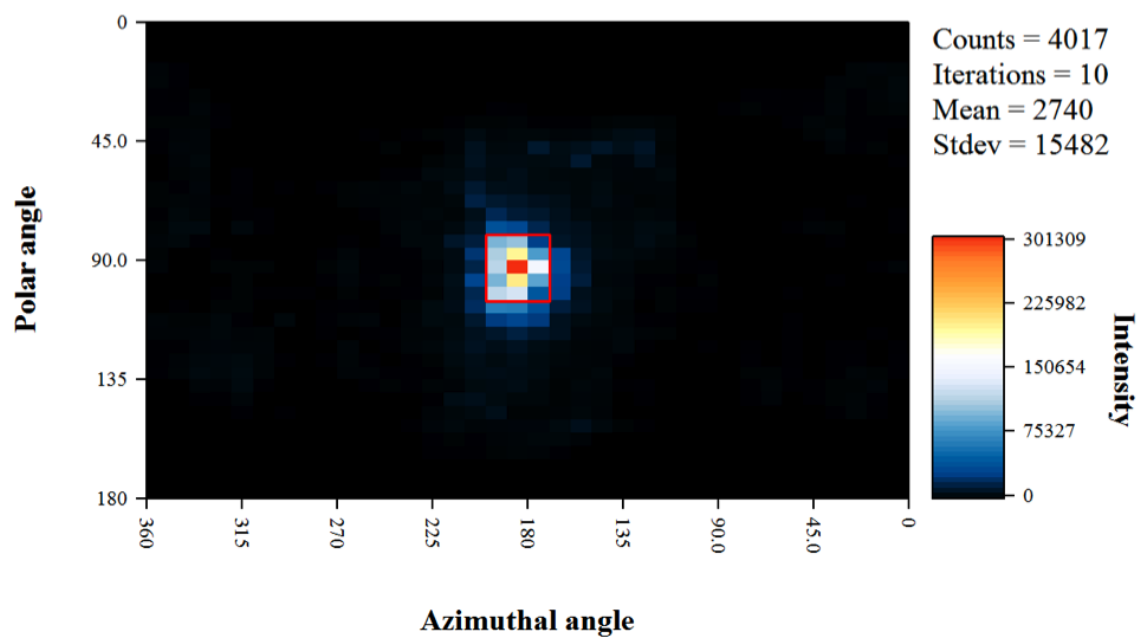
Figure 8.9: The reconstructed image using MLEM deconvolution in the spatial domain with 10 iterations with reference frame rotation motion compensation method.

avoidable problem of this reference frame rotation method is that the Compton cones produced by background events are rotated with the target as well. So the image from the stationary background is smeared when compensating the motion of a moving target.

8.3   Reconstruction with Additional Target Bins

In order to preserve the stationary background image while tracking a moving target, a series of target bins are created. One can "copy" the fraction of the reconstructed Compton cone according to the current location of each target and predefined target size, and then add the cone fraction to the corresponding target bin. This method is illustrated as figure 8.10[3]. The size of the target is a constant, and needs to be defined before the reconstruction. For the SBP algorithm, this method is much faster than the reference frame rotation method since summation is much faster to compute than rotating an image. The reconstructed image in the target bin can then be put back into the backdrop image following the current location of the source, so the radiation image can be overlaid with the image from the optical camera.

By adding the extra bins for targets to the image space, the MLEM reconstruction method described in chapter V becomes the MLEM deconvolution in the combined energy and direction-target domain, or energy-target integrated deconvolution (ETID). Figure 8.11 shows the structure of the new system matrix with the added row for each target. Similar to the MLEM deconvolution in the combined energy and spatial domain, ETID is capable of providing the source distribution in both backdrop and targets for each energy as well as the deconvolved incident spectrum, which is free of Compton continuum, in each target bin and every direction in the backdrop image. The theory, experimental results and analysis is described in detail by Jaworski et al. [76; 77].

---

[3]Image from Jason Jaworski, University of Michigan, Ann Arbor.
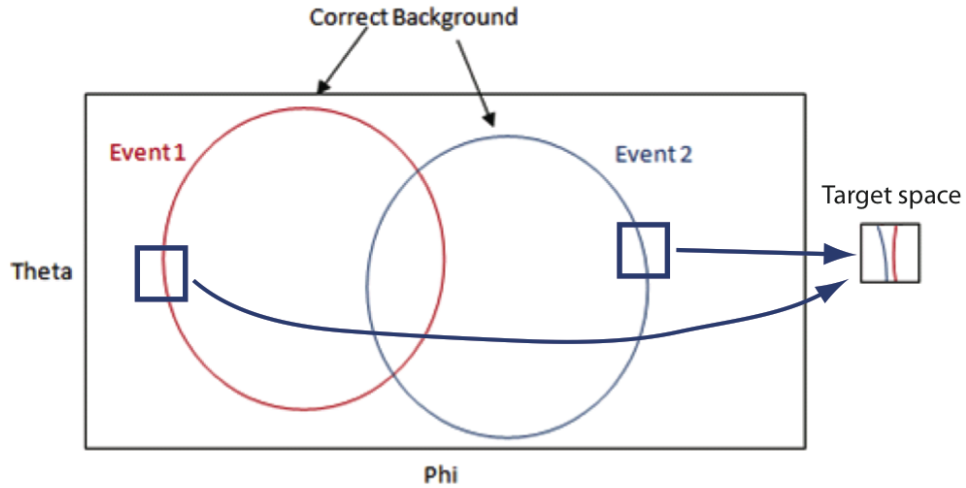
Figure 8.10: Illustration of motion compensation by adding the cone fraction to the target bin based on the direction and physical size of the target.

Compared to SBP with motion compensation which is capable of indicating the source direction with a mere 50 counts, ETID is more suited for situations where there are a sufficient amount of counts to achieve a statistically relevant source distribution estimation.
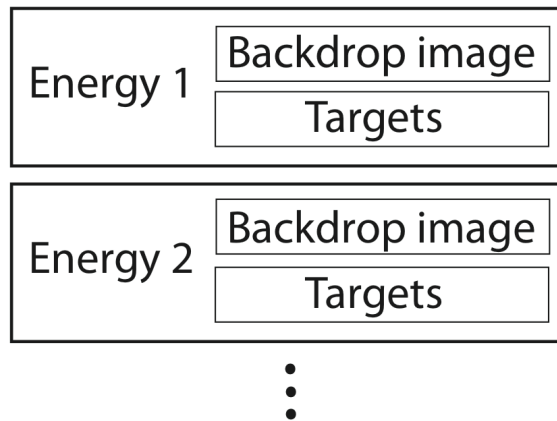
Figure 8.11: Rows are added for targets in the system matrix.

CHAPTER IX

Image Reconstruction with Sub-Pixel Position Resolution Events from a Digital ASIC

Several limitations of the analog system are listed in chapter 2.3. To overcome these limitations and to improve the lateral position resolution, and consequently the image angular resolution, a new digital ASIC was designed in a collaboration with Gamma-Medica Ideas. Instead of only reading out the amplitude of the peakhold signal after the shaping circuitry, the new digital readout system directly samples the waveform of the preamplifier signal. By analyzing the digitized waveform signals, event classification [78] and sub-pixel position sensing [79; 80] can be achieved.

This chapter first introduces the digital system and sub-pixel position sensing algorithm. A method is then proposed to correct the shift of cone axes due to the deviation between the centroid of the electron cloud and the true interaction location. To evaluate this new method SBP reconstructions are performed with simulated data and experimental data.

9.1 The Digital ASIC and Sub-Pixel Position Sensing

The digital ASIC samples the preamplifier signal at a rate of 80 MHz. It can also be operated at lower sampling rates of 40 MHz, 20 MHz and 10 MHz, which is useful

for detector materials that have longer charge collection time. The performance of this ASIC is discussed in detail by Zhu [81]. One example of the advantages of this digital ASIC is that it can reconstruct multiple interactions which occur under the same pixel. Figure 9.1[1] shows a comparison between shaped pixel waveforms from the analog ASIC and the sampled waveforms from the digital ASIC for the case of two interactions under the same pixel. Since the traditional analog system can only readout the maximum amplitude of the shaped signal, interactions under the same pixel will be output as a single interaction with the total energy, shown as the cyan curve in figure 9.1. With the digital ASIC, two rises shown as the green curve in figure 9.1, corresponding to the collection of two electron clouds, can be see in the sampled waveform from the collecting pixel. They can be used to reconstruct the energy and position of each interaction.
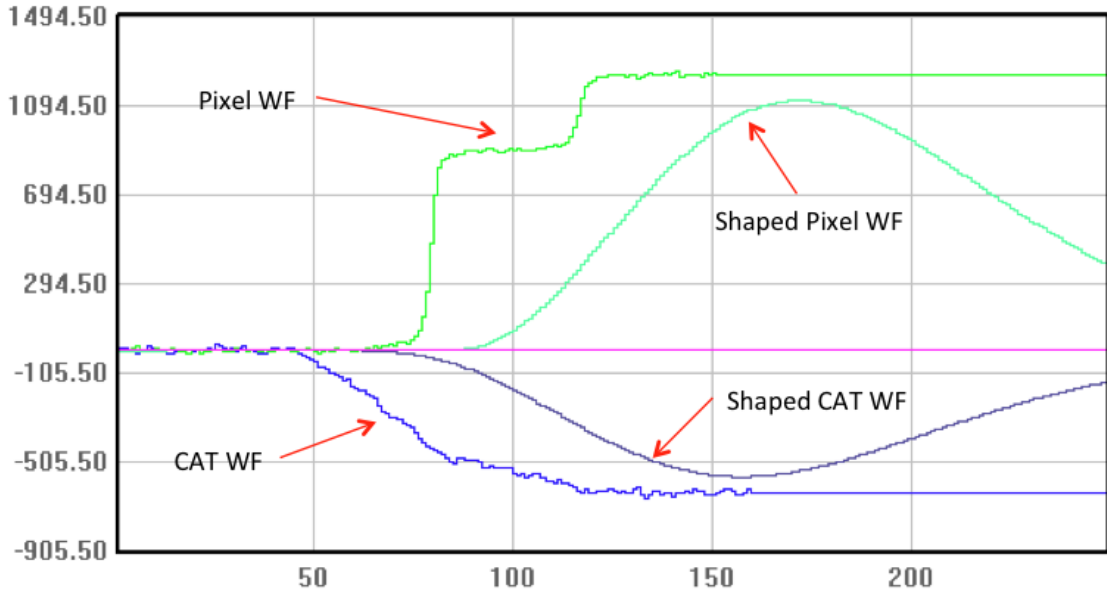
Figure 9.1: The comparison between shaped signal from the analog system and the sampled wave form from digital system for a event with two interactions under the same pixel.

Transient signals are induced on the neighbor pixels when electrons drift towards

---

[1]Image from Hao Yang, University of Michigan, Ann Arbor.

the collecting anode pixel. The amplitude of the transient signals on the neighbor pixels is sensitive to the lateral interaction location. It can be used to estimate the sub-pixel centroid position of an electron cloud. This so-called opposing-neighbor ratio method [80] is described as

$$P_x = \frac{S_{x1} - S_{x2}}{S_{x1} + S_{x2}} \tag{9.1}$$

$$P_y = \frac{S_{y1} - S_{y2}}{S_{y1} + S_{y2}} \tag{9.2}$$

in which P_x and P_y are the estimated sub-pixel centroid positions of an electron cloud in x and y directions, respectively, S_{x1} and S_{x2} are the induced signal amplitudes on the two neighbor pixels in x direction, and S_{y1} and S_{y2} are the induced signal amplitudes on the two neighbor pixels in y direction. Experiments have shown that the lateral sub-pixel position resolution for 662 keV in a 2-cm $\times$ 2-cm $\times$ 1.5-cm CdZnTe detector is about 300 μm FWHM [80].

Since the sub-pixel position resolution is inversely proportional to the energy deposition E [81], and the sub-pixel position uncertainty is about 0.3 mm FWHM at 662 keV, we can estimate the sub-pixel position resolution $p(E)$ at energy E as

$$p(E) \approx \frac{662keV}{E} \times 0.3mm \tag{9.3}$$

If the estimated position uncertainty $p(E)$ is larger than half of the pixel pitch, the reconstructed location is set to the center of the pixel. If the reconstructed sub-pixel interaction position is on the outside of the collecting pixel, the interaction location is set to the closest edge of the collecting pixel from the reconstructed position.

9.2 Back Projection with Sub-Pixel Data

9.2.1 Including the Recoil Electron in Back-Projection Cone Calculation

When a gamma ray Compton scatters with the detector material, part of the gamma ray's energy is transferred to a scattering electron which recoils and is ejected from its atom. This recoil electron travels a short distance in the detector before losing all of its energy and creating a cloud of ionizing electron-hole pairs along its path. The reconstructed interaction position is a measurement of the centroid of the ionizing electron cloud as opposed to the the actual Compton scattering location which is at the starting point of the recoil electron track. Figure 9.2[2] shows the simulation result of the average distance between the true Compton scattering location and the centroid of the electron cloud. When the energy deposition from Compton scattering is less than 2 MeV the distance between the centroid of the electron cloud and the true interaction location is much smaller than the lateral position uncertainty of a pixelated data set, which is limited by the pixel size of 1.72 mm. Therefore, the difference between the true and the measured Compton interation locations can be ignored when reconstructing source image with the pixelated data. With the digital ASIC the lateral sub-pixel position resolution is comparable to the size of the electron cloud, so the difference between the true and the measured Compton interaction locations need to be considered in the image reconstruction.

Figure 9.3 shows a gamma ray, γ, has forward scattered in the detector at location (x_1, y_1, z_1) with a scatter angle $\theta < \pi/2$. The scattered photon, γ', lost all of its energy in a photoelectric interaction at location (x_2, y_2, z_2). The recoil electron, e^-, from the Compton scatter has an angle of $\phi < \pi/2$ relative to the incident angle of the gamma ray γ. The measured location of the Compton scattering is determined by the centroid of the recoil electron cloud at a location (x_1', y_1', z_1'). Therefore, the measured location

---

[2]Image from Yuefeng Zhu, University of Michigan, Ann Arbor.
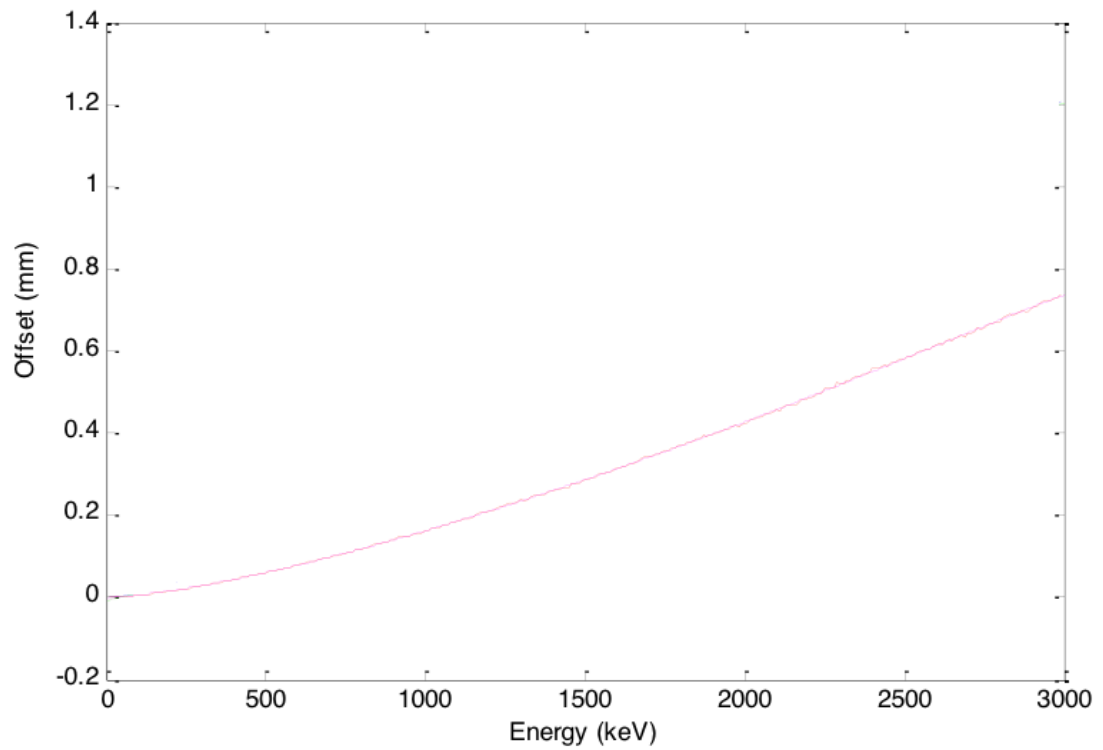
Figure 9.2: The distance between the centroid of the recoil electron cloud and the true interaction location as a function of energy deposition of the Compton scattering. The electron cloud is simulated with Geant 4 simulation software.

(x_1', y_1', z_1') is systematically biased by an angle ϕ and a distance l. By using the measured interaction locations, the blue cone can be reconstructed. This cone does not pass the incident direction because the cone axis was biased by angle δ. Due to the conservation of the momentum, the recoil electron has to be in the same plane with the incident direction of γ and the scattered direction of γ', and on the opposite side of the incident direction of γ from γ'. In order for the back-project cone to pass through the incident gamma ray direction, the scatter angle needs to be increased by δ, as illustrated by the red cone in figure 9.3.
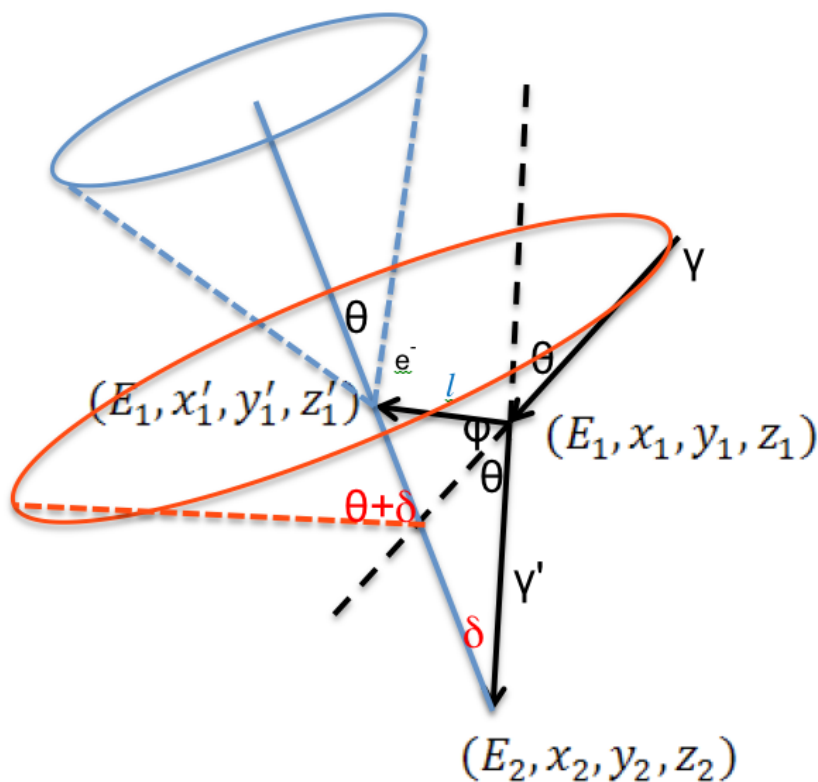
Figure 9.3: The scatter angle needs to be increased by angle δ in the forward-scatter case so the back-project cone passes the incident direction.

When a gamma ray backward scatters in the detector, both the photon scattering angle, θ, and the recoil electron angle, ϕ, are obtuse angles. Figure 9.4 shows a illustration of this backward-scatter scenario. θ' and ϕ' are the supplementary angles of θ and ϕ, respectively. It can be seen in figure 9.4 that in order to make the blue

back-projection cone passes through the source direction, the half angle, θ', has to be increased by the bias angle of the cone axis, δ. As a consequence, the back-projection cone angle θ needs to be decreased by δ.

Figure 9.4: The scatter angle needs to be decreased by angle δ in the back-scatter case so the back-project cone passes the incident direction.

Now we need to solve angle δ in the triangle illustrated in figure 9.5. In this figure, α is the acute angle between the incident photon direction and the scattered photon direction, and β is the acute angle between the incident photon direction and the recoil electron direction. So for the forward scatter case, $\alpha = \theta$ and $\beta = \phi$, and for the backward scatter case, $\alpha = \pi - \theta$ and $\beta = \pi - \phi$. From the conservation of energy and momentum, and the energy-momentum relation for a photon and an electron, we have

$$E_\gamma + m_e c^2 = E_e + E_{\gamma'} \tag{9.4}$$

$$\mathbf{P}_\gamma = \mathbf{P}_e + \mathbf{P}_{\gamma'} \tag{9.5}$$

$$E_\gamma = |\mathbf{P}_\gamma| c \tag{9.6}$$

$$E_{\gamma'} = |\mathbf{P}_{\gamma'}|c \tag{9.7}$$

$$E_e^2 = m_e^2 c^4 + |\mathbf{P}_e|^2 c^2 \tag{9.8}$$

where E_γ and $\mathbf{P}_\gamma$ are the energy and the momentum of the photon before Compton scattering, $E_{\gamma'}$ and $\mathbf{P}_{\gamma'}$ are the energy and the momentum of the scattered photon, E_e and $\mathbf{P}_e$ are the energy and the momentum of the recoil electron, $m_e c^2$ is the rest mass energy of an electron, and c is the speed of light. By combining equations (9.4), (9.5), (9.6), (9.7), (9.8), the acute angle between the recoil electron and the incident photon direction, β, can be derived as

$$\beta = \sin^{-1}\left(\frac{E_{\gamma'}\sin\alpha}{\sqrt{E_e^2 - m_e^2 c^4}}\right) = sin^{-1}\left(\frac{E_2 \sin\alpha}{\sqrt{E_1^2 + 2m_e c^2}}\right) \tag{9.9}$$

From the law of sines, we have

$$\frac{d}{\sin(\alpha + \beta)} = \frac{l}{\sin\delta} \tag{9.10}$$

in which, l is a function of energy E_1 as shown in figure 9.2, and d is the separation distance between two measured interaction locations. δ has two solutions from equation (9.10): one below $\pi/2$, one above $\pi/2$. However, for events with an energy lower than 2 MeV, l is on the order of magnitude of 100 μm, and the average separation distance between the measured interactions, d, is about several millimeter. Therefore, $d > l$ and δ is the acute angle solution from equation (9.10).

9.2.2 Compton Cone Width

Due to the imperfect detector response and measurement uncertainty, only a small portion of the back-projection cones pass the source direction. In the real world application, in order to make the limited number of reconstructed cones intersect with each other, a Gaussian-shaped cone width determined based on the angular
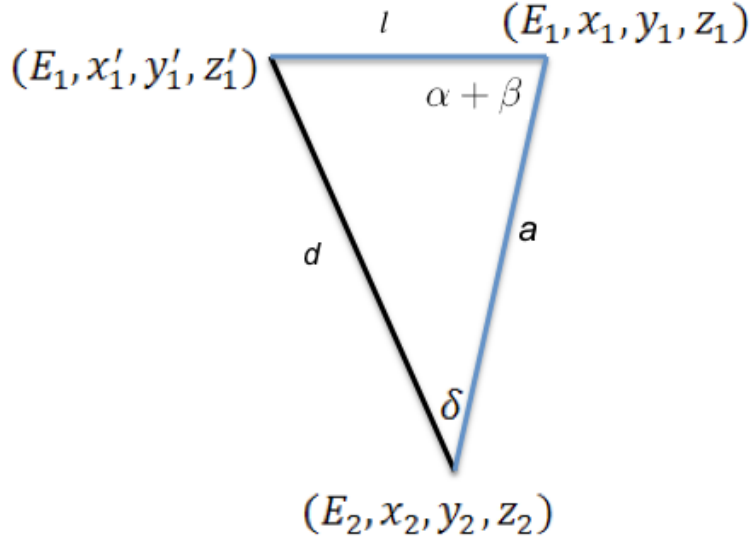
Figure 9.5: The triangle with vertices of true Compton interaction location (x_1, y_1, z_1), measured second interaction location (x_2, y_2, z_2) and measured centroid of the electron cloud (x_1', y_1', z_1').

uncertainty of each event is added to each back-projection cone. By propagating errors for equation (3.3) and (3.4), the cone axis uncertainties in the ϕ and θ directions from the interaction position uncertainties can be achieved as

$$\sigma_\phi^2 = \frac{p_1^2 + p_2^2}{(x_2 - x_1)^2 + (y_2 - y_1)^2} \tag{9.11}$$

$$\sigma_\theta^2 = \frac{(z_2 - z_1)^2(p_1^2 + p_2^2) + 2[(x_2 - x_1)^2 + (y_2 - y_1)^2](\sigma_z)^2}{[(x_2 - x_1)^2 + (y_2 - y_1)^2 + (z_2 - z_1)^2]^2} \tag{9.12}$$

in which, p_1 and p_2 are the sub-pixel position uncertainties of two interactions and σ_z is the depth uncertainty.

When one measures and compares the angular resolution between different algorithms, adding an artificial cone width will over-estimate the angular uncertainty. In the following section, a Gaussian shape cone width with a standard deviation of 0.005 radian was assigned to all back-projection cones.

9.3 Performance

9.3.1 Simulation

Geant 4 was used to simulate the electron cloud. The cloud data was then processed to produce the pixelated data and the sub-pixel position resolution data. All three images in figure 9.6 were reconstructed using the SBP algorithm from a simulated 1460 keV point source. Figure 9.6(a) was reconstructed using the pixelated data. Figure 9.6(b) was reconstructed using the sub-pixel resolution data without performing the recoil electron correction. Figure 9.6(c) was reconstructed using the sub-pixel resolution data with the recoil electron correction. By using the sub-pixel resolution data, the angular resolution was improved by 6.9 degrees in the polar direction and 7.8 degrees in the azimuthal direction compared to the image from the pixelated data. By performing the recoil electron correction, the angular resolution was further improved by 3.6 degrees and 1.4 degrees in the polar and azimuthal direction, respectively.

In figure 9.6(a), two curved vertical lines can be seen on the left and right edges of the hot spot. This is produced from binning interactions into 121 pixels. In the pixelated data, all interactions under the same pixel have the same lateral position as the centroid of the collecting pixel. When sub-pixel resolution data is used, the lateral locations of interactions become much more continuous. As a consequence, this "pixel binning artifact" is eliminated in figure 9.6(b) and 9.6(c). This artifact was never observed before because it was blurred by the added cone width. This effect is consistent with the measurement which will be described in section 9.3.2.

9.3.2 Measurement

A 1-μCi Co-60 source was measured at about 14 cm away from the detector. Three images in figure 9.7 were reconstructed by using the SBP algorithm. Figure 9.7(a)

126
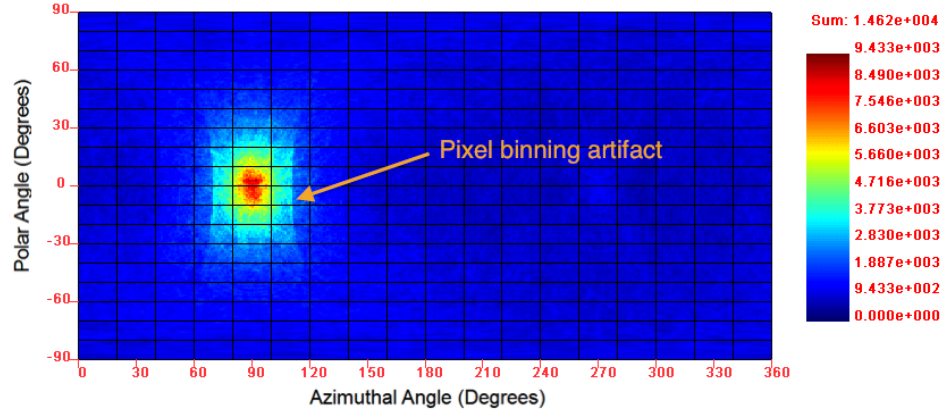
(a) Pixelated data. The polar and azimuthal angular resolution is 31.7 degrees and 23.6 degrees, respectively.
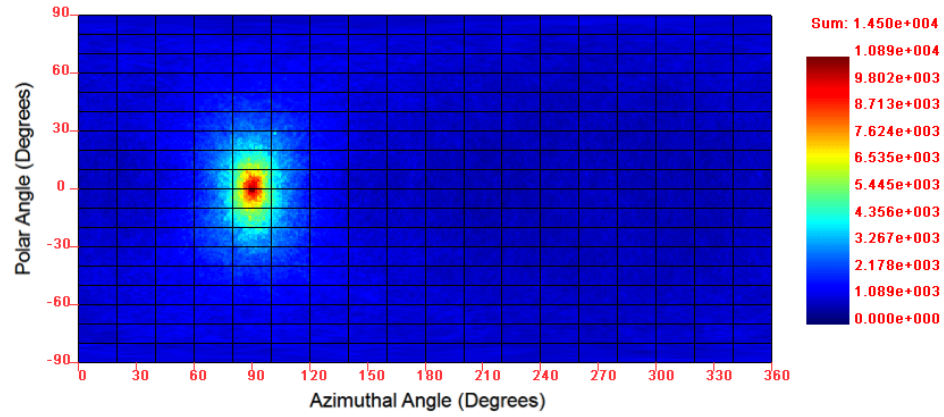
(b) Sub-pixel data without recoil electron correction. The polar and azimuthal angular resolution is 24.8 degrees and 15.8 degrees, respectively.
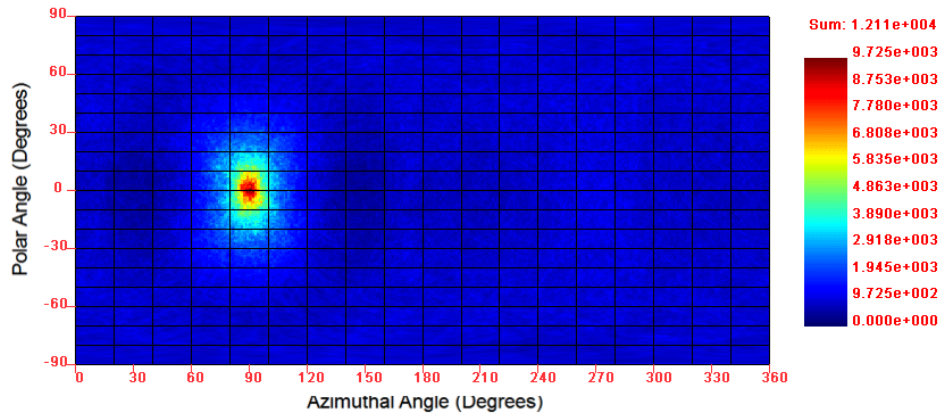
(c) Sub-pixel data with recoil electron correction. The polar and azimuthal angular resolution is 21.2 degrees and 14.4 degrees, respectively.

Figure 9.6: The SBP image from a set of pixelated data produced by a simulated 1462 keV source. The energy windows is from 1400 keV to 1500 keV.

was reconstructed using the pixelated data. Figure 9.7(b) was reconstructed using the sub-pixel resolution data without performing the recoil electron correction. Figure 9.7(c) was reconstructed using the sub-pixel resolution data with the recoil electron correction. By using the sub-pixel resolution data, the angular resolution was improved by 3.6 degrees in the polar direction and 6.5 degrees in the azimuthal direction compared to the image from the pixelated data. By performing the recoil electron correction, the angular resolution was further improved by 3.9 degrees and 1.3 degrees in the polar and azimuthal direction, respectively. This result is consistent with the simulation.
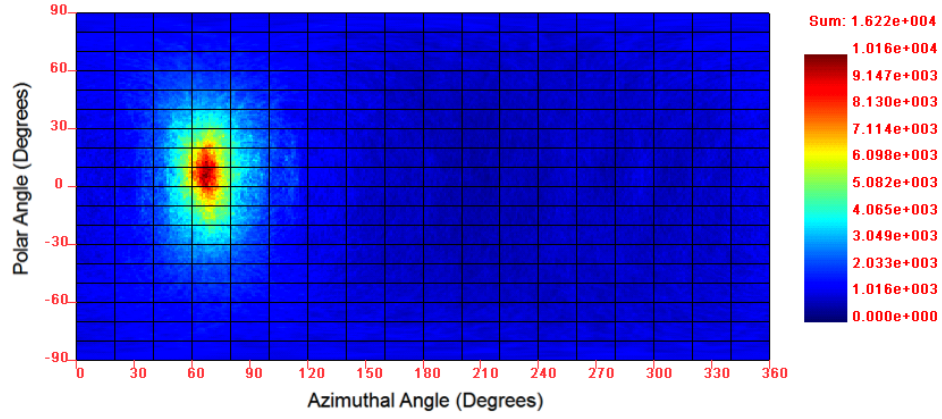
(a) Pixelated data. The polar and azimuthal angular resolution is 37.5 degrees and 23.1 degrees, respectively.
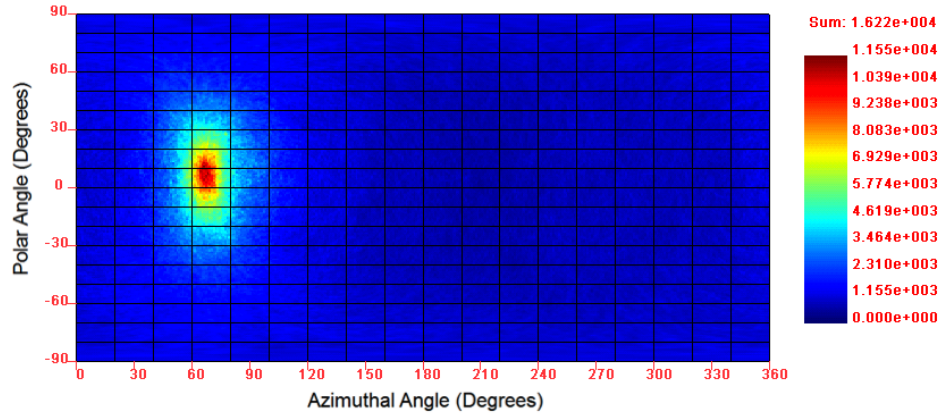
(b) Sub-pixel data without recoil electron correction. The polar and azimuthal angular resolution is 33.9 degrees and 16.6 degrees, respectively.
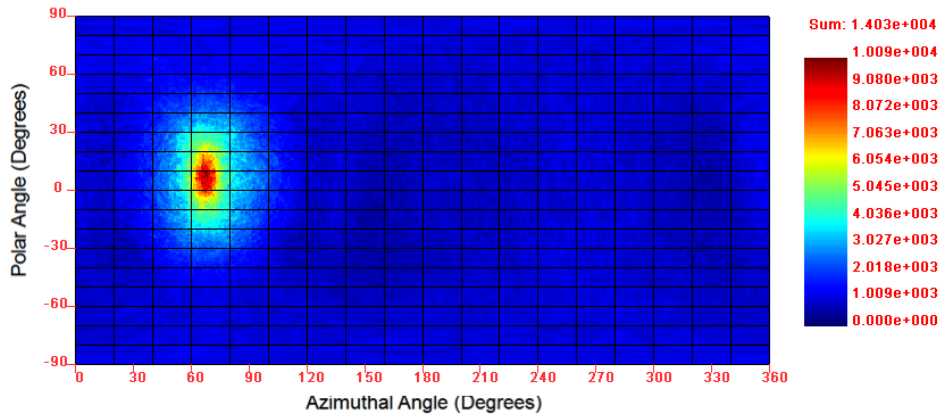
(c) Sub-pixel data with recoil electron correction. The polar and azimuthal angular resolution is 30.0 degrees and 15.3 degrees, respectively.

Figure 9.7: The SBP image from a measurement of a Co-60 source. The energy window is from 1150 keV to 1400 keV.

CHAPTER X

Summary and Suggestions for Future Work

10.1 Summary

Three-dimensional position-sensitive CdZnTe gamma ray detectors are capable of achieving excellent energy resolution (less than 0.7% FWHM for single-pixel events at 662 keV from the entire crystal volume of 6 cm^3) at room temperature. With this versatile detector technology, many types of imaging techniques and applications become possible. In some applications where real world directions are desired, an overlaid optical-radiation image can be achieved with some calibrations.

The system response function for three-dimensional position-sensitive gamma-ray detectors has been established as a function of both energy and direction; therefore, the deconvolved result shows the spatial distribution for each incident energy as well as the incident spectrum for each direction. This energy-imaging integrated deconvolution (EIID) algorithm was developed in our research group for two-interaction events from a single 1.5-cm × 1.5-cm × 1-cm position-sensitive-room-temperature CdZnTe detector. Because of the increased volume of individual CdZnTe detector modules and the new array configuration, the fraction of events with three or more interactions has increased. In order to make use of these events and improve imaging efficiency at higher energies, the analytical derivation of the system response function was extended to three-interaction events and further extrapolated to events with any

number of interactions. By including events with any number of interactions in the maximum-likelihood expectation-maximization deconvolution in the spatial as well as the combined spatial-energy domain, all events can be used in the reconstruction. In addition, these derivations are applied to an array system. The experimental results demonstrated that by using the newly derived system response functions, the deconvolved image from two-, three- and four-interaction events located the source direction, and that the deconvolved spectra were free of Compton continuum. By including three- and four-interaction events in the reconstruction, the imaging efficiency was more than doubled for a Co-60 source, and the angular FWHM was improved as well. This algorithm is not limited to CdZnTe detectors; it can be applied to any gamma-ray detector system that has the capability of providing the 3D interaction location and energy deposition for each interaction.

Prior analysis only considered non-charge-sharing two-interaction events in the Compton image reconstruction. With the correct depth reconstruction, many charge-sharing interactions can be classified as a single interaction and used for Compton image reconstruction. The three-pixel side-neighbor photopeak events from a simulation were divided into six categories based on interaction type. Analysis of this simulation shows that the most effective strategy is to treat all side-neighbor events as charge-sharing events and to combine all side-neighbor interactions into a single interaction. By including these side-neighbor events in the Compton image reconstruction, we can still correctly reconstruct the source distribution using experimental data and improve the imaging efficiency by about 45% and 160% for 662 keV and 1333 keV incident photons, respectively. About 76% of these combined events reconstruct to rings that pass the source direction.

Prior to this thesis work, the EIID imaging efficiency for a Co-60 measurement was about 5% of the raw events. By extending the system response function to events with any number of interactions and including side-neighbor events in the image

reconstruction, the EIID imaging efficiency has been increased to about 42% if only events with two or more interactions are used. If we include the single-interaction events in the reconstruction, almost 100% of the measured raw events can be used.

Since the EIID spectrum corrects for detector efficiency and includes raw events in the Compton continuum, the deconvolved incident spectrum of the source direction has the correct branching ratio. The accurate branching ratios allow for ease of isotope identification. Moreover, the source intensity can be estimated from the deconvolved spectrum after a single calibration. If the distance of the source is known and is combined with the identified isotope information, the activity of the source can be estimated. From the deconvolved image, the presence of shielding can be detected. The shielding can be further characterized as high-z or low-z material by comparing the peak areas in the deconvolved spectrum with the theoretical branching ratios.

We demonstrated that our detector and imaging algorithm are capable of reconstructing an extended area source. The distribution of the natural radiation background from the concrete wall in our laboratory was obtained using Compton imaging techniques with a single 2-cm $\times$ 2-cm $\times$ 1.5-cm CdZnTe detector when all laboratory sources were heavily shielded. The measurement time needed to obtain the distribution of the natural radiation background would be significant reduced if the new 18-detector array system was used. The ability to accurately visualize the natural background is verified by reconstructing a well defined background distribution using a lead tunnel. Moreover, a source sharing an energy line with the distributed background can be differentiated by observing a localized hot spot in the reconstructed image.

Source motion can cause blurry image reconstruction. In order to compensate for the known motion of a source, two methods are proposed. The first method rotates the imaging reference frame to track the movement of the source in order to keep the source stationary in the imaging reference frame. The second method is to expand

the imaging space with additional target bins. The fraction of the back-projection cone passing a target direction is then accumulated in the associated target bin. Both methods can be applied to SBP or MLEM deconvolution.

The new digital ASIC is capable of providing lateral sub-pixel interaction positions. For 662 keV the lateral sub-pixel position resolution is about 300 μm FWHM, which is on the same order of magnitude of the recoil electron cloud size. A geometry analysis suggests that in order to compensate image uncertainty introduced by the difference between the true Compton scattering location and the measured centroid of the recoil electron cloud, the back-projection cone angle needs to be increased in the forward-scattering case and decreased in the backward-scattering case. The change of the cone angle is also calculated from geometry information combined with conservation of energy and momentum. By using this method, appreciable improvement in the image angular resolution was shown with both simulated and experimental data.

10.2   Future Work

In the current implementation the image space is divided into a rectangular mesh. This is not the most computationally efficient mesh since the regions near poles of the imaging sphere (polar angles of 0 degrees and 180 degrees) are over-sampled. We might want to switch to image bins that have equal solid angle to reduce the computational load. In addition, the imaging mesh is a simple set of sampling points and if the mesh is coarse (i.e. few sample points), some cones may not be accurately represented or may not be reconstructed at all. This problem could be overcome by calculating the fraction of the cone that passes each pixel.

Pair production can occur when the incident photon has an energy exceeding twice of the rest energy of an electron. Two annihilation photons each with an energy of 511 keV are created in this process. Photons that undergo pair-production do not contain useful Compton scattering information and, therefore, should be excluded from the

Compton image. Because of limitations of the analog system, pair-production events are difficult to classify. Therefore, it would be useful to include the probability of pair production in the MLEM system model. Ideally, if pair production was included in the system model, the escape peaks would be correctly deconvolved in the incident spectrum.

In order to reconstruct the correct source distribution from single-pixel events and compensate for various model mismatches, a sensitivity image needs to be directly measured. It is nearly impossible to measure the detection probability in each directional and energy bin. But measuring a handful of energy lines for several unique directions and interpolating the detection probability for other directional and energy bins may be a practical solution.

To achieve a deconvolved image in a reasonable time, we neglected $f(D_1^c|\tilde{r}_1; E_0, r_0)$, $f(D_2^c|\tilde{E}_1, \tilde{r}_1, \tilde{r}_2, D_1^c; E_0, r_0)$, $f(D_3^p|\tilde{E}_1, \tilde{r}_1, \tilde{E}_2, \tilde{r}_2, \tilde{r}_3, D_1^c, D_2^c; E_0, r_0)$, and $f(D_3^c|\tilde{E}_1, \tilde{r}_1, \tilde{E}_2, \tilde{r}_2, \tilde{r}_3, D_1^c, D_2^c; E_0, r_0)$ in the system response function derivation in chapter V. These approximations are equivalent to assuming a uniform sensitivity image in system matrix calculation. As a result, the system matrix is weighted by the sensitivity image. Future work is needed to study how to pre-calculate these detection probabilities or compute these probabilities on the fly.

The scenarios of reconstructing a moving source and reconstructing a stationary source with a moving detector are equivalent in math. However, the three-dimensional source distribution can be mapped by the movement of a single detector. With the large number of the possible three-dimensional image bins, a dynamic binning algorithm needs to be developed so that the size of the image bins is adaptive to the reconstructed source intensity in that region. In addition, combining moving detector and moving source algorithms, the distributed detector sensor network concept can be realized.

BIBLIOGRAPHY

BIBLIOGRAPHY

[1] R. Fitzgerald, "Phase-sensitive x-ray imaging," vol. 53, no. 7, pp. 23–26, 2000.

[2] "http://en.wikipedia.org/wiki/x-ray_computed_tomography."

[3] G. Knoll, "Single-photon emission computed tomography," *Proceedings of the IEEE*, vol. 71, pp. 320 – 329, march 1983.

[4] M. W. Groch and W. D. Erwin, "Spect in the year 2000: Basic principles," *Journal of Nuclear Medicine Technology*, vol. 28, no. 4, pp. 233–244, 2000.

[5] M. M. Ter-Pogossian, M. E. Raichle, and B. E. Sobel, "Positron-emission tomography," *Scientific America*, 1980.

[6] J. M. Ollinger and J. A. Fessler, "Positron-emission tomography," *Signal Processing Magazine, IEEE*, vol. 14, pp. 43 –55, jan 1997.

[7] E. E. Fenimore and T. M. Cannon, "Coded aperture imaging with uniformly redundant arrays," *Appl. Opt.*, vol. 17, pp. 337–347, Feb 1978.

[8] S. J. Kaye, W. R. Kaye, J. M. Jaworski, and Z. He, "Experimental limitations of coded aperture imaging using thick 3d-position-sensitive CdZnTe detectors," in *Nuclear Science Symposium Conference Record (NSS/MIC), 2010 IEEE*, pp. 3856 –3859, 30 2010-nov. 6 2010.

[9] K. P. Ziock, J. Collins, M. Cunningham, L. Fabris, T. Gee, J. Goddard, F. Habte, and T. Karnowski, "The use of gamma-ray imaging to improve portal monitor performance," *Nuclear Science, IEEE Transactions on*, vol. 55, pp. 3654 –3664, dec. 2008.

[10] W. R. Kaye, N. D. Bennett, C. G. Wahl, Z. He, and W. Wang, "Gamma-ray source location by attenuation measurements," in *Nuclear Science Symposium Conference Record, 2007. NSS '07. IEEE*, vol. 2, pp. 1294 –1298, 26 2007-nov. 3 2007.

[11] D. Xu, *Gamma-ray imaging and polarization measurement using 3-D position-sensitive CdZnTe detectors*. PhD thesis, University of Michigan, 2006.

[12] V. Schönfelder, A. Hirner, and K. Schneider, "A telescope for soft gamma ray astronomy," *Nuclear Instruments and Methods*, vol. 107, no. 2, pp. 385 – 394, 1973.

[13] M. Singh, "An electronically collimated gamma camera for single photon emission computed tomography. part i: Theoretical considerations and design criteria," vol. 10, no. 4, pp. 421–427, 1983.

[14] J. B. Martin, G. F. Knoll, D. K. Wehe, N. Dogan, V. Jordanov, N. Petrick, and M. Singh, "A ring compton scatter camera for imaging medium energy gamma rays," *Nuclear Science, IEEE Transactions on*, vol. 40, pp. 972 –978, aug 1993.

[15] M. Cunningham, M. Burks, D. Chivers, C. Cork, L. Fabris, D. Gunter, T. Krings, D. Lange, E. Hull, L. Mihailescu, K. Nelson, T. Niedermayr, D. Protic, J. Valentine, K. Vetter, and D. Wright, "First-generation hybrid compact compton imager," in *Nuclear Science Symposium Conference Record, 2005 IEEE*, vol. 1, pp. 312 –315, oct. 2005.

[16] Y. F. Du, Z. He, G. F. Knoll, D. K. Wehe, and W. Li, "Evaluation of a compton scattering camera using 3-d position sensitive CdZnTe detectors," *Nuclear Instruments and Methods in Physics Research Section A: Accelerators, Spectrometers, Detectors and Associated Equipment*, vol. 457, no. 1-2, pp. 203 – 211, 2001.

[17] C. E. Lehner, Z. He, and F. Zhang, "4π compton imaging using a 3-D position-sensitive CdZnTe detector via weighted list-mode maximum likelihood," *IEEE Trans. Nucl. Sci.*, vol. 51, pp. 1618–1624, August 2004.

[18] L. E. Smith, C. Chen, D. K. Wehe, and Z. He, "Hybrid collimation for industrial gamma-ray imaging: combining spatially coded and compton aperture data," *Nuclear Instruments and Methods in Physics Research Section A: Accelerators,Spectrometers,Detectors and Associated Equipment*, vol. 462, no. 3, pp. 576 – 587, 2001.

[19] M. Amman, P. N. Luke, J. S. Lee, L. Mihailescu, K. Vetter, A. Zoglauer, C. B. Wunderer, M. Galloway, S. E. Boggs, H. Chen, P. Marthandam, S. Awadalla, S. Taherion, and G. Bindley, "Detector module development for the high efficiency multimode imager," in *Nuclear Science Symposium Conference Record (NSS/MIC), 2009 IEEE*, pp. 981 –985, 24 2009-nov. 1 2009.

[20] A. Takada, K. Hattori, H. Kubo, K. Miuchi, T. Nagayoshi, H. Nishimura, Y. Okada, R. Orito, H. Sekiya, A. Tada, and T. Tanimori, "Development of an advanced compton camera with gaseous tpc and scintillator," *Nuclear Instruments and Methods in Physics Research Section A: Accelerators, Spectrometers, Detectors and Associated Equipment*, vol. 546, no. 1-2, pp. 258 – 262, 2005. Proceedings of the 6th International Workshop on Radiation Imaging Detectors - Radiation Imaging Detectors 2004.

[21] D. H. Chivers, A. Coffer, B. Plimley, and K. Vetter, "Electron-track compton imaging using high-resolution charge-coupled devices," in *Nuclear Science Symposium Conference Record (NSS/MIC), 2010 IEEE*, pp. 1512 –1517, 30 2010-nov. 6 2010.

[22] Z. He, W. Li, G. F. Knoll, D. K. Wehe, J. Berry, and C. M. Stahle, "3-D position sensitive CdZnTe gamma-ray spectrometers," *Nucl. Inst. & Meth. A*, vol. 422, pp. 173–8, 1999.

[23] Z. He, "Review of the shockley-ramo theorem and its application in semiconductor gamma-ray detectors," *Nuclear Instruments and Methods in Physics Research Section A: Accelerators,Spectrometers,Detectors and Associated Equipment*, vol. 463, no. 1-2, pp. 250 – 267, 2001.

[24] O. Frisch, "British atomic energy report br-49," tech. rep., 1944.

[25] P. N. Luke, "Single polarity charge sensing in ionization detectors using coplanar electrodes," *Applied Physics Letters*, vol. 65, pp. 2884 –2886, nov 1994.

[26] P. N. Luke, "Unipolar charge sensing with coplanar electrodes-application to semiconductor detectors," *Nuclear Science, IEEE Transactions on*, vol. 42, pp. 207 –213, aug 1995.

[27] B. Sturm, *Gamma-ray Spectroscopy using depth-sensing coplanar grid CdZnTe semiconductor detectors.* PhD thesis, University of Michigan, Ann Arbor, 2007.

[28] H. H. Barrett, J. D. Eskin, and H. B. Barber, "Charge Transport in Arrays of Semiconductor Gamma-Ray Detectors," *Physical Review Letters*, vol. 75, pp. 156–159, July 1995.

[29] Z. He, G. F. Knoll, D. K. Wehe, R. Rojeski, C. H. Mastrangelo, M. Hammig, C. Barrett, and A. Uritani, "1-d position sensitive single carrier semiconductor detectors," *Nuclear Instruments and Methods in Physics Research Section A: Accelerators, Spectrometers, Detectors and Associated Equipment*, vol. 380, no. 1-2, pp. 228 – 231, 1996. Proceedings of the 9th International Workshop on Room Temperature Semiconductor X- and @c-Ray Detectors, Associated Electronics and Applications.

[30] G. F. Knoll, *Radiation Detection and Measurement.* Jone Wiley & Sons, Inc., 3rd ed., 1999.

[31] F. Zhang and Z. He, "New readout electronics for 3-d position sensitive CdZnTe/HgI detector arrays," *Nuclear Science, IEEE Transactions on*, vol. 53, pp. 3021 –3027, oct. 2006.

[32] F. Zhang, W. R. Kaye, and Z. He, "Performance of 3-d position sensitive CdZnTe detectors for gamma-ray energies above 1 mev," in *Nuclear Science Symposium Conference Record (NSS/MIC), 2009 IEEE*, pp. 2012 –2016, 24 2009-nov. 1 2009.

[33] G. De Geronimo, E. Vernon, K. Ackley, A. Dragone, J. Fried, P. O'Connor, Z. He, C. Herman, and F. Zhang, "Readout asic for 3d position-sensitive detectors," *Nuclear Science, IEEE Transactions on*, vol. 55, pp. 1593 –1603, june 2008.

[34] F. Zhang, *Events reconstruction in 3-D position sensitive CdZnTe gamma-ray spectrometers.* PhD thesis, University of Michigan, Ann Arbor, 2005.

[35] W. R. Kaye, *Event Reconstruction in Pixelated CdZnTe Detectors.* PhD thesis, University of Michigan, Ann Arbor, 2011.

[36] F. Zhang, W. R. Kaye, Y. A. Boucher, J. Jaworski, C. G. Wahl, W. Wang, S. Joshi, and Z. He, "Measurement results using the polaris 3d-position-sensitive CdZnTe imaging spectrometer array system," in *INMM*, 2011.

[37] F. Zhang, Z. He, and C. E. Seifert, "A prototype three-dimensional position sensitive CdZnTe detector array," *Nuclear Science, IEEE Transactions on*, vol. 54, pp. 843 –848, aug. 2007.

[38] S. J. Kaye, W. R. Kaye, and Z. He, "Experimental demonstration of coded aperture imaging using thick 3d-position-sensitive CdZnTe detectors," in *Nuclear Science Symposium Conference Record (NSS/MIC), 2009 IEEE*, pp. 1902 –1906, 24 2009-nov. 1 2009.

[39] W. R. Kaye and Z. He, "Depth reconstruction validation for multiple interaction events in pixelated CdZnTe detectors," *To be submitted*, 2011. Manuscript in preparation.

[40] J. C. Kim, W. R. Kaye, F. Zhang, W. Wang, and Z. He, "Electron drift velocity non-uniformity in pixelated CdZnTe detectors," *To be submitted*, 2011.

[41] C. L. Thrall, C. G. Wahl, and Z. He, "Performance of five-or-more-pixel event sequence reconstruction for 3-d semiconductor gamma-ray-imaging spectrometers," in *Nuclear Science Symposium Conference Record, 2008. NSS '08. IEEE*, pp. 1299 –1301, oct. 2008.

[42] J. C. Kim, S. E. Anderson, W. R. Kaye, F. Zhang, Y. Zhu, S. J. Kaye, and Z. He, "Charge sharing in common-grid pixelated CdZnTe detectors," *Nuclear Instruments and Methods in Physics Research Section A: Accelerators, Spectrometers, Detectors and Associated Equipment*, vol. In Press, Corrected Proof, pp. –, 2011.

[43] W. Wang, W. Kaye, J. C. Kim, F. Zhang, and Z. He, "Improvement of compton imaging efficiency by using side-neighbor events," in *Nuclear Science Symposium Conference Record (NSS/MIC), 2010 IEEE*, pp. 1101 –1103, 30 2010-nov. 6 2010.

[44] C. G. Wahl, *Imaging, Detection, and Identification Algorithms for Position-Sensitive Gamma-Ray Detectors.* PhD thesis, University of Michigan, Ann Arbor, 2011.

[45] J. Hsieh, *Computed tomography: principles, design, artifacts, and recent advances.* SPIE Press monograph, SPIE Press, 2003.

[46] L. A. Shepp and Y. Vardi, "Maximum likelihood reconstruction for emission tomography," *Medical Imaging, IEEE Transactions on*, vol. 1, pp. 113 –122, oct. 1982.

[47] T. F. Budinger, S. E. Derenzo, G. T. Gullberg, W. L. Greenberg, and R. H. Huesman, "Emission computer assisted tomography with single-photon and positron annihilation photon emitters," *Journal of Computer Assisted Tomography*, vol. 1, no. 1, 1977.

[48] A. P. Dempster, N. M. Laird, and D. B. Rubin, "Maximum likelihood from incomplete data via the EM algorithm," *J. R. Statist. Soc.*, vol. 39, no. 1, pp. 1–38, 1977.

[49] W. H. Richardson, "Bayesian-based iterative method of image restoration," *J. Opt. Soc. Am.*, vol. 62, pp. 55–59, Jan 1972.

[50] L. B. Lucy, "An iterative technique for the rectification of observed distributions," *AJ*, vol. 79, pp. 745–+, June 1974.

[51] H. H. Barrett, T. White, and L. C. Parra, "List-mode likelihood," *J. Opt. Soc. Am. A*, vol. 14, pp. 2914–2923, Nov 1997.

[52] L. Parra and H. H. Barrett, "List-mode likelihood: EM algorithm and image quality estimation demonstrated on 2-D pet," *IEEE Trans. Med. Imag.*, vol. 17, pp. 228–235, April 1998.

[53] R. A. Kroeger, W. N. Johnson, J. D. Kurfess, B. F. Phlips, and E. A. Wulf, "Three-compton telescope: theory, simulations, and performance," *IEEE Trans. Nucl. Sci.*, vol. 49, pp. 1887–1892, August 2002.

[54] I. Y. Lee, "Gamma-ray tracking detectors," *Nucl. Instrum. Methods A*, vol. 422, pp. 195–200, February 1999.

[55] D. Xu and Z. He, "Gamma-ray energy-imaging integrated spectral deconvolution," *Nuclear Instruments and Methods in Physics Research Section A: Accelerators, Spectrometers, Detectors and Associated Equipment*, vol. 574, no. 1, pp. 98 – 109, 2007.

[56] W. Wang, C. Wahl, and Z. He, "Maximum likelihood estimation maximization deconvolution in spatial and combined spatial- energy domains for a detector array system," in *Nuclear Science Symposium Conference Record, 2007. NSS '07. IEEE*, vol. 3, pp. 1965 –1970, 26 2007-nov. 3 2007.

[57] W. Wang, C. G. Wahl, and Z. He, "Maximum likelihood estimation maximization deconvolution in spatial and combined spatial-energy domains for combined single-, two- and three-interaction events," IEEE Nuclear Science Symposium Conference, 2008.

[58] W. Wang, C. G. Wahl, J. M. Jaworski, and Z. He, "Maximum-likelihood deconvolution in the spatial and spatial-energy domain for events with any maximum-likelihood deconvolution in the spatial and spatial-energy domain for events with any number of interactions," *Submitted to IEEE Trans. Nucl. Sci.*, 2011.

[59] D. Xu, J. A. Fessler, and Z. He, "Estimation of the sensitivity image in the maximum likelihood image reconstruction.".

[60] D. Xu, "Sensitivity image study." April 2005.

[61] S. Agostinelli *et al.*, "GEANT4: A simulation toolkit," *Nucl. Instrum. Meth.*, vol. A506, pp. 250–303, 2003.

[62] W. Wang, J. M. Jaworski, W. R. Kaye, and Z. He, "Applications of the energy-imaging integrated deconvolution algorithm for source chatracterization," in *Nuclear Science Symposium Conference Record (NSS/MIC), 2009 IEEE*, pp. 1065 –1068, 24 2009-nov. 1 2009.

[63] W. Wang, Z. He, C. G. Wahl, and F. Zhang, "Detecting shielded sources using 3-d CdZnTe detectors," in *Nuclear Science Symposium Conference Record, 2008. NSS '08. IEEE*, pp. 465 –467, oct. 2008.

[64] O. Catelinois, A. Rogel, D. Laurier, S. Billon, D. Hemon, P. Verger, and M. Tirmarche, "Lung cancer attributable to indoor radon exposure in france: Impact of the risk models and uncertainty analysis," *Environ Health Perspect*, vol. 114, 05 2006.

[65] P. H. G. M. Hendriks, J. Limburg, and R. J. de Meijer, "Full-spectrum analysis of natural [gamma]-ray spectra," *Journal of Environmental Radioactivity*, vol. 53, no. 3, pp. 365 – 380, 2001.

[66] "http://www.livestrong.com/article/498766-how-much-potassium-is-in-light-salt/."

[67] "http://www.mortonsalt.com/products/foodsalts/lite_salt.htm."

[68] K. P. Ziock, A. Cheriyadat, L. Fabris, J. Goddard, D. Hornback, T. Karnowski, and J. N. R. Kerekes, "Autonomous radiation monitoring of small vessels," in *SORMA XII, Ann Arbor, Michigan*, 2010.

[69] T. Aucott, F. Jensen, and M. Bahr., "Machine vision radiation detection system," in *ARI Conf.*, 2009.

[70] D. Hochbaum, *The multi-sensor nuclear threat detection problem*, pp. 389–99. Operations Research and Cyber-Infrastructure Springer US Part III Subpart 6, 2009.

[71] B. D. Y. et al, "Ge intelligent personal radiation locator system," in *ARI Conf.*, 2009.

[72] Y. Picard and C. J. Thompson, "Motion correction of pet images using multiple acquisition frames," *Medical Imaging, IEEE Transactions on*, vol. 16, pp. 137 –144, april 1997.

[73] F. L. et al, "List-mode-based reconstruction for respiratory motion correction in pet using non-rigid body transformations," *Phys. Med. Biol.*, vol. 52, pp. 5187–5204, 2007.

[74] A. Rahmim, P. Bloomfield, S. Houle, M. Lenox, C. Michel, K. R. Buckley, T. J. Ruth, and V. Sossi, "Motion compensation in histogram-mode and list-mode em reconstructions: beyond the event-driven approach," *Nuclear Science, IEEE Transactions on*, vol. 51, pp. 2588 – 2596, oct. 2004.

[75] J. M. Jaworski, W. Wang, and Z. He tech. rep., Univeristy of Michigan, 2011.

[76] J. M. Jaworski, C. G. Wahl, W. Wang, J. A. Fessler, and Z. He, "Model-based reconstruction of spectral and spatial source distribution from objects with known motion," in *Nuclear Science Symposium Conference Record (NSS/MIC), 2010 IEEE*, pp. 1518 –1524, 30 2010-nov. 6 2010.

[77] J. M. Jaworski, C. G. Wahl, W. Wang, J. A. Fessler, and Z. He, "Model-based reconstruction of spectral and spatial source distribution for objects with known motion," *Manustript In Preparation*, 2011.

[78] S. E. Anderson, *Event classification for 3-D Position sensitive semiconductor detectors*. PhD thesis, University of Michigan, Ann Arbor, 2011.

[79] S. E. Anderson, B. Donmez, and Z. He, "Sub-pixel position resolution in pixelated semiconductor detectors," in *Nuclear Science Symposium Conference Record, 2007. NSS '07. IEEE*, vol. 2, pp. 1569 –1576, 26 2007-nov. 3 2007.

[80] Y. Zhu, S. E. Anderson, and Z. He, "Sub-pixel position sensing for pixelated, 3-d position sensitive, wide band-gap, semiconductor, gamma-ray detectors," *Nuclear Science, IEEE Transactions on*, vol. 58, pp. 1400 –1409, june 2011.

[81] Y. Zhu, *Digital Signal Processing Methods for Pixelated 3-D Position Sensitive Room-Temperature Semiconductor Detectors*. PhD thesis, University of Michigan, Ann Arbor, 2011.